AN ATHERMAL PHONON MEDIATED DARK MATTER DETECTOR WITH SURFACE EVENT DISCRIMINATION

A DISSERTATION
SUBMITTED TO THE DEPARTMENT OF PHYSICS
AND THE COMMITTEE ON GRADUATE STUDIES
OF STANFORD UNIVERSITY
IN PARTIAL FULFILLMENT OF THE REQUIREMENTS
FOR THE DEGREE OF
DOCTOR OF PHILOSOPHY

Roland Michael Clarke
May 1999

I certify that I have read this dissertation and that in my opinion it is fully adequate, in scope and in quality, as a dissertation for the degree of Doctor of Philosophy.

Blas Cabrera
(Principal Adviser)

I certify that I have read this dissertation and that in my opinion it is fully adequate, in scope and in quality, as a dissertation for the degree of Doctor of Philosophy.

Doug Osheroff

I certify that I have read this dissertation and that in my opinion it is fully adequate, in scope and in quality, as a dissertation for the degree of Doctor of Philosophy.

Robert Wagner

Approved for the University Committee on Graduate Studies:

Abstract

There exists an overwhelming body of observational evidence that most of the matter in the universe is dark. The constraints of big bang nucleosynthesis coupled with lower limits on the matter density from dynamical estimates suggests that there exists large quantities of non-baryonic dark matter in the universe. In order to have avoided detection thus far, this new particle must interact only through the weak and gravitational forces. The presence of very old galaxies and clusters point strongly to a particle that was non-relativistic at the weak-scale decoupling time in the early universe. A well motivated candidate for this Weakly Interacting Massive Particle (WIMP) is a relic partner predicted from supersymmetric (SUSY) theories.

If our Milky Way halo were composed of WIMPs, we expect them to be in a dissipationless, spherical distribution random Boltzmann velocities. A detector on the earth, carried through the galaxy at the orbital speed of the sun ($\sim 300\,\mathrm{km/s}$ or 10^{-3}c), could detect the recoil energy imparted by a WIMP scattering with one of its nuclei. Characteristic energies in this interaction would be $\sim 10\,\mathrm{keV}$ for WIMP masses of $\sim 10\,\mathrm{GeV/c^2}$. A suitable dark matter detector would have to have a threshold of $\sim 1\,\mathrm{keV}$ to be viable. Estimates of the density of the dark galactic halo in the solar neighborhood are on the order of 0.3 $\mathrm{GeV/c^2cm^3}$. Combining this ambient flux with an upper limit of the theoretical WIMP-nucleon cross section from SUSY theory of $\sim 10^{-41}\mathrm{cm^2}$ gives us the extremely low event rates of $\sim$1 per kilogram per day. A suitable dark matter detector must therefor also have a high degree of background rejection capability. This thesis describes the development of such a detector capable of detecting these relic dark matter particles.

In order to achieve very low thresholds, coupled with powerful background rejection capabilities, we have developed a cryogenic athermal phonon-based dark matter detector. By cooling a semiconductor absorber to millikelvin temperatures, phonons generated by particle events can have lifetimes of $\sim 100\,\mu$s and can propagate many centimeters. We absorb these phonons on large area aluminum collector fins which diffusively transmit energy to an electrothermal-feedback-transition-edge-sensor (ETF-TES) through quasiparticle mediation. The resulting current pulse is then read out using a high-bandwidth DC SQUID array. By combining this phonon readout with a low voltage ionization detector we can reject bulk electron recoil backgound events to better than 1 in 10^3.

We present evidence that the phonon readout in this dark matter detector is sufficiently fast to distiguish between ballistic and quasiballistically propagating phonons in silicon. Taking advantage of the down-conversion of phonons in metallic layers at the detector surface we use rise time to reject a soft electron background at better than 1 in 30. We present data from this detector in the Stanford Underground Facility (SUF) and discuss their implication for possible WIMP-nucleon cross section upper limits. In a series of calibration experiments we show that phonons generated by electron-holes have a clearly different spectrum than those generated in particle events. A first attempt to exploit this effect in the development of a phonon-based discrimination technique is discussed. Finally, we discuss theoretical limits to this detector technology and speculate on likely progress in the near future.

Acknowledgements

It has been a privilege and a joy to do my thesis under Blas Cabrera. He is as close to the ideal of a perfect advisor as I could ever imagine. His first priority was always the welfare of his students, constantly attentive and willing to encourage. I can not recall a single occasion when upon talking to him I did not feel my faith and enthusiasm for physics renewed. Sae Woo Nam is an incredibly talented individual. Working with him for the majority of my PhD. was a great privilege. His quickness was astounding, his ability to see through a situation and gauge what was necessary was truly unbelievable. He truly is one of the most gifted individuals I have ever worked with. I would like to thank Andrea Davies for being a good friend during trying times, and an understanding work mate. I must also thank Paul Brink for being a constant and attentive tutor, even if I seldom appreciated it. His knowledge was indispensable in the furthering of our understanding of the sensors, and his patience with me was more than I deserved. His working attitude was always refreshing, I'll never forget the long Rose and Crown lunches while we were slogging away in the clean room. In the brief time I knew Pierre Colling he impressed me immensely as a person with his feet on the ground. I wish good luck with his career in the 'real world'. Mike Penn was the first person I worked with in the Cabrera group. He allowed me to participate in research immediately and to touch equipment that he needed for the completion of his thesis. He had patience with me and I appreciated that. He also gave me a new outlook toward opera. My overlap with Kent Irwin was brief, but I must say that his enthusiastic personality was a large component in my decision to join Blas' group. Richard Gaitskell has become one of my good friends in the CDMS collaboration. His breadth of knowledge in physics is as impressive

as his thoroughness in problem solving. Much more importantly, he recognizes the necessity of a good pint. Betty Young showed me great kindness during my time as a graduate student. I was honored to have been allowed to participate in the light-second of little blue. Jochen Hellmig arrived at possibly the worst time and place in the history of CDMS. He managed to keep a good attitude and succeed under incredible pressure. I hope the new faces, Tarek, Aaron and Tali find as much enjoyment doing their dissertation with Blas as I have. I further hope that the string of Canadians does not end with Tarek. I'd like to thank Mike Hennessey for always being the man with practical sense and the ability to construct something fast. Richard Schnee's initial task as a postdoc in CDMS was to take over the messy, ill-conceived shell that Sae Woo and I had constructed as dark pipe and to turn it into a viable, flexible analysis tool. His patients and competence were exactly what the experiment needed. Mike Crisler and Steve Eichblatt were a pleasure to work with when the experiment finally needed some input from big science. Steve was the source of much needed fresh ideas when the acquisition and data systems were under siege. Bernard Sadoulet has always shown me exceptional kindness and patience. In the times where I was fortunate enough to share his lab he always treated me as one of his own students. I had the privilege to use the dilution refrigerator lovingly brought into life and heavily modified by Tom Shutt. At times I was not as tender as I should have been and I do appreciate his patience. Doug Osheroff was my first advisor when I came to Stanford University. I'll never forget his kind words of encouragement or his generosity. I became good friends with his students and frequently abused his lab for spare parts and advice. Charlie Marcus was my first advisor at Stanford University. He introduced me to many aspects of experimental physics, and was one of my most attentive and resourceful tutors. Over my graduate career I must have visited the machine shop hundreds of times. Wolfgang Jung was always patient with me, and was always willing to listen to my ideas and correct them to make them better, cheaper or stronger. Karlheinz Mehlke took over this role when Wolfgang retired. Marcia Keating started her job as graduate secretary the year that I arrived at Stanford. Her first gesture was to invite the graduate students to her house for thanksgiving dinner. This is just an example of the hospitality she extended to all

of us during those years. I would like to thank Holly Ernst, and Linda Hubly for being patient with me when I would forget receipts, or need something ordered right away. This should be extended to the entire staff at Varian, they always went above and beyond the call of duty. Sven Rogge was one of the first friends I made when I came to the U.S. His zest for hard work infected me immediately. I will never forget the many nights of dinner at 3am at Taco Bell, or the Friday dinners before going to the Rose and Crown. I'd like to mention my roommate of several years, Mark Snodgrass. He kept me sane through difficult years and provided a sounding board for too many of my crazy ideas. He also put up with one of the messiest people on the planet, and for that I will always be grateful. Matija Siljak and Brian Kirsch became good friends late in my stay in California. Their influence on me was not always the best, but I certainly enjoyed every minute of it. I can't thank Analisa enough for being a constant ray of sunshine. I'll always look forward to Erin's rapid e-mail response, our long phone calls, and to her constant words of support. May she always be a kindred spirit. Never will I forget the free beers that Heather gave me, nor the constant parties at the Webster St. house. Thank you, Kathy, for being my friend and always willing to call me crazy. I'd like to thank Mark Kawcab for providing me with an exceptional public house. It has truly been my oasis of relief during these final graduate years. Finally I want to thank my family. To my parents William Brian Clarke and Michele Adriane Pannetier, I owe all that I am and will become. I thank my sister Lisa for still talking to me despite witnessing first hand the atrocities of sibling relationships. On balance I have had a remarkable experience here at Stanford, California and the United States. I would like to thank this country in general for taking in another one of us Canadians.

Contents

List of Tables

List of Figures

Chapter 1

Dark Matter

1.1 Introduction

The first identification of what is known as the dark matter matter problem came from the examination of the dynamics of nearby stars and galactic clusters[1] in the early 1930's. Since that time overwhelming evidence has accumulated on the magnitude, distance scale, and likely composition of the dark matter. This chapter is intended as a brief introduction to the field.

1.1.1 Mass to Light ratio

In the 1600's Johannes Kepler formulated his famous law of orbital motion

$$T^2 \propto kR^3 \tag{1.1}$$

based on the measurements of the period and radii of the visible planets. As we now know, k = $(2\pi)^2$/GM, and the law 1.1 is a simple consequence of the planets moving around the sun in the absence of any other perturbing gravity. The sun can be 'weighed' in this way quite reliably giving a modern value of 2.0 x 10^{30} kg[2].

Since the power output of the sun is 3.9 x 10^{26} W in the optical, we may state the Mass-to-light ratio of the solar system as $M_\odot/L_\odot = 5$ x 10^3 [kg/W]. All estimates of the mass-to-light ratio in the universe are referred back to this fundamental value of 5 Tonnes per Watt.

In the years 1835-40, using parallax motion caused by the rotation of the earth around the sun, Bessel and Henderson independently obtained a distance measurement for 61 cygni[3]. In this way the absolute magnitude (The magnitude of the object if it was at a distance of 10 parsecs) of stars of all spectral types have been measured. Measuring the mass of stars besides the sun was accomplished by studying the period and radii of resolved binary systems. Since about half of the stars in the galaxy are binaries, data on stellar masses became plentiful. Around the turn of the century Arthur Eddington showed that the luminosity of a star is almost completely determined by its mass and is largely independent of size. The classification system developed by Hertzsprung and (later) Russell enabled a stars mass to be estimated by its spectral characteristics alone.

By studying variable stars in the Small Magellanic Cloud and assuming that, since the stars were all at similar distances, a change in apparent magnitude implied a change in absolute magnitude, Henrietta Leavitt postulated that the period of Cepheid variables correlated with their absolute magnitudes[3]. In 1924 Hubble used Cepheids in Andromeda and other 'nebulae' to prove these objects were indeed outside of the Milky Way and constituted other galaxies. Coupling these data with the redshift surveys of Slipher and Humason, Hubble showed that distant galaxies were moving away from us at a rate proportional to their distance. This was the first evidence for the big bang, and the origin of the Hubble constant, H_o. The present value of this constant is still (surprisingly) quite uncertain due to the problems resolving peculiar velocities and finding appropriate distance estimators at each length scale. For an excellent review of cosmological distance indicators see ref. [4]. The

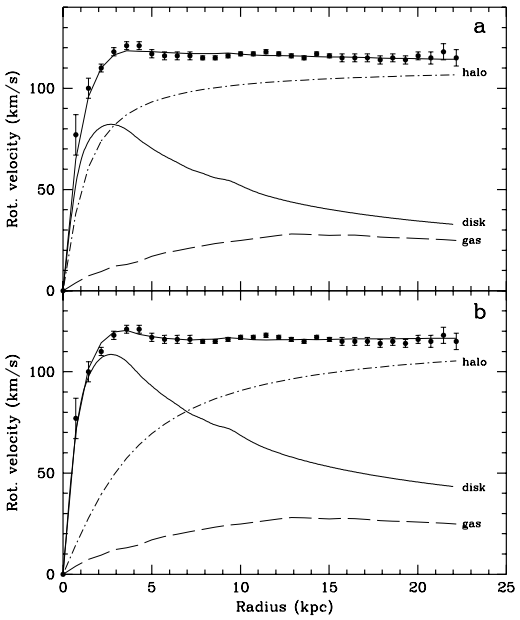

Figure 1.1: A plot of rotation velocity vs. galactic radius for a typical spiral galaxy. Doppler shift data is shown with the estimated disk mass distribution (solid), the gas component (dash), and the halo (dot-dash). The bottom plot uses a maximal disc hypothesis which decreases the halo fraction at low radius. From astro-ph/9706230.

favored range for the Hubble constant at present is 55 to 75 [$\mathrm{km\,s^{-1}Mpc^{-1}}$]. It is common to account for this uncertainty with a dimensionless constant, h, so that $\mathrm{H}_o = 100\,h$ [$\mathrm{km\,s^{-1}Mpc^{-1}}$]. Many cosmological parameters can then be quoted in terms of their dependence on h.

Galactic Rotation Curves

Galaxies can be classified into two major types, spiral and elliptical. The spiral galaxies have a dense, bright core surrounded by a thin rotating disk and can be divided into normal spirals, barred spirals, and lenticular (marginal disk) galaxies. In almost all spiral galaxies the luminosity profile is exponential

$$I(r) = I_o \exp(-r/r_o) \tag{1.2}$$

where r_o is the scale length of the galaxy (for the milky way is $\approx 3\,\mathrm{kpc}$[5]).

The velocity distribution of spiral galaxies can be measured using the Doppler shift of H or Ca emission lines as long as the disk is at a sufficiently oblique angle. The velocity distribution can be used as a tracer of the mass using

$$\frac{GM(r)}{r} = v(r)^2 \tag{1.3}$$

essentially Eq. 1.1. When one compares the predicted mass distribution in spiral galaxies from the luminosity profile (Eq. 1.2) to that predicted by the velocity distribution one finds them completely at odds (see Fig. 1.1). The velocity in a spiral galaxy tends to rise quickly in the central core region and then remains flat out to large distances. This velocity curve predicts a mass distribution with a form

$$\rho = \rho_o \frac{a^2 + r_o^2}{a^2 + r^2} \tag{1.4}$$

where the luminous mass becomes negligible as one travels out toward the edges of the galaxies. Estimates of the mass to light ratios of spiral galaxies range from 10 to 100 $\mathrm{M}_\odot/\mathrm{L}_\odot$ depending on how far out the rotation curve has been measured. Numerical simulations involving ejection of stars from a dwarf spheroidal galaxy, however, show a M/L capped at ~ 2.5[6]. The general trend of larger distance scales requiring larger and larger amounts of dark matter continues when one examines the velocity distribution galactic Clusters.

Cluster Masses

One of the first pieces of observational evidence for the dark matter problem was Zwicky's measurements of the peculiar velocities of the Coma cluster[7]. Using the virial theorem ($|\mathrm{T}|=\frac{1}{2}|\mathrm{U}|$) it is easy to show that

$$M \simeq \frac{2 < v^2 >< r >}{G} \tag{1.5}$$

This relation enables an observer to estimate the (mean) mass from the distance and velocity distributions of a cluster. Zwicky's observations of the mass-to-light ratio in the Coma cluster gave about 500 $\mathrm{M}_\odot/\mathrm{L}_\odot$. Later estimates were refined by Merritt[8] to a value of $\sim$350 $\mathrm{M}_\odot/\mathrm{L}_\odot$. It turns out that the Coma cluster is an ideal system to study due to its compactness and smooth density distribution. Despite the number of known rich clusters (many thousands in the northern sky) only a small percentage have been studied extensively. The CNOC (Canadian Network for Observational Cosmology) redshift survey conducted at the Canada-France-Hawaii telescope[9, 10] has compiled an impressive catalogue of over 6000 cluster redshifts. The best estimate for the mass-to-light ratios in these clusters is 288 ± 49 $\mathrm{M}_\odot/\mathrm{L}_\odot$.

Gravitational Lensing

One of the simple results of the theory of general relativity is that light passing close to a massive object is bent by twice the newtonian value

$$\hat{\alpha} = \frac{4GM}{c^2 b} = \frac{2R_s}{b} \tag{1.6}$$

where R_s is the Schwarzchild radius. It is easy to show[11] that, in general, a light ray is bent at an angle

$$\hat{\alpha} = \frac{2}{c^2} \int \vec{\nabla}_{\perp} \Phi \tag{1.7}$$

where Φ is the gravitational potential and the integral is taken along the ray path. Zwicky, in 1937, first argued that large nebulae may be massive enough to a produce measurable lensing effect[12] Observation of this gravitational effect was first confirmed with the discovery that two distant quasars were in fact multiple images of the same object[13]. Since then, over 30 multiply imaged sources have been discovered[14] that shed light on the dark matter distributions in the intervening lens galaxies. All contain significant halos that do not necessarily trace the light distribution and statistically their sparseness appears to rule out a matter dominated (CDM) universe with no cosmological constant. By studying the lensed images of several quasars Hawkins[15] estimates that 3/4 of galaxies are dark, in the sense that they contain mass to light ratios of several hundred $M_{\odot}/L_{\odot}$.

In the absence of a clear multiple image scenario the correlated distortions in galactic images may be used to reconstruct lens mass distributions. This effect, known as weak lensing, tends to bend distant galaxies into arc-lets facing toward the lens mass. Studies on rich clusters[16, 17] indicate large mass-to-light ratios ranging from about 100 to several hundred $M_{\odot}/L_{\odot}$[18]

1.1.2 The Nature of Dark Matter

The assumptions isotropy, homogeneity and Hubble's law lead to a simplified form of Einstein's field equations.

$$\ddot{R} = -\frac{4\pi G}{3} R\left(\rho + \frac{3p}{c^2}\right) + [\frac{1}{3}\Lambda R^2] \tag{1.8}$$

$$\dot{R}^2 = \frac{8\pi G\rho}{3} R^2 - kc^2 + [\frac{1}{3}\Lambda R^2] \tag{1.9}$$

where R is the scale factor, ρ is the total inertial mass density of the matter and radiation, p is the pressure, and k is a constant related to the radius of curvature of the universe. The cosmological constant Λ was first introduced by Einstein in 1917 as a kludge to accommodate a static universe. Prior to Hubble's discovery, Einstein had no knowledge of the expansion of space-time. He would later call the introduction of this constant the greatest blunder of his life[19].

Equation 1.9 is known as Friedmann's equation where the left hand side corresponds to the kinetic energy of the expanding fluid and the first term on the right hand side is its gravitational potential energy. The distance scale, R, is related to the present Hubble parameter, H_o by

$$H_o = \left(\frac{\dot{R}}{R}\right)_{t=now} \tag{1.10}$$

We can now introduce a critical density $\rho_c = (3H_o^2/8\pi\mathrm{G})$ so that the first term on the right of equation 1.9 contains just a density fraction. The critical density can then be expressed in terms of the dimensionless parameter, h,

$$\rho_c = 1.9 \times 10^{-26} h^2 \left[\frac{kg}{m^3}\right] = 11h^2 \left[\frac{GeV}{c^2 m^3}\right] \tag{1.11}$$

If Λ is positive (we consider a non-zero Λ due to recent observational arguments) it may be associated with a repulsive force of the vacuum induced by a scalar field. It can be shown[] that scalar fields have negative equations of state, p_v = -ρ_vc^2. If we add this type of density into equation 1.8 (where $\rho_m \propto 1/\mathrm{R}^3$ and ρ_v = constant) we find that

$$\ddot{R} = -\frac{4\pi G\rho_o}{3R^2} + \frac{8\pi G\rho_v}{3}R \tag{1.12}$$

so $8\pi G\rho_v$ acts just like Λ. Defining two more convenient parameters, $\Omega_m = \rho_m/\rho_c$ and analogously $\Omega_\Lambda = \rho_v/\rho_c$ we find that the deceleration of the universe at the

present epoch (R=1) can be written

$$q_o = \frac{\Omega_m}{2} - \Omega_\Lambda \tag{1.13}$$

If we return to equation 1.9 we can see that the curvature parameter, k, can be expressed as

$$k = \frac{[\Omega_m + \Omega_\Lambda - 1]}{c^2/H_o^2} \tag{1.14}$$

A universe with k $\equiv$ 0 (flat universe) is heavily favored by inflationary models of the big bang. Also non-flat universes quickly evolve into very sparse (open) or crunched (closed) universes. In order for the universe to be this close to the critical density at the present epoch, the density would have to have been within one part in 10^{60} of the critical density at the Plank time. We can, therefor, with confidence state that

$$\Omega_m + \Omega_\Lambda = 1 \tag{1.15}$$

1.1.3 Big Bang Nucleosynthesis

Big Bang Nucleosynthesis is one of the most successful, and consistent theories in cosmology. It also provides the most convincing argument as to why the dark matter can not be baryonic. Starting with a few basic assumptions about the early universe one can predict, using the appropriate nuclear reaction rates, the relative abundances of the light elements in the universe from the baryon to photon ratio (η).

The first attempt to combine nuclear reaction rates with a model of cosmological expansion was in 1948 by Alper, Bethe, and Gamow[21]. Later[22, 23, 24] many refinements of the theory took place until the uncertainties in the model were low

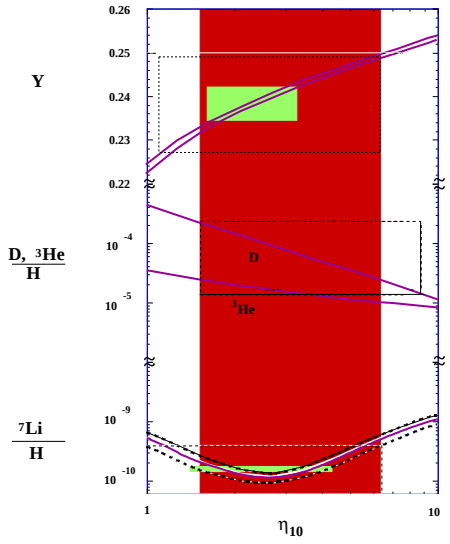

Figure 1.2: Constraints on the total baryon density from measurements of the abundances of the light elements. Shown are the Helium to Hydrogen ratio, Y, also Deuterium, Helium-3 and Lithium-7. The measurements lead to the constraints on $\eta \equiv 10^{10}\eta$ shown in grey. Taken from Olive[20]

enough to allow the total baryon density to be estimated from the relative abundances of the light elements.

When the universe was about one second old the neutron fraction froze out at a ratio of

$$\left[\frac{n}{p}\right] = \exp\left(\frac{-\Delta mc^2}{k_B T}\right) = 0.26 \tag{1.16}$$

In order for the light elements to form, the universe had to cool to about 10^9 K so that the tail of the blackbody distribution of photons no longer could dissociate deuterium (binding energy of 2.2 MeV). Extensive computer simulations of the universe in the epoch of 100 seconds to 300 seconds by Wagoner[25] and later by Kolb and Turner[26] predict the He, D,^{3}He, and ^{7}Li to H ratios given the baryon-to-photon-ratio $\eta = 2.74$ x $10^{-8}\,\Omega_B h^2$ (see Fig. 1.2).

Direct measurements of the ratios of these light elements in the early universe all carry particular systematic problems. Helium-4 is produced during stellar evolution, so the most accurate estimates of Y_p comes from low metalicity stars where stellar populations are the youngest. Olive and Steigman [27] find a value of 0.232 $\pm$ 0.005. Helium-3 has been found in meteorites with an abundance of [^{3}He/H] = 1.4 $\pm$ 0.4 x 10^{-5}[5] but varies between 1.2 and 15 x 10^{-5} from measurements of the ^{3}He hyperfine line in interstellar clouds. Since ^{3}He can both be destroyed and created during stellar evolution it is difficult to provide a consistent interpretation. Deuterium is the element that shows the strongest dependence on the present baryon density so should be the best indicator[28]. Deuterium is only destroyed during stellar evolution, therefor any measurement of its abundance represents a lower limit on the primordial value. Measurements of the absorption spectra of large redshift quasars seems to have a cieling of [D/H] = 2 x 10^{-4}[29]. Adopting a value of h =0.65 gives us

$$\Omega_B = 1.6 \times 10^{-2} \text{ [5]} \tag{1.17}$$

which is marginally consistent with the amount of visible matter but much less than the critical density, or even the lower limit of density set by the POTENT method. It is clear that the majority of matter in the universe must be non-baryonic. It is conventional, then, to define a baryonic mass density independent of the total matter density

$$(\Omega_B + \Omega_{DM} \equiv \Omega_m) + \Omega_\Lambda = 1 \tag{1.18}$$

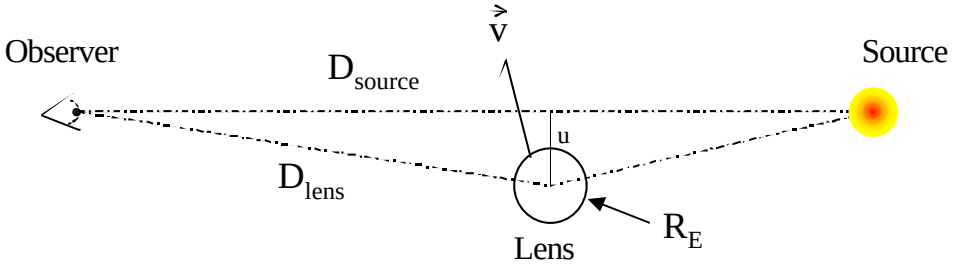

Figure 1.3: A diagram of a microlensing event. The impact parameter, u, is in terms of the Einstein radius (for an explanation see text).

Large Scale Flows

The mass distribution, and mass density at very large distance scales can be estimated using the velocity flows of large numbers of 'tracer' galaxies or clusters. Enormous catalogues[30] have been compiled of the peculiar velocities of distant galaxies with the aim of using these data to predict the mass distribution that might have given rise to these velocities. The intuitive idea is that peculiar motions result from gravitational potentials pulling and pushing (in the case of voids) on the tracer galaxies through the course of time. If one assumes a specific probability distribution for the initial fluctuations one can determine Ω. A very clever subset of these 'inverse' methods relies on no assumptions about the initial density perturbation or velocity distributions to place a lower limit on the total density. In order that the predicted mass density in the large voids do not fall ridiculously negative Dekel and Rees[31] has placed a 2.4 σ lower limit on Ω_m of 0.3. Given the constraints of big bang nucleosynthesis we are forced to have significant quantities of non-baryonic dark matter even in the presence of a cosmological constant.

Baryonic Dark Matter

Impressive constraints on the density of massive compact halo objects (MACHOs) can be obtained using a technique called microlensing. Similar to macrolensing (see preceding section) it takes advantage of the optical effects induced by gravitational matter, but without resolving separate images. It can be shown (see Fig. 1.4) that an intervening massive object moving across a star will magnify the apparent brightness of a star by the factor

$$A(t) = \frac{u^2 + 2}{u\sqrt{u^2 + 4}} \tag{1.19}$$

where u is the impact parameter

$$u(t) = \left[u_{min}^2 + \left(\frac{2(t - t_{max})}{\hat{t}}\right)\right]^{1/2} \tag{1.20}$$

$\hat{t}$ is the time for the lensing object to move through the Einstein radius, $R_E = \sqrt{4GmD/c^2}$. D is an adjusted distance, $D = D_{lens}(D_{source}\text{-}D_{lens})/D_{source}$, and m is the lens mass. The problem is that the Einstein radius is very small and if the galactic halo is made up of MACHOs, the probability of a lensing event is very low. Estimates of this probability based on realistic halo models[32, 33] are on the order of 3×10^{-6} (This is actually an estimate of the optical depth, a measure of the mass density along the line of sight). The first observation of microlensing toward the LMC[34] accompanied by many observations toward the galactic bulge[35, 36] hailed great promise that a large percentage of the halo could indeed be made of MACHOs. The measurement of a simple lens event has an intrinsic degeneracy between the lens distance and lens mass, however, leading to an unavoidable uncertainty. The measurement of binary events resolve this uncertainty, and a number of them have been confirmed to be in the LMC, not the galactic halo[37]. The lack of short

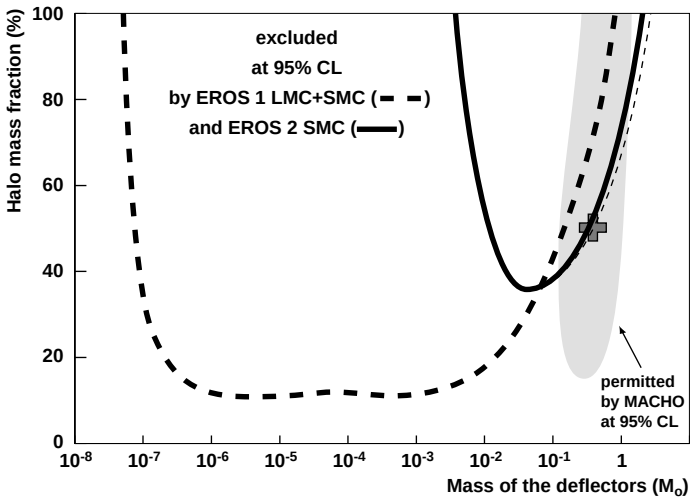

Figure 1.4: A combined exclusion plot of the milky way halo fraction as a function of lens mass. EROS1, EROS2 and MACHO data are combined. Masses below 10^{-7} $M_\odot$ and above 0.08 $M_\odot$ can be excluded by other arguments. From astro-ph/9812173.

duration events can be used to create a 90% confidence upper limit on Macho fraction of $\sim$20% over a large range of masses (see Fig. 1.4). For objects greater than 0.08 solar masses one expects hydrogen burning (brown dwarfs) to be initiated and therefor be visible with the Hubble space telescope. Objects smaller than 10^{-7} solar masses are unlikely to survive evaporation processes[6].

Despite the success of the microlensing searches it now appears unlikely that a significant component of the halo of composed of MACHOs. Excitement still continues in the field, with the possibility of resolving the caustics generated by small planetary objects[38]. This may provide a complimentary approach to the conventional Doppler shift method of searching for extra-solar planets. Valuable information has also been gained about the density profile of the galaxy toward the bulge[39].

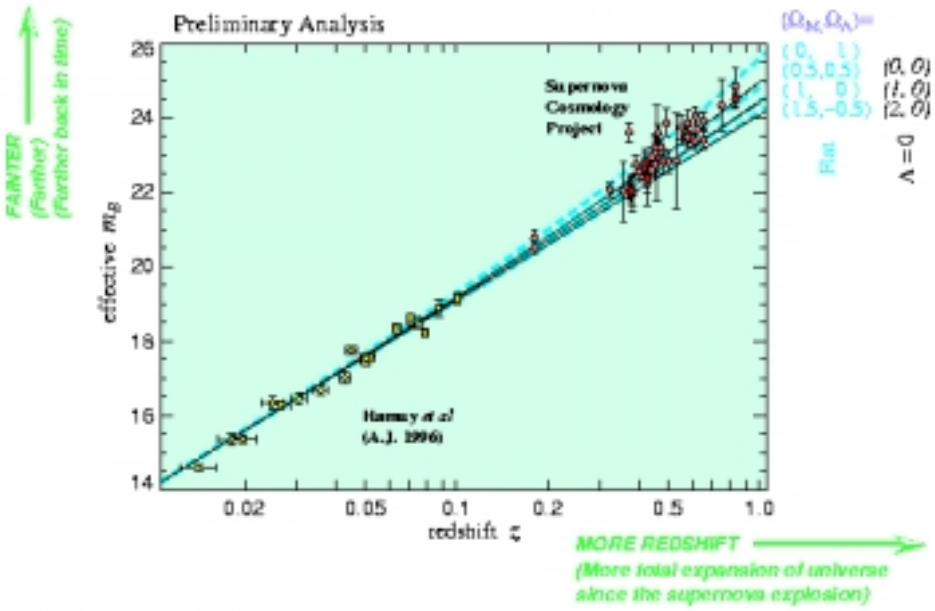

Figure 1.5: Plot of magnitude vs. redshift for Type 1a supernovae. The supernovae at high redshift should be brighter (lower) if their recessional velocity had remained constant through all time implying that the universe is slowing down. From astro-ph/9812473.

1.1.4 Super Novae Searches

Empirically Type 1a supernovae have been found to have a very small dispersion in absolute luminosity. The preferred model of these cataclysmic events is that a white dwarf is driven over the Chandrasekar mass of 1.4 $M_\odot$ by accretion from a binary companion. The luminosity is largely due to the radioactivity of ^{56}Ni that is ejected from the core during the explosion[40]. Since the composition of these white dwarfs is quite uniform at the end of their life cycle, the production of fresh ^{56}Ni is also. The peak luminosity of these objects turns out fortuitously to be an ideal standard candle.

Using techniques similar to those employed in the microlensing searches, two

groups[41, 42] have amassed an impressive number of light curves for distant supernovae. When very distant (high redshift) supernovae are observed, both groups arrive at the same startling result that the Hubble constant seems to have been larger at earlier times (see Fig. 1.5). This means that the universe use to be expanding faster than it is now. In terms of our earlier equations

$$q_o = \frac{\Omega_m}{2} - \Omega_\Lambda < 0 \tag{1.21}$$

The maximum likelihood regions of both groups are are consistent with

$$\Omega_m = 0.3 \pm 0.1 \;\; for \;\; \Omega_m + \Omega_\Lambda = 1 \tag{1.22}$$

1.1.5 Cosmic Microwave Background

In 1965 Penzias and Wilson, through a careful calibration of the noise in their horn antenna[43], discovered a uniform radiation at $\sim 3\,\mathrm{K}$. This cosmic microwave background radiation (CMB), along with Hubble's constant and primordial nucleosynthesis, is a critical piece of evidence for the big bang theory. For an excellent review of the subject, I suggest a recent article by Kamionkowski and Kosowski[44].

During the early phases of the expansion of the universe (including the phase of nucleosynthesis) photons and matter were in thermal equilibrium. When the universe was about 300,000 years old the temperature had dropped to 10,000 K ($\sim 1\,\mathrm{eV}$). At this point the photons could no longer ionize the free hydrogen so they effectively decoupled from the matter. Since this time these primordial photons have traveled ballistically throughout the dilute universe. This 'surface of last scatter' occurred at redshifts of about 1000. The size of a causally connected region of space, therefor, is about as large as the universe was when the photons decoupled. A region of 300,000 light years at redshifts of 1000 sub-tend an angle of only one degree of the sky. The

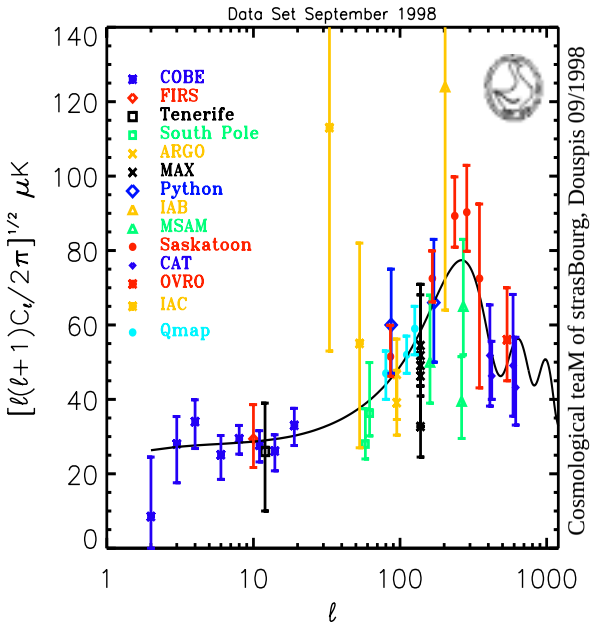

Figure 1.6: A summary of satellite and ground based observations of the power as a function of angular scale in the cosmic microwave background. The curve shown is for a $\Omega_M = 0.2$ $\Omega_\Lambda = 0.8$ universe. From astro-ph/9903260

fluctuations in the CMB at angular scales finer than a degree, then, tell us about the quantum fluctuations in density during the period of inflation that gave rise to large scale structure and galaxy formation. Measurements of the power spectrum of the CMB at fine angular scales have the promise of providing serious constraints on the values of H_o, Ω_m and Ω_Λ.

An anisotropy of $\sim 10\,\mathrm{mK}$ in the CMB was discovered in 1976 using balloon flights[45] and confirmed using U-2 aircraft[46]. This could be explained by the fact that we are moving with a peculiar velocity of about 300 km/s with respect to the rest frame of the big bang.

In 1989 the Cosmic Microwave Background Explorer (COBE) satellite was launched and succeeded in measuring the uniformity of the CMB to one part in 10^5[47]. At

the limit of the angular resolution of COBE, 7 degrees (about 14 times larger than the moon), there are fluctuations in the CMB temperature of about 0.2 mK.

The rapid improvements in technology available to ground based, and balloon based experiments[48] have lowered the angular scale of CMB measurements to less than half a degree (for the OVRO telescopes). Several ambitious new balloon experiments plan to map out larger portions of the sky and at finer angular scales. MAXIMA, the successor to the MAX program has just completed its first flight with eight simultaneous 12 arcmin pixels. BOOMERANG and TOPHAT are planning to circle the south pole in a flights lasting as long as 14 days. Ground based GHz interferometer arrays such as CAT, CBI and DASI will be coming on line in the next year. These experiments aim to constrain the total density Ω and H_o to a 10% error and give significant information on the second Doppler peak[48]. These experiments are all racing to examine as much of the sky as possible before the next generation satellites, MAP and Planck Surveyor, are launched. The NASA satellite, MAP, will have 5 frequency channels and resolution of 12 arcmin and should fly by late 2000. The ESA satellite will combine HEMT and bolometer technology with an angular resolution of 4 arcmin but will not launch until 2007.

1.2 Non Baryonic Dark Matter

1.2.1 Candidates

Neutrinos

The only previously discovered particle to interact solely through the weak force is the neutrino. This fact alone makes it a compelling choice when seeking a dark matter candidate. Recent confirmation of atmospheric neutrino oscillations (implying a non-zero neutrino mass)[49] have heated up the debate on whether neutrinos are a

major constituent of the dark matter. Models of structure formation in the early universe (both with and without a cosmological constant), however, seem to rule out an abundant relativistic particle[50]. Upper limits on the electron neutrino mass of $\sim 5\,\mathrm{eV}$ from beta decay experiments rule out a critical density population.

Axions

The axion was first proposed in 1977[51, 52, 53] as the boson associated with the P (parity) and CP (charge-parity or => anti-particle) discrete symmetries. The mass of the axion is small, $\sim$ 1-1000 μeV[54], yet was formed out of equilibrium so it would be non-relativistic. Many axion detection experiments have been undertaken which hope to see the resonant decay of axions in a magnetic field.

WIMPS

The best motivated non-baryonic dark matter candidate is the lightest superpartner in many supersymmetric theories (SUSY), the neutralino[55]. The essentials of supersymmetry theory are that every boson has a fermionic partner and every fermion has a bosonic partner. This frightening doubling of the number of particles (non of which have so far been detected) is necessary to solve the so called guage hierarchy problem that prevents the mass of the Higgs from becoming very heavy. Since 'partner type' number is conserved in these theories all superpartners must decay to other superpartners, so the lightest of these must be stable. Through a wide range of parameter space Minimally Supersymmetric theories (MSSM) predict relic abundances of this lightest supersymmetric partner (LSP) in a density range capable of closing the universe. It is this LSP WIMP that we hope produces a measurable signal in our detectors.

1.2.2 Direct Detection Experiments

Heidelberg-Moscow

The Heidelberg-Moscow experiment has achieved very low backgrounds using conventional Ge diode ionization detectors[56]. Originally designed as a double beta decay experiment, most of the 10.96 kg of detectors located in the Gran Sasso Underground Laboratory were optimized for the energy region of 2 MeV. The most impressive dark matter limits have come from one enriched ^{76}Ge detector run in a special low threshold configuration. The active mass of this detector is now 2.758 kg with a total analyzed exposure of 0.69 kg-years. The very low event rate of 0.042 cts/kg/keV/d from 15 to 40 keV has been achieved through extreme original cleanliness of the detectors and the decay of the cosmogenic activity in the Ge and copper from being 4 years underground.

The fact that this experiment employs no background rejection means that, in the present configuration, essentially no improvement in results is expected. The new Heidelberg Dark Matter Search (HDMS) experiment has recently been commissioned using two cylindrical Ge diodes operating in anti-coincidence mode[57]. GEANT simulations of the two-detector geometry predict a factor of 10-20 suppression in background rate.

A much larger experiment is proposed which will employ tonne of germanium suspended directly in liquid nitrogen. If proponents are correct and most of the internal contamination actually comes from the copper housing, this GErmanium in liquid Nitrogen Underground Setup (GENIUS) will be able to probe much of the SUSY phase space for WIMPs and probe neutrino masses down to 0.02 eV[58].

DAMA

The DAMA collaboration now employs the largest active mass for the purpose of a particle dark matter search[59]. Situated in the Gran Sasso underground laboratory, this group has operated nine 9.7 kg NaI detectors for an impressive 20 tonne-days of exposure. Due to their enormous number of events, the DAMA group can realistically hope to see a modulation in rate induced by the earth revolving around the sun (the earths velocity is $\sim$ 1/10th that of the sun around the galaxy). At several conferences, and now in published papers, this group has claimed discovery of this annular modulation effect, produced by a WIMP of 80-120 $\mathrm{GeV/c^2}$ with a cross section on the order of $10^{-41}\,\mathrm{cm^2}$. The effect is most visible in the lowest energy bin, however, where systematic effects are the most uncertain. Confirmation or denial of this result is likely by the CDMS experiment within the millenium.

UKDM

Located 1100 m underground in the Boulby salt mine, the UK Dark Matter experiment occupies an impressive low background site. Like the DAMA experiment, the technology involves measurement of scintillation light in large crystals of NaI at liquid nitrogen temperature. Unlike the DAMA experiment, UKDM places more emphasis on the discrimination capability of NaI. By comparing the arrival time distribution of light pulses UKDM have lowered their effective background by factors of 10-40 in the 4-25 keV range[60].

An annually modulated signal in the nuclear recoil spectrum has been observed by UKDM[61], however they do not claim positive WIMP identification. The likely cause of the signal is thought to be surface alpha contamination modulated by humidity or temperature within the mine.

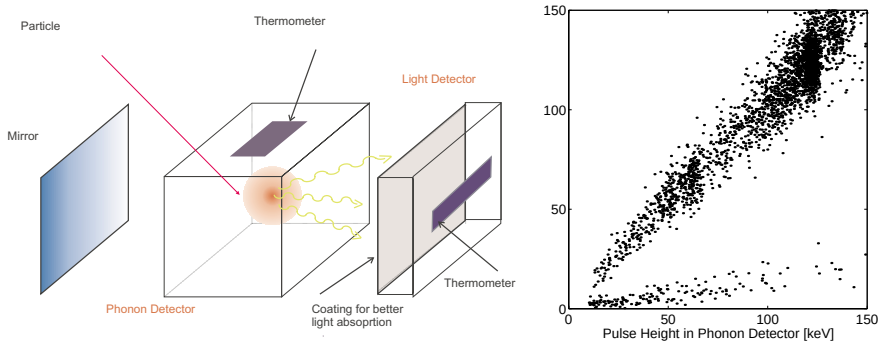

Figure 1.7: A diagram of the new hybrid scintillation-phonon detector developed by the CRESST collaboration. On the right is a plot of light vs. heat for electron and nuclear recoils. From astro-ph/9904005

CRESST

Like the DAMA experiment, CRESST is located at the underground laboratory in Gran Sasso. Like the CDMS experiment it is attempting to take advantage of the low threshold and background rejection of cryogenic detectors to improve the limits of WIMP sensitivity. This group has concentrated on a type of detector known as the SPTT (Superconducting Phase Transition Thermometer). It is similar to the QET phonon detectors in that it consists of a tungsten superconductor, but is operated in a very different mode. Instead of the extreme voltage bias regime, they operate the transition edge thermometer in a regime of almost neutral bias. The device, to first order, neither adds nor subtracts heat from the substrate, and acquires a time constant very close to the intrinsic time constant of the absorber. This has the advantage of gaining very good energy resolution, but gives up the position sensitivity of the QET's. The precise transition temperature also becomes an issue when operating large numbers of these detectors at once. To overcome this problem, the Munich Group has developed an alternate form of temperature feedback using a thin gold film heater placed very near the tungsten SPTT. This leads to

a significant speed up, less susceptibility to transition temperature, and Johnston noise suppression as is found in the electrothermal feedback systems. In addition to this advancement, a recently developed discrimination scheme shows enormous promise. By using two SPTT's, one placed on a crystal of BaF scintillator, and one placed on an adjacent silicon wafer, they are able to measure the simultaneous production of photons and phonons in their absorber. The production of photons is severely depressed in nuclear recoils when compared with electron recoils (similar to the charge-based discrimination of CDMS and Eidelweise), and appears to allow a separation of the two types of events at the 99% level. The most promising piece of information is that electrons striking the surface of the $CaWO_4$ do not produce decreased scintillation light. Although these initial tests were done on a 2 g crystal extrapolating to the performance of a several kilogram crystal should not be difficult.

EDELWEISS

The EDELWEISS experiment is set in the Laboratoire Souterrain de Modane in the Fréjus tunnel between France and Italy. The technology utilized is similar to CDMS in that they employ simultaneous detection of heat and ionization at millikelvin temperatures to discriminate between gammas and nuclear recoils. The thermal measurement is made with NTD (Neutron Transmutation doped) thermistors and the ionization contacts are ion implanted p-i-n diodes. The p-i-n diodes allow the application of large voltages across the crystals which separate the nuclear recoil and beta signals[62]. To date they have instrumented one 70 g crystal with a phonon resolution of 1.2 keV. With a total exposure of 1.17 kg-days they have achieved a nuclear recoil upper limit of 0.6 kg/keV/day at 90% confidence[63]. This collaboration plans to instrument a series of 20 detectors in a newly constructed low background cryostat by the beginning of 2000.

1.2.3 Estimating Event Rates

The goal of these direct detection experiments is to go from a background rate measurement to an upper limit on the WIMP-nucleon cross section with a given mass. I will briefly review the formalism involved in this process following the standard treatments of Lewin and Smith, and Jungman *etal*[64, 55]. These formuli, along with a statistical method developed by our group will be applied in chapter 6 to actual data.

We will start by assuming an average density of WIMPs in the solar neighborhood of $\rho_W = 0.3\,\mathrm{GeVc^{-2}cm^{-3}}$. This is a fiducial density generally accepted by the community and is on the lower end of current estimates[65]. This allows us to compute a number density $n_o = \frac{\rho_o}{m_\chi}$ of particles that will impinge upon our detector. These particles will have random Maxwellian velocities up to the escape velocity ($\sim 600\,\mathrm{kms^{-1}}$) with a mean equal to the orbital speed of the sun around the galaxy of $v_o = 220\,\mathrm{kms^{-1}}$. Since the velocities are so gentle, the recoil energy from a WIMP elastically scattering off an earth bound nucleus is describable by simple first year kinematics

$$E_r = \frac{\mu^2 v^2}{m_N}(1 - \cos\theta) \tag{1.23}$$

where v is the velocity of the WIMP with respect to the earth, μ is the reduced mass of the WIMP-nucleon system ($\mu = \frac{m_\chi m_N}{m_\chi + m_N}$), and m_N is the mass of the target nucleon. We can further assume isotropic scattering so that the differential rate (per unit recoil energy) is

$$\frac{dR}{dE_r} = \frac{m_N}{2\mu^2}\int_{v_{min}}^{v_{max}} \frac{1}{v^2} dR(v) \tag{1.24}$$

where $v_{min} = \sqrt{\frac{m_N E_r}{2\mu^2}}$. The Rate of interaction is merely the flux times the cross section

$$R = < v > n_o \sigma_o = < v > \frac{\rho_o}{m_\chi}\sigma_o \tag{1.25}$$

here we assume a Maxwellian form for $< v >$ so

$$< v >= \frac{1}{2\pi^{3/2} v_o^3} \int v e^{-v^2/v_o^2} dv^3 \tag{1.26}$$

Substituting from Eq. 1.26 into Eq. 1.24 we obtain

$$\frac{dR}{dE_r} = \frac{\sigma_o \rho_o}{2 m_\chi \mu^2} \int_{v_{min}}^{v_{max}} \frac{1}{v} e^{-v^2/v_o^2} dv^3 = \frac{\sigma_o \rho_o}{\sqrt{\pi} v_o m_\chi \mu^2} \exp\left(\frac{-E_r m_N}{2\mu^2 v_o^2}\right) \tag{1.27}$$

when v_{max} is infinite. This is the justification for an exponential energy distribution expected in any WIMP search experiment, and the argument for as low a threshold as possible. We can write the differential rate in a more general way[55]

$$\frac{dR}{dE_r} = \frac{\sigma_o \rho_o}{\sqrt{\pi} v_o m_\chi \mu^2} T(E_r) F^2(E_r) \eta(E_r) \tag{1.28}$$

where T, F, and η are dimensionless functions that absorb the details of kinematics, exact form of the cross section as a function of energy for a given target material, and detector characteristics. For scalar interaction, we use the Woods-Saxon form factor

$$F(E_r) = 3 \frac{j_1(E_r/\hbar c)}{E_r r_n/\hbar c} \exp\left(\frac{-(E_r s/\hbar c)^2}{2}\right) \tag{1.29}$$

where $r_n \sim (0.89 \mathrm{A}^{1/3} + 0.3)\,\mathrm{fm}$ and $\mathrm{s} \sim 1\,\mathrm{fm}$, and

$$T(E_r) = \exp\left[-(\frac{v_{min}}{v_o})^2\right] \tag{1.30}$$

but can encompass all the details of velocity peaks, and galactic escape velocity cut offs and modulation effects. It is then with equation 1.28 that we transform any measured differential rate in the lab to a limit on the cross section, σ_o.

Chapter 2

Detector Overview

2.1 Phonon Measurement

The idea of utilizing the athermal phonons generated in a low temperature crystal as a particle detector is not a new one.[66, 67, 68, 69] The essential advantage of these detectors is that the quanta of energy being generated (the phonon) is much smaller than that of scintillation or ionization mediated detectors. The typical energy to create a scintillation photon is $\sim$100eV, to create an electron-hole pair in a semiconductor is $\sim 3\,\mathrm{eV}$, whereas phonons are much lower energy $\sim 1\,\mathrm{meV}$. The resolution limit that arises in ionization detectors of $\sigma > \sqrt{FN}$ is therefor not an issue. In chapter 7 we will discuss a first attempt to create a discriminating detector that does not employ charge readout.

2.1.1 Phonons in crystals

Phonons are to vibrations in a lattice what photons are to electromagnetic disturbances in a vacuum. They are merely the particle manifestation of continuum acoustic phenomenon, or depending on your philosophy, they are the exchange particles

of heat that manifest themselves as bulk waves. A phonon can be represented by its wave vector k, a frequency ω, and a polarization ϵ. The polarization vector divides phonons into three types: longitudinal (L); fast transverse (FT); and slow transverse (ST). The thermal average number of phonons in a given mode of frequency ω is given by the Planck distribution:

$$\bar{n} = \frac{1}{exp(\frac{\hbar\omega}{k_B T}) - 1} \tag{2.1}$$

where temperature is the critical parameter to determine both the peak of the distribution (at $\hbar\nu = 2.8 k_B T$) and the total energy. At 30 mK phonons at the peak of the Planck distribution have an energy of 7.5μeV. Thus, at these temperatures, the only detectable phonons are those that are extremely out of equilibrium.

When a particle interaction occurs in a low temperature crystal, phonons are generated at or near the Debye energy (13.4 THz in Si). These phonons then quickly decay by splitting into two phonons of lesser energy. This process has a rate that depends highly on frequency[70] and can be written as:

$$\tau_D = \tau_{D-1THz} \frac{1THz}{\nu}^5 \tag{2.2}$$

where τ_{D-1THz} is Dependant on the phonon mode and the frequency. For silicon L-mode phonons decay with $\tau_{D-1THz} \sim 8.6\mu s$. The probability distribution is governed by

$$P \propto E_f^2 (E_i^2 - E_f^2) \tag{2.3}$$

where E_i is the energy of the initial phonon and E_f is the energy of one of the final phonons.

The dominant scattering mechanism of any measurable phonons in a crystal such

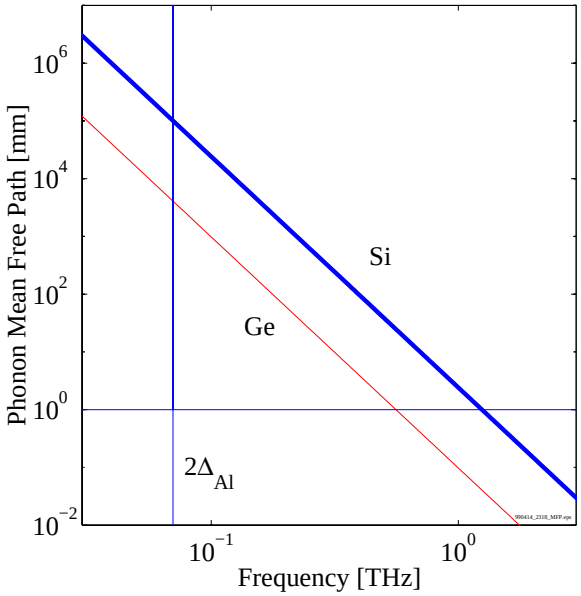

Figure 2.1: A plot of phonon mean free path versus phonon frequency for Silicon and Germanium. Vertical line is the $2\,\Delta_{Al}$ energy threshold. Horizontal line is at 1 mm. Taken from Wolfe [71]

as silicon is elastic isotope scattering. The isotopic abundance of naturally occurring silicon is 92.2% ^{28}Si, 4.7% ^{29}Si, and 3.1% ^{30}Si. Using perturbation theory, it can be shown[72] that

$$\tau_I \propto f_i(1 - \frac{m_i}{\bar{m}})^2\omega^{-4} \tag{2.4}$$

where f_i is the fraction of the dominant isotope and m_i is its mass. This leads to the value of $\tau_{I-1THz} = 0.41\mu s$[70]. The probability distribution for this process is weighted by the polarization vectors, ϵ_1 and ϵ_2 , of the initial and final phonons and the phase velocity V_p of the final phonon,

$$P \propto \frac{(\epsilon_1 \cdot \epsilon_2)^2}{V_p^3} \tag{2.5}$$

Note that the phase velocities are different for the different modes (L $\sim 9\frac{mm}{\mu s}$, FT and ST $\sim 5.9\frac{mm}{\mu s}$). The combination of isotopic scattering and anharmonic decay leads to what is known as the quasidiffusion of phonons, where a phonon will diffuse through isotopic scattering and then decay. A 1.5 THz phonon, for example, will have a lifetime of $\sim 1.1\,\mu$s and will scatter on average 14 times diffusing a distance of 1 mm.

It can be shown that the phonons that reach the surface of a macroscopic sample (as our 1cm thick detector) tend to toward a 'bottleneck' frequency[73] ν_{BN} of about 1.6 THz. In addition, the mean time of arrival of these phonons is roughly 3 times the ballistic time (t_b).

The phonons generated from initial particle interactions are thus rather high frequency ($\sim$ THz) and rather diffusive. As discussed later in section 2.1.2 only phonons above an energy of $2\Delta_{Al}$ or ≈ 120 GHz can be seen in our detector. This leaves many phonons that are above the intrinxic threshold of the detector, but yet, due to the extreme frequency dependence of the scattering length, travel ballistically. The data in chapter 5 supports the existence of such lower frequency phonons generated during the special class of events that occur near the surface of the detector.

An entirely different class of phonons are generated by electron-hole pairs drifting through the crystal (Sec.2.2.1). When a photon interacts with a K-shell electron of the silicon lattice, dumping E_γ energy, $\approx E_\gamma/3.8$ electron-hole pairs are eventually produced (fewer for neutrons, again see Sec.2.2.1). The small electric field that is applied to the crystal causes the charges to accelerate up to the speed of sound and scatter inelastically with the lattice. This generates what are known as 'Luke' phonons[74] (Actually predicted earlier by Neganov[75]] but, as we in the west, the

name sticks). Thus, during practical operation, for each event of energy E_γ we actually measure $E_\gamma \cdot (1 + y \cdot \text{eV})$ of phonon energy. (This statement assumes that we recover the 1.1 eV of gap energy from the charges recombining at the surface. Data in chapter 5 is shown in confirmation.) The frequency distribution of this additional 'Luke' component ($E_\gamma \cdot y \cdot \text{eV}$) can be calculated[76]. For $\sim$1-2 V/cm range where we operate, the mean frequency of generated phonons is predicted to be ≈ 0.25 THz. This would correspond to a mean free path of ≈ 50 cm. Data shown in chapter 5 represents a confirmation of the frequency difference between initial phonons and 'Luke' phonons.

2.1.2 Quasiparticle Trapping

When the non-equilibrium phonons reach the surface of the detector, we must find some way of channeling this energy into the active tungsten elements. We do this by taking advantage of a technique called quasiparticle trapping originally proposed by Booth[77] in 1987. Phonons enter the large ($\sim$1mm) aluminum collector fins and scatter with the cooper pairs creating quasiparticles and sub-gap ($E_{ph} < 2\Delta_{Al}$) phonons. The quasiparticles then diffuse until they reach a region of the fin where a reduced gap has been created. When the quasiparticle reaches this region it can inelastically scatter, (either off another quasiparticle or by emitting a phonon) and lose energy to be trapped (see Fig.2.2). It then must diffuse to the edge of the trap region and scatter again to be trapped in the pure tungsten region. We then rely on diffusion to take the non equilibrium quasiparticles in the tungsten spurs (see Chapter 4 for a description of the exact device geometry) to the current carrying portion of the TES to cause a resistance change. It is critical to the success of these detectors that we estimate the efficiency of the above process. Let us examine the constituent parts in more detail.

First, we must convert phonons to quasiparticles in the Aluminum film, ie. the

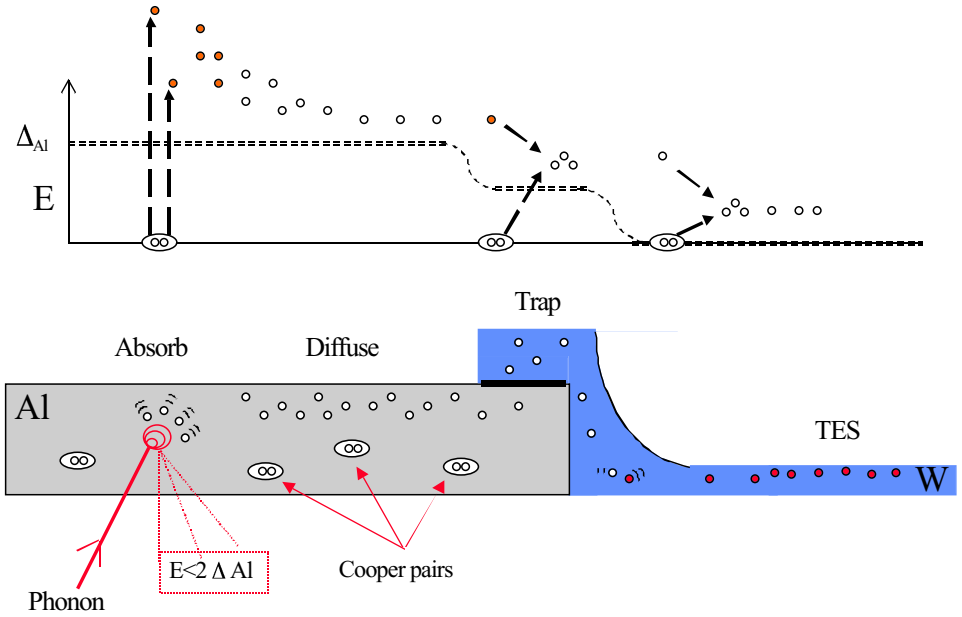

Figure 2.2: Gap diagram and Quasiparticle Trapping Cartoon. 1. Phonons enter the aluminum film creating quasiparticles. 2. Quasiparticles diffuse to the trap, losing energy and dying on the way. 3. Quasiparticles trap in the reduced gap region of the W/Al interface region. 4. Quasiparticles deposit their energy in the TES.

phonons must enter the aluminum film, be above $2\,\Delta_{Al}$ and scatter with a cooper pair. The transmission process is governed by acoustic mismatch theory[78] and is likely to be faily accurate given the assumption that there is no additional scattering due to a poorly made interface (see chapter 3). Estimates of the rate of phonon pair breaking can be found in Kaplan [79] which agree well with preceding experiments[80]. The mean free path of THz phonons in Aluminum films was measured most recently by Mrzyglod and Wies [81] under similar conditions as in our detector. The energy loss in the phonon-quasiparticle conversion process is also of concern. Phonons of high energies ($1\,\mathrm{THz} \sim 28\Delta_{Al}$) will tend to create quasiparticles far above the gap energy. These initial quasiparticles will then scatter creating more quasiparticles in a cascade process. The similarity between the quasiparticle-quasiparticle and

the quasiparticle-phonon scattering rates leads to the production of many sub-gap phonons during this cascade process. These phonons represent a real loss to the detector since they will never be reabsorbed. Best estimates for the efficiency of this process is $\sim 50\%$[82].

Second, the quasiparticles must be long lived and arrive at the TES. This depends upon the mean free path, λ, and the effective lifetime, τ_{qp}, of the quasiparticle. To estimate the mean free path we note that the residual resistance ratio ,$\Re$, of our 150 nm was measured to be ~ 10. Since

$$\lambda = \frac{\Re m^* v_F}{ne^2 \rho_{300K}} \approx \Re(15\, nm) \tag{2.6}$$

we have a λ consistent with being thickness limited. From $\Re$ measurements of larger thickness aluminum under the same conditions and in the same machine as was used for our detector[83] we can claim that a λ of 400 nm is achievable. The diffusion length, L, can be estimated by comparing the signal ratio in a two detector experiment[84]. We performed an experiment of this kind using two tungsten TES detectors and a 350 μm Al absorber made in the same fabrication cycle as our primary dark matter detector.

When, and if, the quasiparticle reaches the trap region, it must enter the reduced gap area of proximitized tungsten, and scatter inelastically to an energy less that Δ_{Al} order to be trapped. The transmission coefficient across the W/Al interface was of great concern to us in terms of fabrication, and many steps were taken to ensure a clean boundary (See chapter 3). When the quasiparticle loses energy, it can do so by scattering with a cooper pair (If the proximitized gap is less than $\Delta_{Al}/3$) or it can emit a phonon. If the later process happens it represents a real energy loss to the system and is therefor referred to as 'bad' trapping. The energy conserving mechanism is referred to as 'good' trapping.

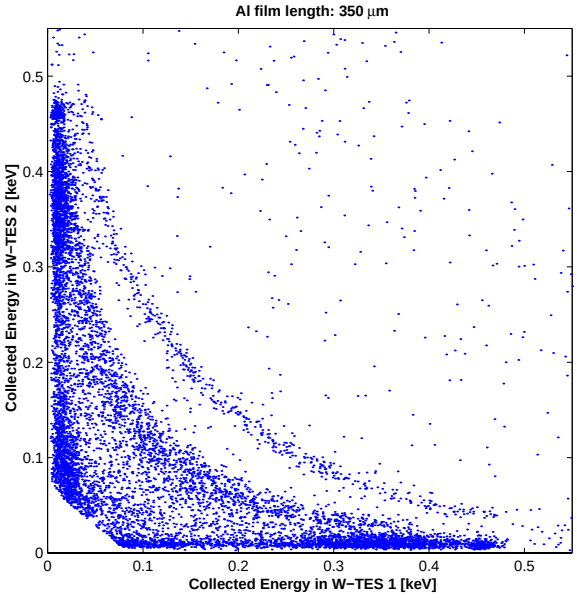

Figure 2.3: Energy in TES-1 versus Energy in TES-2 for 1.2 keV xrays. A number of features in the plot allow us to estimate the transmission probability, trapping probability, and diffusion length in our aluminum films (see text).

To estimate the efficiency of the majority of the processes involved in quasiparticle mediation, we constructed a specialized device consisting of two tungsten TES detectors placed on either end of a 350 μm long aluminum absorber. Low energy X-rays from a fluorescence source hit the aluminum absorber and quasiparticles diffuse into the TESs at either end. Figure 2.3 shows data collected from such a device. I will describe several features that are of interest. First, the outermost curve is formed by the events hitting the aluminum directly. The more solid curve below it are the substrate events. The fact that this is less than a factor of two below the Al events shows a high efficiency for phonon-quasiparticle conversion. Second, the curvature of the band suggests a rather large loss of quasiparticles across the modest distance of 175 μm. Since the size of the aluminum fins in the dark matter

detector are $\sim 1\,\mathrm{mm}$ this led us to the conclusion that most of the total signal loss was from the small quasiparticle diffusion length (measured to be $\sim 180\,\mu\mathrm{m}$). At either extremes of the distribution we can compare the direct hits in the TES with events close by in the aluminum. The fact that these are roughly of equal energy suggests a highly efficient trapping process. Examining the distance in y-energy (TES-2) between the TES events at large x-energy (mostly TES-1) we can say that an event in the aluminum close to the TES does not transmit much of its energy back to the other TES. This is equivalent to a good transmission probability for the W/Al interface. For a more detailed discussion on obtaining the values of these parameters (transmission probability, diffusion length, and trapping efficiency) see Kraus[84], and for a more detailed discussion of these data see ref. [85].

2.1.3 ETF-TES

The fundamental concept of electro-thermal feedback is that the tungsten element is voltage biased and self heats above the ambient substrate temperature. This leads to the classic balancing equation

$$c_v \frac{dT}{dt} = \frac{V_{bias}^2}{R(T)} - \kappa(T^n - T_s^n) \tag{2.7}$$

where c_v is the relevant heat capacity of the superconductor, T is the temperature of the sensor, V_{bias} the voltage bias across the TES, $R(T)$ is the resistance of the sensor, T_s is the temperature of the substrate, and n is the conductivity exponent. For tungsten TES sensors with transition temperatures of $\sim$100mK electron-phonon decoupling is the dominant thermal impedance. Thus c_v refers to the heat capacity of the electron system, and n=5. See chapter 7 for an attempt to measure the value of n for a sensor of this type. For a small perturbation δT about the bias point the equation becomes[86]

$$c_v \frac{d\delta T}{dt} = -\frac{P_o \alpha}{T}\delta T - g\delta T \tag{2.8}$$

where P_o is the equilibrium power flowing into the substrate, $\alpha = \frac{TdR}{RdT}$ the dimensionless quantity that describes the sharpness of the transition, and g = $n\kappa T^{n-1}$ the thermal conductance to the substrate. Through this non-equilibrium approximation, and using $P_o = \kappa T^n$ for extreme self heating, we can see that Eq. 2.8 leads the classic speed up equation

$$\tau_{ETF} = \frac{\tau_o}{1 + \frac{\alpha}{n}} \tag{2.9}$$

where τ_o is the standard $\frac{c_v}{g}$ time constant for an object returning to thermal equilibrium.

Since the total power admitted into the TES can be computed with no free parameters from the integral of the pulse...

$$E_{TES} = V_b \int \delta I dt \tag{2.10}$$

It is clear that to maximize signal to noise one must bias the sensor with as low a voltage as possible since $\delta I \propto \frac{\delta P}{V_b}$. This approximation is true if the time constants elsewhere in the system (ie: quasiparticles or phonons) are much slower than the TES time constants. We continue this simple analysis in the next section to examine the impact of different T_c's on the signal to noise of a TES-based dark matter detector. The major result is that the noise limit deviates from the pure ETF formula of

$$\sqrt{4k_B T^2 C(\sqrt{n/2}/\alpha)} \tag{2.11}$$

due to the fact that the time scale of a pulse (energy measurement) is not determined

by the ETF time scale, but by the slower phonon and quasiparticle time scales of a real dark matter detector.

2.1.4 Modeling DC characteristics

Using a very simple model one can duplicate almost exactly the I-V characteristics of a TES. The form for R_s as a function of T was chosen to be a Fermi-like function...

$$R_s = \frac{R_n}{2}(\tanh(\frac{T - T_c}{w}) + 1) \tag{2.12}$$

This is a good approximation to actual measured curves[87] and is likely to break down only at very low resistances. We can then iteratively solve the equation

$$\frac{I_b^2 R_b^2 R_s(T)}{(R_s(T) + R_b + R_p)^2} = \kappa(T^5 - T_s^5) \tag{2.13}$$

to find R_s(T) for a given bias current.

Shown in Fig.2.4 are the predicted Voltage vs. Current, Voltage vs. Resistance, and Voltage vs. Power for TES sensors with four different T_c's. The other parameters were chosen to be close to those of the 100 g silicon detector, $R_n = 2\,\Omega$, w=1.4 (3 mK 10-90 width), $T_s = 30$ mK, $R_b = 20$ mΩ, $R_p = 15$ mΩ, and κ=$\gamma V = 1.8\ 10^{-8}$ (measured for our detector, giving $\gamma = 1.9\ 10^{-12}$ [WK$^{-5}\mu$m^{-3}] with a volume of 7.8 $10^3\ \mu$m^3.

The Johnson noise of the sensor circuit can be expressed simply in terms of the relevant resistances[87].

$$i_n^2 = \frac{4kT_s}{R_s}\left(\frac{R_s}{R_s + R_p + R_b}\right)^2 + \frac{4kT_s}{R_b}\left(\frac{R_b}{R_s + R_p + R_b}\right)^2 + \frac{4kT_s}{R_p}\left(\frac{R_p}{R_s + R_p + R_b}\right)^2 \tag{2.14}$$

Using this noise estimate (which ignores the Johnson noise suppression from ETF)

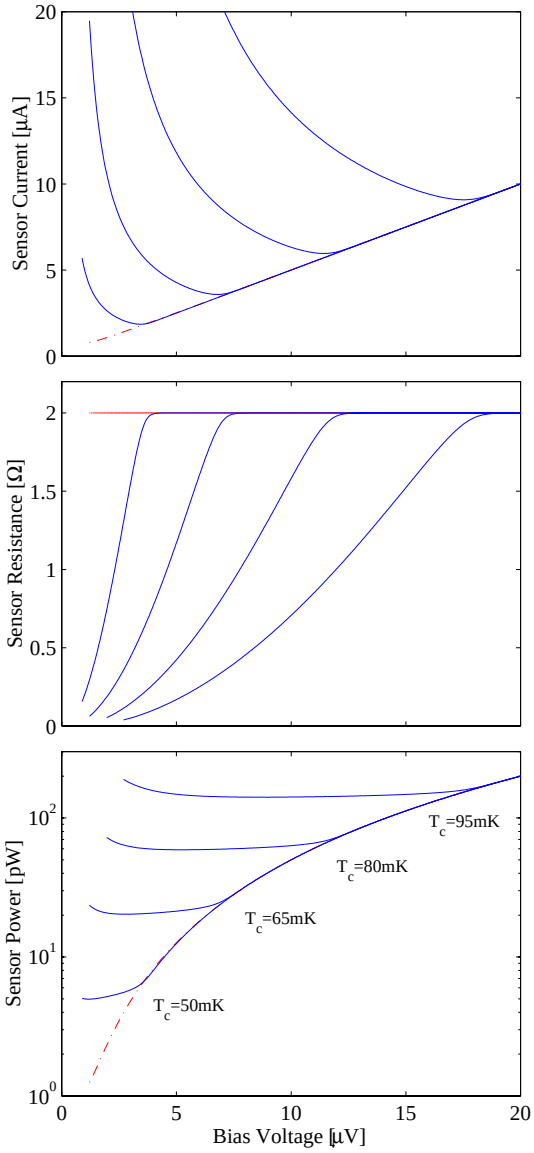

Figure 2.4: The DC behavior of 4 different W TES sensors with different T_c's. This is used in Fig.2.5 to display the effect of T_c on signal to noise.

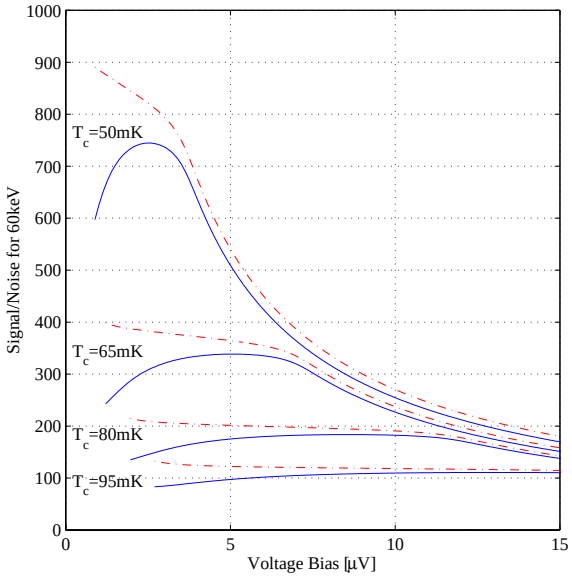

Figure 2.5: A plot of signal to noise versus V_b for TES sensors with different T_cs. The maxima of these curves agree closely with the T_c^3 law predicted from standard thermodynamic analysis.

we plot in Figure 2.5 the signal to noise as a function of voltage bias for sensors with different T_c's (Fig.2.4). Note that Figure 2.5 assumes the same bandwidth for each sensor, and that the signal current will scale as $\frac{\delta P}{V_b}$ as suggested in equation 2.10. For the sake of argument we can construct an ideal sensor dominated by it's own Johnson noise. This leads to the ideal resolution of

$$\sigma = T_c^3 \sqrt{\gamma V 4 k_b \tau_{ph}} \tag{2.15}$$

which is valid as long as the phonon time scale dominates and does not change. Note that this assumes 100% collection efficiency. Also note that this analysis suggests that running a sensor with a high T_c at an elevated temperature could gain back signal/noise (due to the increased relevance of P_o). This is true as long as the

intrinsic heat loss time scales τ_o do not become comparable to τ_{ETF}. In this extreme case signal will be lost due to the sensor's inability to measure it. One can write the τ_{ETF} with a finite substrate temperature as

$$\tau_{ETF} = \frac{\tau_o}{1 + \frac{\alpha}{n}(1 - (\frac{T_s}{T_c})^4)} \tag{2.16}$$

writing the fraction of signal that the detector can measure (ie. that does not get lost to the substrate) as

$$f_s = \frac{\tau_o}{\tau_o + \tau_{ETF}} \tag{2.17}$$

adding this loss term, and recalculating equation 2.15 to include a finite temperature substrate, we find the fundamental resolution of

$$\sigma = \sqrt{\gamma V (T_c^5 - T_s^5) 4 k_b T_c \tau_{ph}} \left[\frac{2 + \frac{\alpha}{n}(1 - (\frac{T_s}{T_c})^4)}{1 + \frac{\alpha}{n}(1 - (\frac{T_s}{T_c})^4)} \right] \tag{2.18}$$

2.2 Ionization Measurement

Although fundamentally a noisier and more limited technology, measuring the induced charge along with phonons is necessary at this point to obtain discrimination. The major difficulty of this type of duel phonon-charge detector is that charge must be collected under extremely low voltages in order that the induced 'Luke' phonons not pollute the initial signal. I will briefly describe the state of the knowledge on low temperature, low voltage charge collection.

2.2.1 Charge Collection

Crystals of high purity semiconductor material at these temperatures become completely insulating. This is because of the lack thermal excitations necessary to populate the conduction and valence bands. The 'freeze out' temperature for silicon tends to be between 4 K and 10 K depending on the dominant dopant and between 1 K and 4 K for germanium. The crystals are as high purity as possible to create as uniform a Fermi surface as possible.

When the sample is initially cooled down the crystal is in a state typically referred to as 'Mode I'. Charge collection is poor, requiring large voltages, and drift times are large. Drift times on the order of several microseconds (from signal rise times) have been observed. In Mode I and in very impure crystals (ρ <2 kΩ-cm) a simple trapping model works quite well[88] where the charges diffuse and are trapped along the drift path by impurity sites. This leads to a position dependant signal

$$\frac{S(z_o)}{Q_o} = \frac{\lambda_e}{d}(1 - e^{-z_o/\lambda_e}) + \frac{\lambda_h}{d}(1 - e^{-z_o/\lambda_h}) \tag{2.19}$$

where S(z_o) is the charge signal, compared to the total Q_o, and λ_e, λ_h are the trapping lengths of the electrons and holes, and d is the thickness of the sample.

When the sample was irradiated or illuminated with the right frequency of light from an LED[87] the charge collection improves dramatically. This is attributed to the filling of potential charge trapping sites by the induced electrons and holes. The irradiation dose (and presumably the LED time, although this was never tested) scaled roughly linearly with the purity of the crystal. One the surprising things about the progression from Mode I to Mode II is that the phonon signal increased roughly 20%. In fact the effect was originally discovered in a phonon sensor by A.T. Lee during bombardment by a VanDeGraff accelerator.

The most surprising result of M. Penn's findings, which must be restated here, is

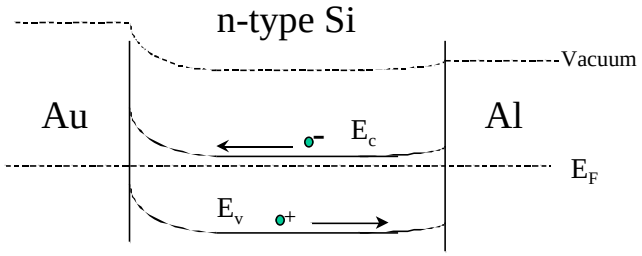

Figure 2.6: A band diagram of the silicon ionization system. The barrier on the aluminum side is zero or very small.

that for very pure samples ($\rho > 20$ kΩ-cm) the signal loss was virtually independant of the thickness of the sample. The obvious interpretation was that most of the charge was being lost in the initial e-h cloud when the electric field could be effectively shielded out.

By comparing the rate of coincidence in a split detector, M. Penn was able to estimate the size of the charge cloud in Si and its dependance on electric field. In high purity Si charge clouds of 1 mm are the minimum diameter. This constrained some of the electrode geometry, discussed in chapter 3.

The phonon sensor itself is mostly aluminum and the backside was covered with gold (ignoring a very thin titanium sticking layer). These two metals comprised the Schottky barriers of the ionization system depicted in figure 2.6. Work function estimates of gold range from 5.1-5.4 eV[2], aluminum from 4.1-4.4 and silicon from 3.9-4.2. The schottky barrier on the gold side then is ~ 1 eV or approximately the size of the band gap. The schottky barrier on the aluminum side is zero or very small.

Chapter 3

Design and Fabrication

This section will outline in detail the physical geometry and fabrication issues of the FLIP design known as the 'Alex' design. A previous design was attempted in a 100 g format, but many problems associated with its design. Details of this older design can be found in the PhD thesis of Sae Woo Nam[87] and in the work of B. Chugg[89]. I would like to thank Paul Brink for his invaluable help during the design and construction of this device. Many subtle issues would have escaped me if not for his patience. I would also like to thank Barron Chugg for many useful discussions on the specifics of processing thick wafers.

3.1 Basic Design Constraints

In order to create the most efficient phonon detector, we believed it necessary to cover the maximal surface area with aluminum collector elements. Since the diffusion length of quasiparticles in aluminum was finite (and at the time of the design, unknown) we endeavored to minimize the area of each individual collector fin. This required maximizing the number of TES elements that would be fed by these collector fins. The number of TES elements that can be connected in parallel in a detector

is limited, however, by a combination of the stability criterion[87] and the L/R time constant of the SQUID readout circuit. Conservatism forced us to accepted a maximum length of 250 μm for a stable TES. The actual maximum length should be measured but this has not yet been done (see chapter 8). For an L/R time constant of $\sim 1\,\mu$s, the operating point must be $\sim 0.2\,\Omega$ for the input inductance of our present SQUID input coils (L = 0.25 μH). To maintain a high α (see chapter 2) we wished to bias the TES at $\sim \frac{1}{5}$ of its normal resistance. This constrained us to an R_n of about an Ohm.

Given the resistivity of our tungsten ($\sim 5\,\Omega/\Box$ at 35 nm thickness) the maximum length of 250 μm limited the total parallel width of TES to around 1.2 mm. Combining this with the practical value of $\sim 2\,\mu$m for a comfortable photolithographic linewidth we were limited to about 500 total TES elements. To cover the 10 cm^2 of surface area on one quadrant of a 3 inch wafer then required each TES to be fed by about 2 mm^2 of aluminum. Below is a detailed account of our attempt to satisfy these design constraints.

3.2 Design Geometry

The 'phonon side' of the detector is divided into an 'active' area, the QET region, and a 10% area coverage tungsten outer grid. The W grid was patterned in the final W layer (see chapter 3) into a 200 μm long 20 μm wide grid. To avoid an asymmetry, the orientation of this grid was rotated to form a parquet pattern. Maintaining metalic coverage as far out to the edge of the wafer was a prerequisite to ensure good electric field uniformity for the ionization sensor. The irregularity of the photoresist near the edges of the crystal limits ones ability to place active elements there. This necessitated a passive outer grid. In the original FLIP design, the outer electrode consisted of a solid layer of the 35 nm W. This lead to a factor of two in phonon

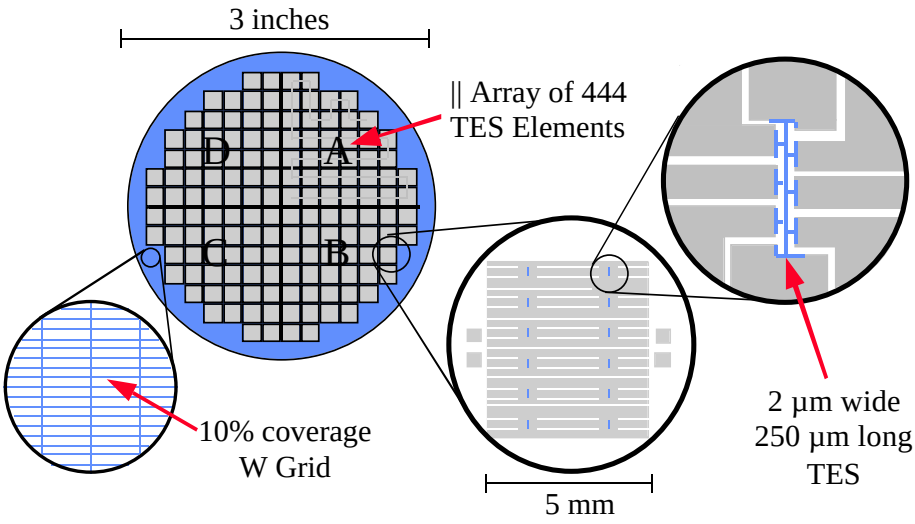

Figure 3.1: A diagram of the phonon sensor side of the Alex design. The surface is divided into active area and an outer W grid. The active area consists of 4 independent readout channels each composed of 37 - 5 X 5 mm individual dies. Each of the dies has 12 QET elements each leading quasiparticles to a 2 μm wide W TES.

losses at the crystal edges which was the motivation for a sparsified grid design. The grid needed to be on a fine enough scale so that non uniformities in the electric field did not penetrate the silicon. The confortable photolithographic limit of 2 μm wide features and the constraint of 10% coverage completely determined the design. The signal losses near the edges of the detector did improve dramatically in the new design (see chapter 5) implying that little or no down-conversion occurs at the bare silicon surface.

The active sensor area is divided into 4 quadrants, each with its own independent bias and associated electronics channel (commonly denoted as A,B,C and D). The decision to partition the sensor into four separate channels was motivated by the success of the smaller 2 X 2 detectors developed by S.W. Nam. Position sensitivity

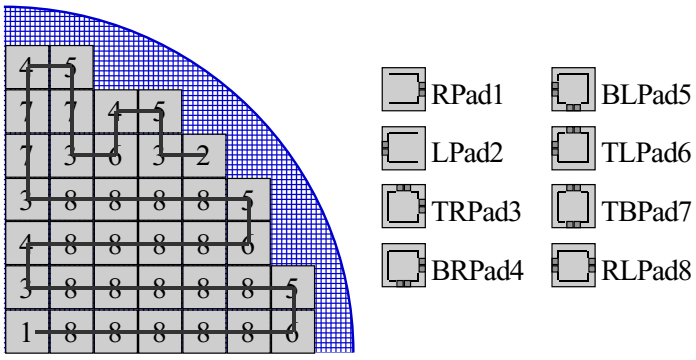

Figure 3.2: One channel of the phonon sensor side with interconnectivity pattern. Eight separate dies (shown on the right) are necessary to complete the snake pattern in each quadrant. The other quadrants are merely mirror images of these quadrants. Because of the limitations of the ultrastep1000 we are forced to double the number of masks to 16 (see Fig. 3.3).

has the enormous advantage of being able to identify a radioactively 'hot' component located close to the detector. In addition, position sensitivity has allowed us to put much more stringent constraints on any Monte Carlos predictions of the low background environment. For a demonstration of this please see the photon calibration section of chapter 5.

Each quadrant was divided into 37 interconnected 5 X 5 mm dies. The reason for this was the fundamental limitations of the ultrastep 1000 aligner (see following section). This was the only aligner that had been modified to accept 1 cm thick wafers. It possessed excellent alignment accuracy ($\sim 0.1\,\mu$m) but was very particular about the details of the alignment marks. In order to be able to stitch together many independant fields, B. Chugg was able to use overlapping vertical alignment marks (VAMS). Since each mark could be both a left and right alignment mark this created a doubly exposed region around the edges of each die of $200\,\mu$m. Each mask then had opaque areas it would leave unexposed and could create a connection between adjacent dies. The minimun distance between VAMS that the ultrastep allowed was

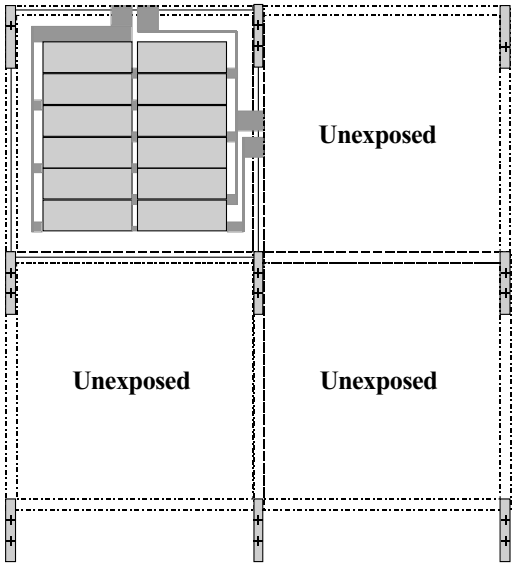

Figure 3.3: A diagram of a single 5 mm die. In order to achieve the 5 X 5 mm geometry we needed to fool the ultrastep into thinking it was exposing over a 1 cm grid. Note: each alignment mark is simultaneously a left and right mark. The die shown is l_TRPad3. See text for an explanation of the different dies.

1 cm. In order to stitch a pattern that was composed of 5 X 5 mm squares, we had to fool the ultrastep into thinking it was dealing with a 1 cm field (see Fig. 3.3). Each 5 X 5 mm square in a mask was actually embedded in a 1 X 1 cm field with only one quadrant containing the pattern. Note that figure 3.3 shows the 12 individual elements within the 5 X 5 mm square all wired in parallel. The 37 squares were then connected together in the 'snake' pattern shown in figure 3.2. Eight fundamental dies are necessary to produce virtually any interconnection pattern (see Fig. 3.2). Because of the limitations of the ultrastep1000 aligner the number was doubled to 16. It was found later that this doubling of alignment marks was not necessary due to the ability of the ultrastep to align with only one mark. The Alex design was nevertheless completed with the double mask set.

Inside each of the 5 X 5 mm squares were 12 QET elements connected in parallel

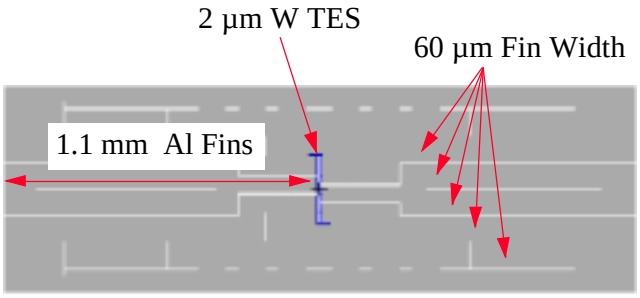

Figure 3.4: Diagram of a single QET element. The total width is 2.2 mm to give an 80% coverage of the 5X5 mm die. Fins are split into 60 μm bars to help prevent trapping of flux vortices.

(see Fig. 3.3). They were placed in the same relative position within each of the 16 dies so that only one tungsten die (2 masks) was required for the TES patterning stage. Figure 3.4 is a diagram of one of these QET elements. The total distance that quasiparticles must diffuse to reach the TES in the center is $\sim$1.1 mm. This was the smallest distance we could manage and still satisfy the philosophy of total aluminum coverage (see Sec. 3.1). We were also quite concerned about the possibility of trapped flux in the aluminum degrading the aluminum diffusion length[90]. For this reason we divided the aluminum into many thin strips of width less than 100 μm. If the aluminum was much wider than this, it was thought that the flux vortices would not feel a force from the decreased gap at the edges and would be free to form and create traps. The value of 100 μm came from P. Brink's previous experience with Al/Al tunnel junctions.

The dimensions of the quasiparticle trap region are shown in figure 3.5. Each TES is fed by eight quasiparticle traps. Two of the traps are situated at the extremes of the TES and also act as the voltage bias rails. The different fins must not be connected electrically inorder to maintain a smooth voltage drop across the TES. Part of the reason for dividing the trap section into eight was to limit the aluminum

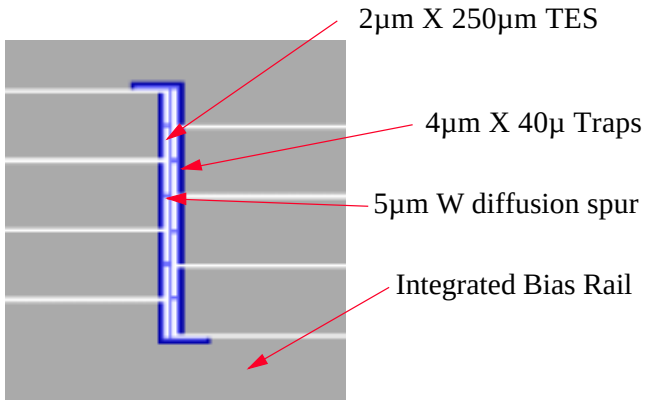

Figure 3.5: A close up of a single QET element showing the W TES, the quasiparticle trap dimensions and the W diffusion spur. The voltage bias rail is integrated into the bottom and top quasiparticle fins.

width as discussed above, but it was also done to limit the total diffusion distance to the spurs after trapping. Since the elastic mean free path of quasiparticles in the tungsten was far shorter than in the aluminum (roughly by the ratio of the 4 K resistivity, $\sim$). It was estimated that the length of time for the quasiparticles to traverse the 20 μm to the tungsten spur was about 2 μs.

3.3 Fabrication

This section is designed to highlight the specific fabrication methods that were developed for the 100 gram silicon detectors and to briefly overview the steps in manufacturing a general QET detector. For more complete description of the fabrication process please be referred to the fabrication page of the CDMS web site or the numerous CDMS notes on the topic.

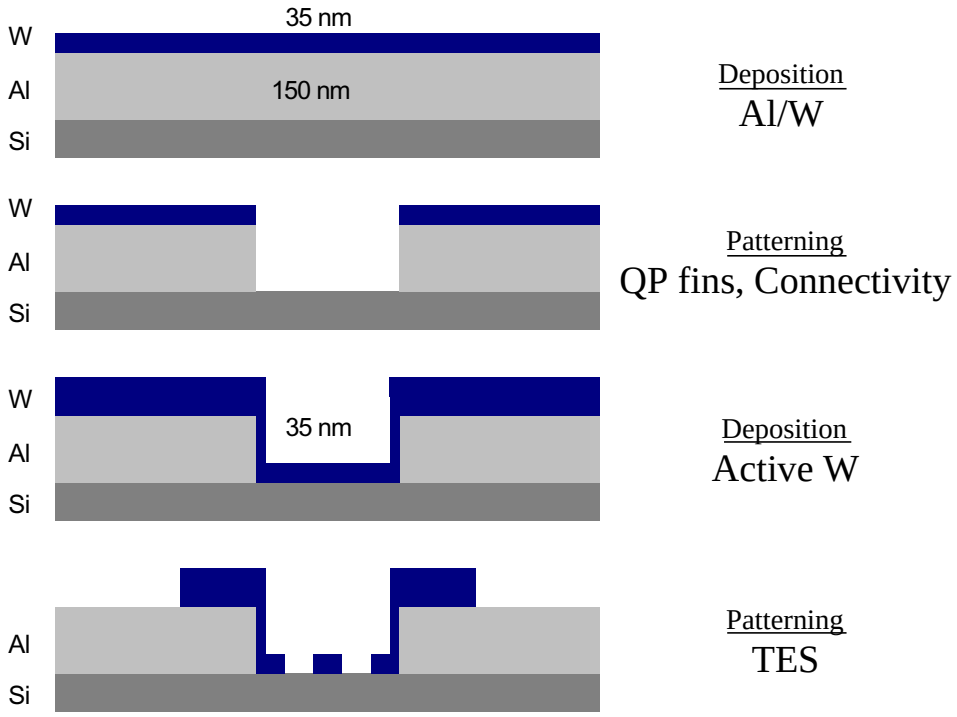

Figure 3.6: A diagram of the four basic steps involved in processing a silicon QET detector. The complications that arise in each of these steps are discussed briefly in the text.

3.3.1 Processing

There are four basic steps in the production of a QET phonon detector: deposition of the aluminum/tungsten bilayer, etching of the fin and interconnection pads, deposition of the final active tungsten, and the patterning of the TES and quasiparticle traps (see Fig. 3.6. This section will discuss each of these steps in more detail and hopefully elucidate some of the reasons for these exact proceedures.

Before a silicon wafer is placed in the Balzers sputtering chamber it must be cleaned. The standard cleaning at the center for integrated systems (CIS) is H_2O_2:H_2O at a 3:1 ratio repeated twice followed by an HF (50:1) dip to remove surface oxides. Care must be taken at this step to limit contamination and surface dirt which could

impede the transmission of phonons through the silicon/aluminum interface. The wafers are then loaded into the Balzers sputtering chamber.

Before the metal layers are laid down, surface oxides are cleaned off using an RF back sputter. We then deposit 150 nm of aluminum and 35 nm of tungsten in on step without breaking vacuum. It is important that we lay down these two layers at once to ensure an oxide free interface between the aluminum and tungsten. Any interface could impede the transmission of quasiparticles across the trap region and decrease the detector efficiency.

We then pattern the Al/W layer. This is a long and involved process due to the limitations (again) of the ultrastep1000. First, we must put alignment marks spaced at 5 mm over the entire wafer. This requires a prebake, photoresist application, resist bake, blind-stepped exposure in the ultrastep, development, hard bake, etching in H_2O_2 and aluminum etch, and a resist strip phase merely to START defining the features. Without going into the details of photolithography, there are a few steps that are significantly altered by the fact that we are processing on thick wafers. Bake times are significantly larger due to the increased heat capacity of the thick wafers. Normal prebake times for 300 μm wafers are 30 minutes. We increase this to about an hour for the 1 cm thick wafers. Spinning is also significantly more difficult. With spin speeds of 5000 RPM needed to create a 1 μm layer of Shipley 1813, we needed to manufacture a special vacuum chuck with a rubber o-ring. Precise manual centering is required to prevent disaster. In the next section we will discuss the modifications to the ultrastep to enable the exposure of 1 cm wafers. Development is done individually in a glass beaker. Etching and resist stripping takes place in the standard CIS chemical baths.

The formation of the aluminum fin geometry is done after reliable alignment marks have been laid down in the metal. We now use the 16 separated masks to define the snake pattern in the four quadrants of the wafer. This removes all metal

in the TES region to ensure a fresh surface for the active tungsten. We are left with Al/W everywhere we will eventually have quasiparticle fins and interconnection pads.

The wafer is then placed back in the Balzers for the deposition of the active tungsten. At this stage the cleanliness of the wafer and the chamber are paramount. The superconducting temperature of the tungsten is quite low ($\sim 100\,\mathrm{mK}$) so any contamination could cause a shift in T_c. Another group placed wafers with photoresist in the sputtering chamber and caused us to lose T_c for many months. The tungsten is sputtered while applying a -200 V DC bias to the wafers. This technique was developed by Kent Irwin to achieve the appropriate range of transition temperature. A DC bias is traditionally used to remove contamination, and has been strongly correlated to the tungsten T_c (see future work by B. Young and T. Saab). For a general discussion on the superconductivity of tungsten please be refered to the work of P. Colling[91] and others [92, 93, 94, 95, 96, 97]. Essentially there are three phases of tungsten, α-phase, β-phase, and γ-phase each with different superconducting transition temperatures. Thin films of β-phase tungsten can be made through evapouration with a T_c of 15 mK, close to the bulk value. Sputtered films have been produced with γ-phase tunsten and T_c of 4-5 K. Sputtering with noble gases (similar to our proceedure) have produced α-phase tunsten with expanded lattice sizes and high T_c's of 3-5 K. Our tungsten is almost certainly an admixture of two of the phases to create an intermediate T_c of 100 mK. Recent work of B. Young and T. Saab has also shown a strong (linear) correlation of the tunsten transition temperature with the volume density of ion implanted iron. This work gives us the ability to continuously tune T_c to a few millidegrees. In terms of the T^3 dependence of energy resolution this will enable us to create highly optimal detectors in the near future.

The tungsten grid is patterned during the same step as the TES elements. This is a blind step, since there are no alignment marks near the edge of the wafer. We

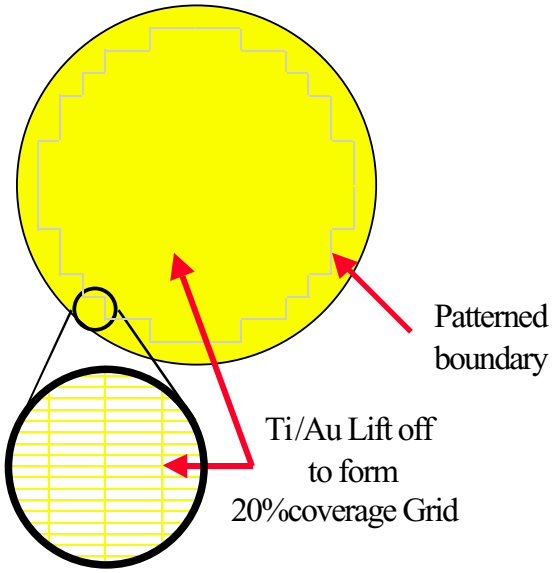

Figure 3.7: A diagram of the ionization side of the detector. A 20% area coverage grid is patterned with a barrier between the inner and outer electrodes. A thin Ti/Au layer is evapourated, then lifted off to define the back electrodes.

also leave behind some tungsten on selected interconnection pads to increase the reliability of the wire bonds. Tungsten is a much tougher material than aluminum and creates a hard crust for which the Al bond wire to weld.

The final processing step involves the patterning of the backside electrode for the ionization electrode. For the Alex design we used a lift off proceedure to define the grid and inner and outer electrodes. After the phonon side processing is completed, we cover the metal with a double layer of photoresist for protection. We then apply resist to the backside, placing the phonon side in contact with the spinner chuck. A lift off mask is created in the resist by exposing, soaking in chlorobenzene for 1 minute and then developing. The chlorobenzene hardens the top surface of the photoresist and inhibits development. The photoresist then gains the classic undercut profile of a liftoff mask. We then deposit a 5 nm titanium sticking layer followed by 25 nm of

gold. The depositions are done in the Ginzton clean room by T. Carver in an e-beam evaporator. The titanium is intended only as a sticking layer for the gold, and was made as thin as possible. The gold was also made as thin as possible and still have a continuous metalic layer.

The wafer was then placed in PRS1000 to remove the unwanted metal. Great care was taken to avoid floating pieces of gold from drifting on to the phonon sensor.

3.3.2 Equipment

As simple as our QET process is (just two deposition steps) it is utterly dependent on a few critical pieces of equipment. It is of utmost importance to the future of our project that these machines are maintained by CIS despite the outdated 3 inch wafer format that they employ.

SVG Coater

This is perhaps the machine that required the most minor modification, and is most easily replaced. A new wafer chuck was machined that employed an O-ring to increase to gripping force during spinning. Recently, the O-ring has been abandoned in favour of gripping side walls. This removes the possibility of misalignment, but allows photoresist to accumulate along the sides of the wafer. This is believed to contribute to residual metal not being removed during etching and the shorting of the outer electrode to the phonon sensor in recent detectors. Even though spinning a thick wafer seems like a trivial exercise, it is performed six times in the Alex process and must be repeated flawlessly to ensure good lithography. The SVG coater allows all automatic loading, baking and alignment features to be turned off, yet automatically applies the resist during a slow spin cycle. For these reasons it it ideal for our process.

Ultrastep1000

The ultrastep1000 is the bane of any sane person's existence. It features automatic alignment of incredibly high accuracy ($\sim 0.1\,\mu$m) but is very finicky about the details of the alignment marks to which it is presented. There is no camera mounted on the machine so the operator is unable to manually align and is completely subject to its every whim. At any moment it may decide that one of the 148 die positions on the wafer is unalignable due processing irregularities, trough depth, or anything. This is reasonably acceptable to the average processor who is producing 148 separate items that will be cut apart anyway, but is completely unacceptable to us who rely on the integrity of every field to produce a working detector. This is the first reason why we would be better off using a contact aligner. The second is that it would cut the number of photoresist applications dramatically. A contact aligner that could expose the entire wafer at once would not require the application of pre-alignment marks thus eliminating a step. The third reason is a dramatic increase in the freedom of design. We would no longer be constrained by 5 mm squares but could design the sensor to be as close to the circular edge of the wafer as possible. The interconnection pattern could also be made more robust through redundancy. The reason we have not moved to another aligner is merely because of the time and money already invested in the ultrastep. Traditionally, clean room users are very conservative about allowing modifications to a precision machine such as an aligner. This forces us to obtain modified chucks directly from the manufacturer instead of machining them ourself. Not only does this add expense but it adds time. Present estimates for the cost of modifying the chuck of a Karl Suss contact aligner to take 1 cm wafers are in the ballpark of $5K.

Balzers

The Balzers sputtering chamber is the most critical piece of equipment in the processing chain. Not only is contamination an issue for our tungsten, but the chamber is in constant public use which jeopardizes its cleanliness. After the original target was exhausted, another targer was purchased which showed no T_c. A special high purity target has now been purchased and will be kept for our use only. Modifications of the wafer holder rings were necessary to accomodate 1 cm thick wafers. This is perhaps the only piece of equipment which will not allow an increase in wafer thickness without bound (given an adaptation of the Karl Suss which allows a possible wafer thickness of several inches). The limit in thickness is created by the distance between the interior drum and the wafer pallets. It is unlikely that wafer thicknesses of more than 1.5 cm are possible. Thus, althought the phonon collection now allows us many centimeters, the practical limit in detector mass comes from our processing equipment.

Chapter 4

Experimental Apparatus

The primary concern in the design and construction of all detector hardware was that of radiopurity. The additional constraints placed on materials to perform cryogenically made the design task a very difficult one. It is a testament to this project that these systems were developed and implemented in a relatively short amount of time, and came close to achieving the stringent background goals. Aside from the actual mounting hardware of the FLIP's and the hybrid SQUID/FET card, most of the work described here was conducted by other members of the CDMS collaboration.

4.1 Detector Mount

The mounting hardware of the large 100 gram detectors was made to mirror the proven mounts used for the smaller devices as much as possible. The mount consisted of two large hexagonal copper rings (thickness 0.15 inches) with an outer diameter that would interface with the rails of the CDMS tower structure. Since the tower and BLIP hardware had already been designed, there was no option for changing the outer footprint. The hexagonal rings provide rigidity for the structure and hold the circuit boards used to interface with the detector. Two screw holes at each

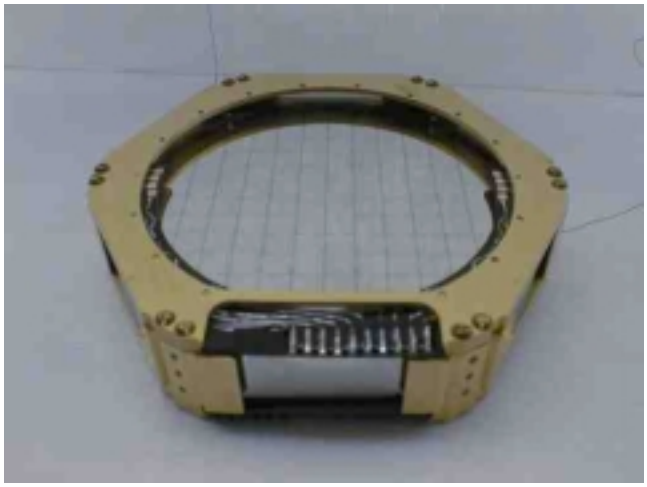

Figure 4.1: A photograph of the phonon sensor side of a mounted FLIP detector. Note the gold plated copper housing, the angled posts, Kapton copper circuit board, and the row of ten millmax sockets.

vertex of the hexagon were used to hold the copper posts that separated the charge, and phonon rings. Beryllium copper had been used successfully in the past by our group as springs to hold the smaller detectors. Uranium tends to be found with beryllium at unacceptable levels[98] so phosphor bronze was chosen as a material for springs instead. The fingers were gold plated to limit corrosion and hopefully provide good thermal contact to the W outer ring of the detector. On the phonon side, the detector was held by four of these fingers placed between the phonon ring and a support post. Extreme care was taken during mounting to ensure that the fingers only made contact with the outer tungsten electrode and not the delicate aluminum fin structure. One accidental scrape would ruin the entire detector. On the ionization side, the detector was supported by three Kapton feet. The sides of the detector were kept away from the copper posts by 0.05 inch Kapton squares epoxied into place. The phonon circuit board, the phonon 'C', had 10 millmax connectors leading to the side coax (see Fig. 4.1). Eight of these connections were for the four

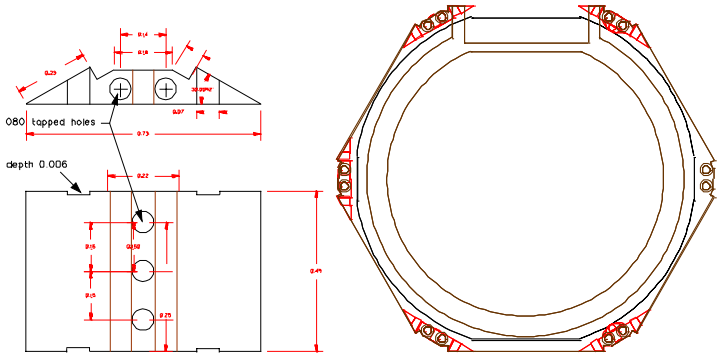

Figure 4.2: The major copper mounting parts. Two hexagonal rings (right) sandwich six copper posts (left) to create a housing for the detector.

phonon sensors and two were for the LED's required for mode I-II conversion. For the eight phonon traces, only a straight connection was required which lead to the bond pads at the east and west vertices of the hexagon. Bonds to the detector were made with 0.002 inch aluminum/silicon bond wire. The charge side circuit board had 6 millmax connectors to the side coax and contained all the components for the charge circuit. Each channel required a bias resistor (3 - 10 MΩ chip resistors) a feedback network (4 - 10 MΩ chip resistors acting as a resistor/capacitor element) and a 1 nF blocking capacitor (see diagram in sec. 2.2.1).

4.1.1 Materials

The correct choice of materials was a major concern in the design of the mounting hardware. Below is a list of all materials used in the mount, their approximate mass and whether they are considered 'counted' by the low background facilities run by Al Smith.

Item	Material	Counted	Amount
PCB (C's)	Cu/Kapton/Cu	(y)	X g
Rings	Copper	(y)	2 - 0.03"XxXx
Posts	Copper	(y)	6 - 0.03"XxXx
MillMax Pins	Phos-Bronze/Gold	(y)	16 pc
Glue	Stycast1266	(y)	3 g
Solder	CDMS Radiopure	(y)	3 g
Bond Wire	Al/Si	(m)	10 mg
1nF Capacitor	Si/SiO2/Au	(y)	2 pc
10 MΩ Resistors	Si/Mo	(y)	14 pc
LED	Plastic/Cu/Sn/Si	(y)	4 pc
LED wire	Phos-Bronze	(y)	20 cm

Table 4.1: A list of materials used for mounting a FLIP. Most materials were screened by Al Smith. The Al/Si bond wire was identical to that used by J. Emes at LBL and should be condidered counted.

4.2 Detector Tower

A significant problem for the CDMS experiment to overcome was the shear number of wires needed from 300 K to 20 mK. The eventual plan was to run seven towers each with 6 detectors. The number of wires needed from room temperature to 4 K per FLIP detector is 23 not counting ground returns. The solution to this problem was a cryogenic stripline. This was a Kapton/Copper/Kapton flex circuit 2 meters long carrying 50 traces each. For a more detailed description see the thesis of W. Stockwell[99]. The number of wires needed from 4 K to 20 mK per detector is 16. This meant that a system needed to be developed to carry 700 signals from 4 K to 20 mK with less than 1 μW heat leak. The solution is known as the 'tower' shown in figure 4.3.

Wiring from room temperature travels through the electronics stem of the Icebox to the 50 pin connector of an 4 K card (shown at the top of figure 4.3). The cryogenic preamplification system (see section 4.6) converts these 50 signals into 16 signals that

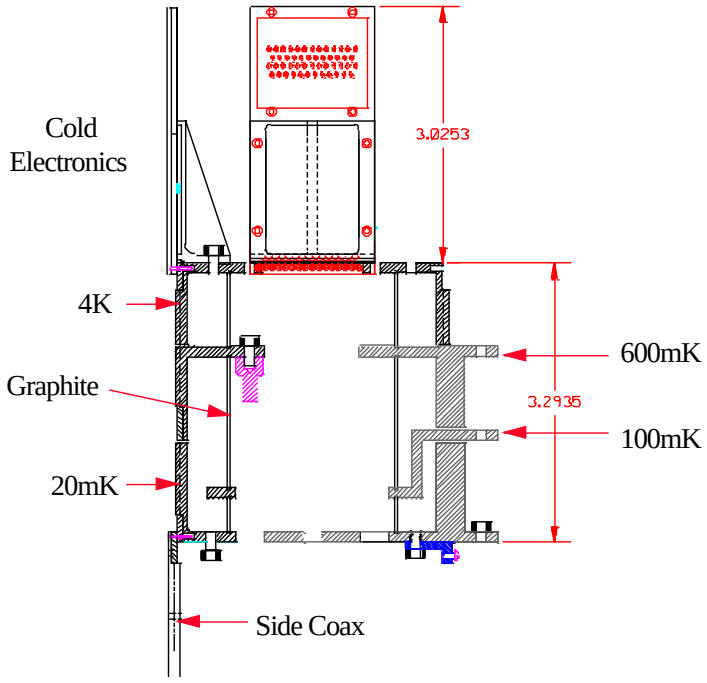

Figure 4.3: A diagram of the tower with the four temperature stages. Cold electronics cards at 4 K held the SQUIDs and FETs. Graphite tubes thermally isolated the temperature stages. Each tower carries 96 wires from 4 K to 20 mK.

need to be transmitted to the detectors at 20 mK. Connection is made between the cryogenic card and the tower using gold plated mill max pins soldered to a Kapton circuit board. The parasitic resistance of connections made with these pins has been measured to be $\sim 1\,\mathrm{m}\Omega$ at 4 K. For the phonon circuit this creates an appreciable minimum parasitic resistance of $6\,\mathrm{m}\Omega$. The 0.002 inch diameter NbTi wires then carry the signals down the side of the tower on individual vacuum coax channels. The wires are heat sunk at 600 mK and 20 mK on Kapton circuit boards. Stretched wires are a necessity for the high impedance circuits of the charge channels but are unecessary for the low impedance readout of the phonon channels. If a phonon-based discrimination scheme could be found it would greatly simplify the entire cryogenic wiring chain.

The separation between tower temperature stages is achieved using tubes of graphite machined to a thickness of 0.018 inches. The choice of graphite was a difficult one due to the enormous variability in its measured conductivity[100]. Although some forms of graphite have outstanding thermal properties (Note: the lowest conductivity is found in samples of graphite where the lattice structure has been compromised by intense neutron irradiation) the exact properties tend to be quite batch specific. Future towers are being designed with a large enough separation between stages to accomodate the radiopure graphite we have on hand. It is regrettable that due to the expense of screening new cryogenic materials, a measurement of more conventional, and highly machineable stand-off materials such as Vespel SP-1 or SP-22 were never conducted.

4.3 Berkeley: Oxford 75

The only dilution refrigerator in the collaboration (aside from the icebox, see below) that could accomodate a full size 3 inch detector was the 75 μW Oxford instruments refrigerator located on the Berkeley campus (or Berkeley Test Facility, BTF). Through the great effort of T. Shutt and others this fridge was modified (see Fig. 4.4) to mimic the internal geometry of the icebox with the four necessary temperature stages to accomodate a tower and detector package (note that the LN_2 stage from the icebox is not needed). The base temperature with a tower and detector installed was ~ 25 mK.

All of the characterization and calibration of large detectors took place in this facility (see chapter 5). This facility was also invaluable in terms of debugging electronics, tower systems, and cryogenic electronics, since the turn around time is as short as 24 hours, compared to ~ 10 days for the Icebox. The lack of a liquid nitrogen intercept means that the entire thermal burden of cooling the striplines is

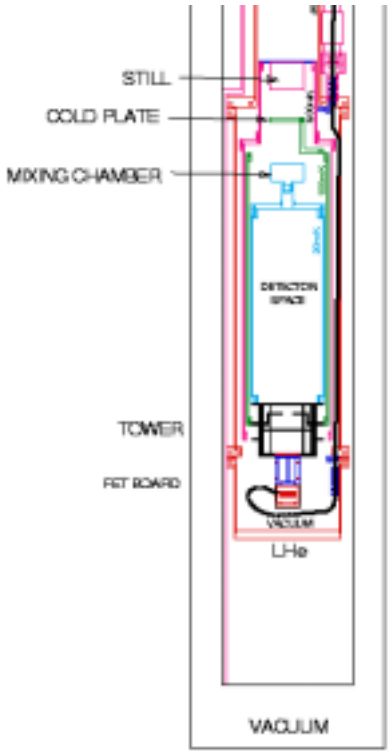

Figure 4.4: A diagram of the Berkeley 75 μW dilution refrigerator modified to accept an inverted tower assembly. The temperature stages are inverted by a series of concentric copper cans similar to the icebox.

placed on the helium bath. In order to maintain the 24 hour hold time, the number of striplines is likely to be capped at three. The limitation of this refrigerator will be apparent in the rapid testing phase of the experiment where the common systems are proven and many detectors are in the que to be commissioned. From this point of view, the Icebox will be a preferable venue due to the fact that it can simultaneously test 18 detectors.

The tower is installed upside down (when compared to the icebox, see figure 4.4) while the operator lies on their back. During installation, a plastic dust shield is placed around the refrigerator to limit the contamination due to radon daughter

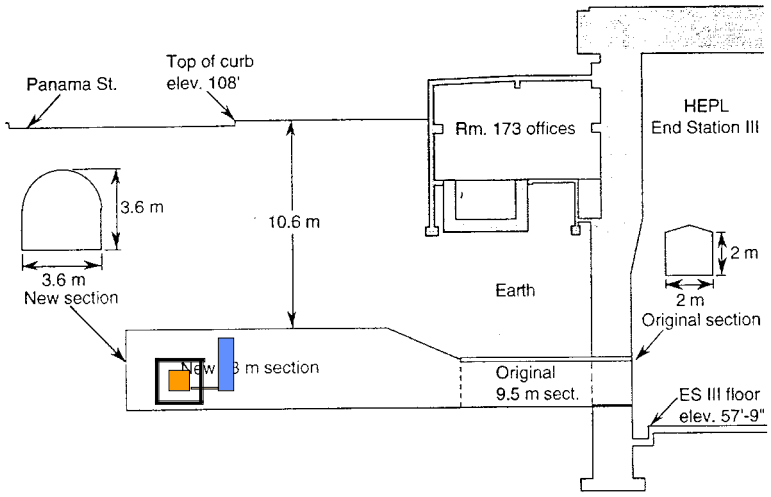

Figure 4.5: A side view of the Stanford Underground Facility (SUF). It is located conveniently on campus at a depth of 10.6 m underground. An additional 18 m of tunnel was dug out to accomodate the dilution refrigerator, icebox and associated electronics.

products that attach themselves to dust particles. Gloves, and clean tools are always employed. The seal to the IVC is a conventional indium cold weld, and the rest of the details of cooldown and running or identical to a conventional dilution refrigerator. In order to avoid excess helium exchange gas from accumulating on the surface of the detector and causing a signal deficit (see ref. [87]) we pump the IVC at $\sim$12 K for several hours. Typically, we have waited the value of $\sim 3\ 10^{-7}$ [mbar l s^{-1}] leak rate before using the circulation system to cool the rest of the way to base temperature.

4.4 Stanford Underground Facility

A large tunnel was formed out of an old accelerator beam dump at the west end of the End Station III HEPL building in 1993 to act as the shallow site of the CDMS

experiment. The background radiation of the surrounding rock was measured[101] and this information was fed back into the design of the shield (see sec. 4.4.1). For a detailed discussion of the backgounds in the shallow site and their impact of the shield design please be referred to the thesis of A. DaSilva[102]. The tunnel is 10.6 m under Panama st. on the stanford campus. The depth can be translated to 17 m of water equivalent (MWE) in terms of its attenuation of cosmic rays. The hadronic component (neutrons, protons, pions) are reduced from their sea level rates by over four orders of magnitude[101]. The muon rate, however, is reduced by only one fifth. Neutrons, induced by muons interacting in the lead shield will provide a continuous calibration and will be easily vetoed (see chapter 6).

A control room is located on the upper floors of end station III, with a fast ethernet connection to the data acquisition computer in the tunnel. Cryogens travel down a freight elevator to the mouth of the tunnel where a small hoist is used to complete the journey. Electrostatic filters are employed for the ventilation system, where clean air is pushed from the back to the mouth of the tunnel.

4.4.1 The Shield

The shielding employed around the icebox consisted of 4 major components (see Fig. 4.6):1) An active muon veto shield; 2) 15 cm of lead; 3) 20 cm of polyethylene; and 4) finally inside the copper cans 1 cm of ancient lead. The muon veto consists of many scintillator paddles completely surrounding the shield. The thresholds of each paddle is adjusted to give the maximum efficiency possible for muons while not over triggering on ambient gammas. A typical rate for the muon shield during Run 18 was about 7 kHz. Inside the active shield was a tomb of lead bricks 15 cm thick, to shield the gammas from the surrounding rock. The lead was fixed in place by a steal box structure. The lid of the lead shield was cleverly constructed to roll in and out on large rails giving convenient access to the icebox. Inside the lead was a copper

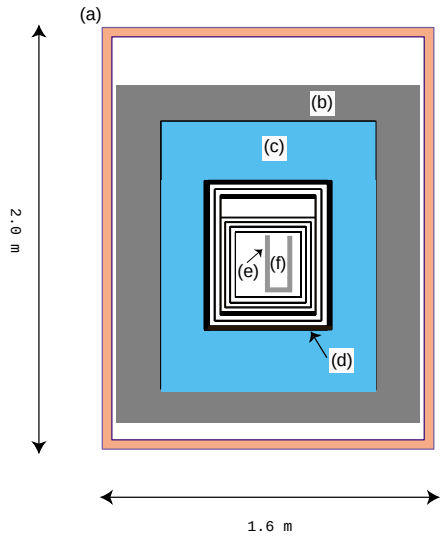

Figure 4.6: A diagram of the shielding that surrounds the icebox at SUF. From outside in: a) 4π active muon veto shield, b) 15 cm of lead, c) 20 cm of polyethylene around the d) copper layers of the icebox. Also shown is e) the 1 cm of low activity lead surrounding the d) detector array.

box which held the neutron moderator, 20 cm of block polyethylene. The ratio of lead to polyethylene depends the rejection ratio we expect from electron to nuclear recoils in the detector. It should also be noted that the neutron rate increased by an order of magnitude in the tunnel when the lead shield was introduced due to the interaction of cosmic ray muons[101]. Inside the polyethylene around the icebox outer can was a μ-metal shield to limit the impact of earths ambient field on the performance of the SQUIDs. The icebox cans themselves formed a 4 cm shield layer of copper. Inside the innermost can, immediately outside the detectors was another 1 cm of ancient lead. This lead was sufficiently old ($\sim$200 years) so that the ^{210}Pb had sufficiently died away. This was the same material that was used to produce the low activity solder[103].

4.4.2 The Icebox

The intrinsic radioactivity of many materials commonly utilized in the construction of a dilution refrigerator (such as G10, aluminum, ceramics and some plastics) required the CDMS collaboration to manufacture a specialized cryogenic compartment for use in the shallow site[104, 105]. A long right angle joint was constructed, creating a nested series 1.4 m long copper tubes between the sample space and a conventional Oxford instruments 400 dilution refrigerator (see Fig 4.7). Thermal contractions over these distances are on the order of 5 mm, making the design task very difficult. For a detailed discussion of the thermal issues, contraction, radiation, and conduction, please see ref. [99] or ref. [105].

The installation of a tower into the icebox is much easier and less risky than in the BTF. During installation, a special filtered blower is used to limit the dust contamination of the icebox. In the future, a plastic tent could be employed to prevent particulates from falling into the internal cans. The tower is inserted vertically and bolted to the base temperature lid of the icebox. At present, a small 1 cm ancient lead shield is used immediately outside the detectors to reduce muon-anticoincident the gamma rate. In the future, a circular lead shield will be employed to surround the three towers. Heatstraps and heatshields are required for the 100 mK, 600 mK and 4 K lids. The IVC seal is made with a thin, softened copper gasket and two circular copper knife edges on the can and lid. Brass bolts are used throughout. The LN_2 lid is merely a thermal shield, so requires no vacuum seal. The OVC vacuum seal is made with a standard Viton O-ring.

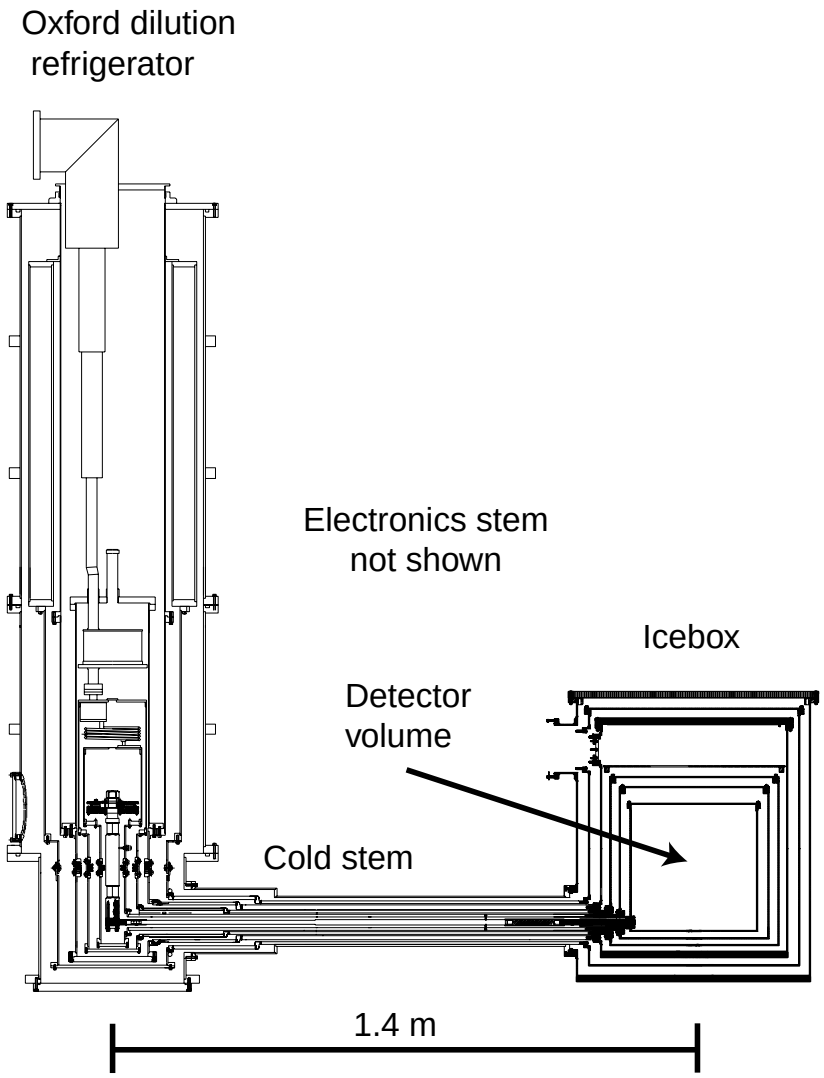

Figure 4.7: A diagram of the Kelvinox 400 dilution refrigerator, and the right-angle icebox assembly. Five concentric copper cylinders carry heat 1.4 m from a 30 l cold box (detector volume). No cryogens pass beyong the right angle joint. Wiring enters along an electronics stem through the top of the icebox. The distances between the temperature stages on the tower match with the positions of the lids.

4.5 Warm Electronics

4.5.1 Slow Control

An enormous step forward in the CDMS effort to run QET-based dark matter detectors was with the development of GPIB-controllable room temperature electronics. Ten, independantly addressable 3U boards comprised one detector compliments worth of electronics. The details of the operation and capabilities of these boards are beyond the scope of this thesis. Suffice it to say that they possessed all the features necessary to run, characterise and debug a QET-based detector. The electronic system was designed to be completely automated, through GPIB control, and yet be low noise. While communication was not taking place, the digital traffic is completely shielded from the rack.

4.5.2 Data Acquisition

Data acquisition in the tunnel was performed using a power macintosh talking to a VXI crate that housed the front end digitizers. The Labview based acquisition software was developed by D. Bauer with input from S.W. Nam. The joerger digitizers were run at 10 MHz and collected a total trace length of 1 ms. In a pre-processing phase, each of the 6 - 1 ms traces wer decimated (10:1 time averaged) and stored as a 4 kbyte record. The first 100 μs of each trace was also stored as 4 kbyte record in order to preserve rise time information. After preprocessing, data was transmitted over a local ethernet connection to a Sun Ultra 1 workstation for processing using a Matlab-based analysis program (see appendix A). Post processing and reduced quantity analysis was performed using Matlab. The enormous quantity of information meant that large data sets could not be loaded directly into memory. A clever virtual memory system was developed by S.W. Nam and R. Gaitskell to get around

this limitation.

4.6 Cryogenic Electronics

4.6.1 Description

The FLIP detector required 4 high-bandwidth SQUIDs[106] and 2 heated Silicon JFET preamplifiers to read out the phonon and ionization sensors. Requirements of the low impedence and high impedance electronics were very different, however. The Hypres SQUIDs required their temperature to be held below $\sim 6\,\mathrm{K}$ in order to operate, whereas the FETs needed to self heat above 100 K. These two design constraints are completely at odds with one another, and have continually plagued the construction of a simple cryogenic electronics package for the FLIP detectors. As I have mentioned before, the elimination of the charge channels would remove the 100 K FET ovens from the cryogenic enclosure and greatly simplify the design.

The hybrid SQUID/FET card was constructed out of two pieces of 0.05 inch thick counted copper/Kapton/copper laminate epoxied (using ecobond 1266) to a 0.03 inch OFHC copper backbone. The backbone provided enough of an isotherm in the card to prevent the 100 K FETs from warming the SQUID arrays. Holes were machined in the copper backbone around the millmax pins, the SQUIDs, and the FET window to prevent shorting, unnecessary eddy current induced flux in the SQUIDs, and thermal shorting of the FETs to 4 K. Traces on the phonon circuit were tinned using counted solder[103] to lower their parasitic resistance and prevent unnecessary heating due to the phonon bias currents.

Figure 4.8 shows both sides of the SQUID/FET card with wiring traces. The SiJFETs were attached to a 5 mil Kapton window using GE varnish. The wire FETs were connected with 2 mil diameter Manganin with a resitivity of $\sim 1\,\Omega$/inch. The

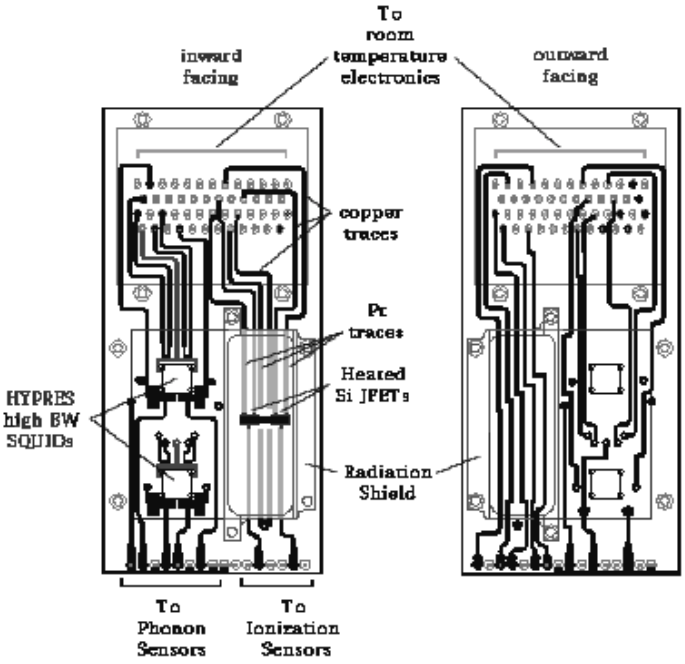

Figure 4.8: A physical diagram of the hybrid SQUID/FET card. Four high bandwidth HYPRES SQUID arrays were mounted 1 cm from two self-heated 100 K Si-JFETs. The 50 pin connector at the top mated with the stripline. The 16 pin connector at the bottom mated with the tower.

window was epoxied to the main Kapton circuit board using Ecobond 1266. A 1 kΩ RuO_2 resistor was fixed close to the FETs to facilitate self heating and to allow initial conduction after cooldown. A thermometer was never mounted, as originally intended, to monitor the bias point of the FETs.

Two HYPRES SQUID chips were attached to the card using GE7031 varnish. Each chip holds two high bandwidth SQUID arrays containing 200 SQUIDs fabricated in series. The phonon voltage bias resistors were constructed out of 20 mil diameter manganin wire cut to $\sim$0.2 inches for a resistance of $\sim$20 mΩ. The exact values of each bias resistor was measured at 4 K with a 4-terminal geometry. The

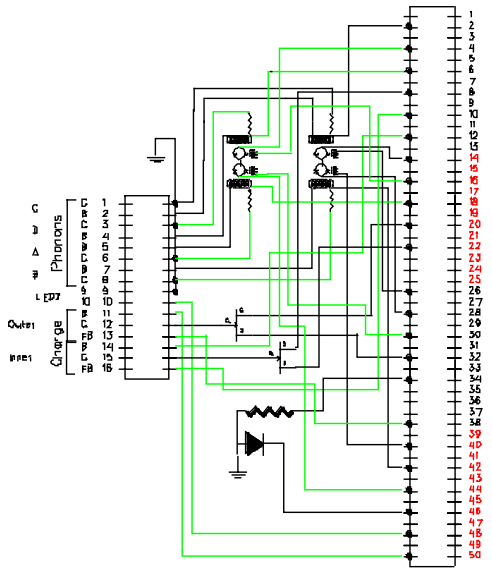

Figure 4.9: A complete wiring diagram of the hybrid SQUID/FET card shown from the stripline 4 K connector (right) to the 16 pin tower connector (left).

SQUIDs were wired to the card using 2 mil Al/Si bond wire (the same used in the detector mount).

4.6.2 Materials

As with the detector mount the choice of materials was a major concern in the design of the cryogenic hardware. More compromised were made here than in the case of the mount due to the increased distance to the detectors and the added complication of the electronic components. Below is a list of all materials used in the SQUID/FET card, their approximate mass and whether they are considered 'counted' by the low background facilies run by Al Smith.

Item	Material	Counted	Mass
PCB	Cu/Kapton/Cu	(y)	0.03"XxXx
Heatsink	Copper	(y)	0.03"XxXx
MillMax pins	Phos-Bronze/Gold	(y)	66 pc
SQUID shield	Nb foil	(n)	2 - 0.002" X 25 mm^2
Glue	Stycast1266	(y)	1 g
SQUIDs	Si/Nb	(n)	2 - 300 μm X 25 mm^2
Solder	CDMS Radiopure	(y)	10 g
SQUID glue	Ge7031 Varnish	(y)	1 g
Bond wire	Al/Si	(n)	1 mg
FET wire	Manganin	(n)	1 mg
Bias wire	Manganin	(n)	10 mg

Table 4.2: A list of materials used for constructing a hybrid SQUID/FET card. Most materials were screened by Al Smith prior to construction. The major item as yet uncounted is the Nb foil used to shield the SQUID chips.

Chapter 5

Detector Calibration

5.1 Electron Calibration

During CDMS Run 18 it was discovered that events with low charge collection that were unvetoed (ie. dark matter candidates) had significantly shorter rise times than bulk events. The hypothesis at the time was that these events were caused by electrons interacting with the surface of the detector in a 'dead layer'. Phonons created near the surface would down-convert and travel across the detector ballistically, generating faster rise times. This was an entirely new discrimination technique, and one that worked on exactly the particle that was the most problematic for the dark matter search experiment.

After the completion of Run 18, Alex was repackaged and cooled down in the Oxford Instruments dilution refrigerator at the Center for Particle Astrophysics to calibrate this phonon rise time effect.

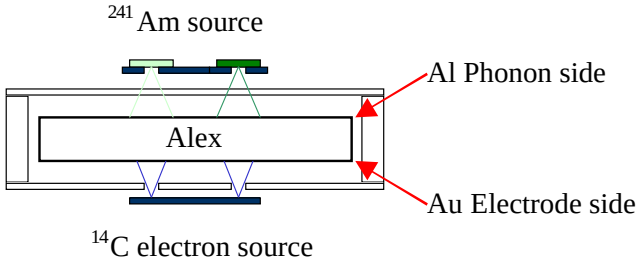

Figure 5.1: A diagram of the position of the ^{14}C (electrode side) and ^{241}Am (phonon side) sources for the electron calibration runs in the Berkeley Kelvinox 75. The ^{14}C source was visible through 4 collimation holes positioned 1 inch apart roughly centered over the X and Y axes of the detector. The ^{241}Am shone through two collimator holes lining up roughly with two of the spots from the ^{14}C source (see Fig.5.2).

5.1.1 Setup

The detector was run at the Berkeley Test Facility (BTF) without any remounting, or change to the copper housing. The goal was to create a setup that as as closely mirrored that of the previous run at SUF as possible. The same room temperature and cold electronics were used. The only item that changed unavoidably was the the primary receiver board immediately prior to the joerger digitizers. This led (we believe) to a systematic shift in rise times which we correct for when making comparisons with the low background, photon and neutron calibration (SUF data). The acquisition system was necessarily different, since the one that existed previously at BTF was optimized for a 4 channel BLIP detector. The SUF acquisition was impossible to import due to its highly complicated optimization for the various extraneous hardware such as the muon veto and temperature monitoring of the icebox. The actual working of the acquisition was made to be practically identical to the one used in Run 18. The post analysis (Dark Pipe) was completely ported to Berkeley and run with only the minor changes necessary to allow analysis of the new data

format.

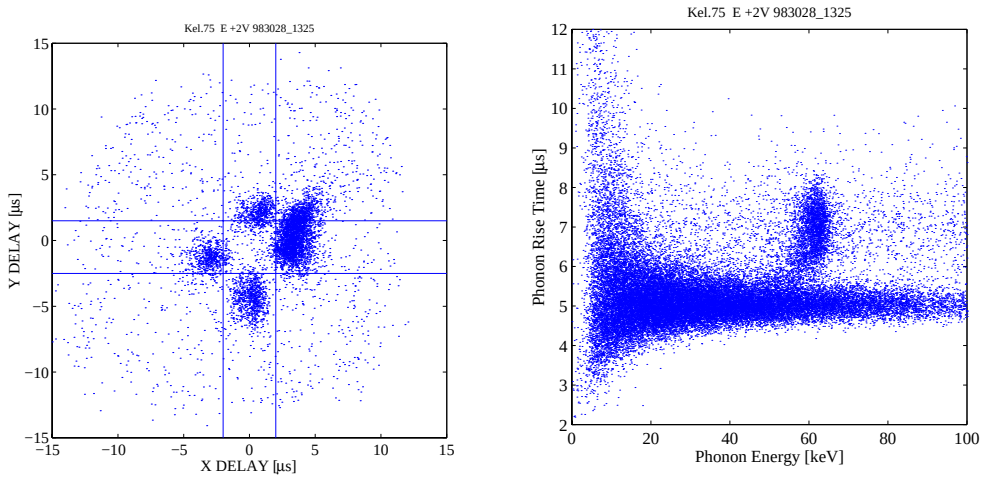

Figure 5.2: (a) Delay in X (CD-AB) versus delay in Y (BC-AD) for 60keV. The four electron spots from the ^{14}C source are clearly visible as well as those from the ^{241}Am source. Lines show cuts used for later analysis.(b) Phonon rise time versus Phonon energy. The electrons from the ^{14}C source are clearly separated from the 60keV photons of the ^{241}Am source.

To calibrate the electron response, a ^{14}C source of 1.337 μCi (total activity) was placed $\sim$1 cm from the charge side of the detector. The electrons were collimated into four spots 25 mm apart aligned with the X-Y axis of the detector itself. The estimated spot size at the surface was $\sim$3 mm, with a rate of $\sim$20Hz per hole. An ^{241}Am source was placed 1 cm from the phonon side of the detector and shone through two collimator holes. As seen in the data, the two holes lined up with two of the four ^{14}C holes (see Fig.5.2) on the x-axis.

5.1.2 Results

The evidence for a population of electrons at low phonon rise time, distinct from the population of bulk photons was clear immediately. Figure 5.2 shows the four spots from the electron source, separated by $\sim$8 μs. The ^{241}Am source is visible

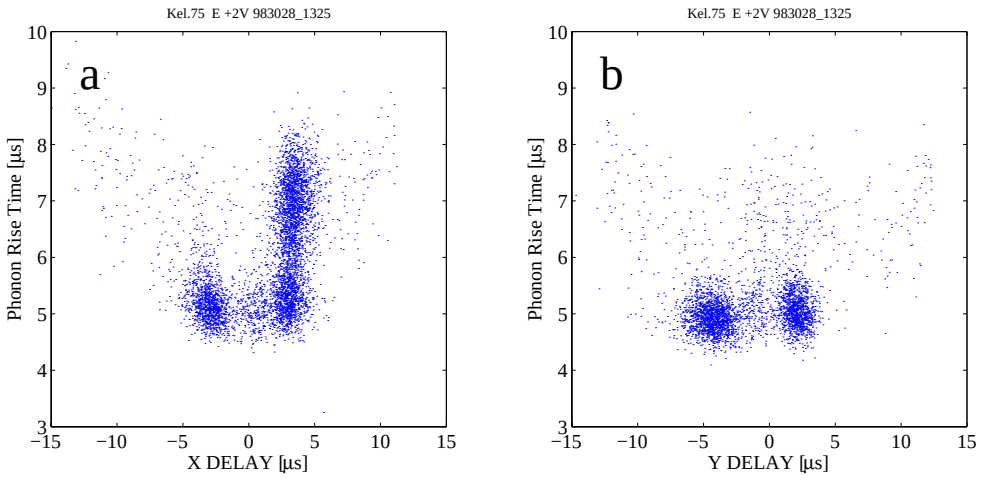

Figure 5.3: Phonon rise time versus delay in X (a) and delay in Y (b). The electrons appear at clearly lower phonon rise times ($\sim 5\mu$s) than the 60 keV photons.

by the extended smear in the rightmost distribution. By cutting alternately on the x-axis and the y-axis, we show the distribution of phonon rise times for both a pure electron population (Fig5.3b) and one including the 60 keV photons (Fig5.3a). One can see in Figure 5.3 the electron spots still clearly separated by position (x-axis of plot), and the electrons now distinct from the 60 keV photons by phonon rise time. The plot of phonon rise time versus energy (Fig.5.2) shows how the resolution of this measurement degrades with energy.

Phonon rise time was measured by filtering the pulse at 90 kHz using a 6 pole butterworth filter and simply counting up to the 80% point and down to the 20% point. Assuming the pulse is exponential in form, I then scaled the measured time by 1.59 to obtain the 10-90 rise time estimate (see appendix A).

Phonon Rise Time

There is evidence in Figure 5.2b of a tail of the 60 keV photons extending to low rise time. By carefully cutting these photons (Fig.5.4) and plotting only these events we

can estimate the distance scale of the rise time enhancement effect. The fraction of photons from the peak (obtained in this way) was $\sim 3.8\%$. Using the attenuation coefficient in silicon at 60 keV of $0.75\,cm^{-1}$, and ignoring compton photons, we can translate this to a depth of about 500 μm. Considering that an electron with 100 keV energy has a penetration depth in silicon of only $\sim 1\,\mu$m there is plenty of margin. If we consider events which have rise times approaching those of the electron population ($\sim 5\,\mu$s) we get a much smaller depth of about 50 μm. On the opposite side of the detector it clear that the photons also shift to fast rise as well as losing phonon energy (the horizontal tail in Fig.5.4a). These events are seen as the population that shifts down and to the right in figure 5.4b. Using the same method, the depth scale for these events is close to 1 mm.

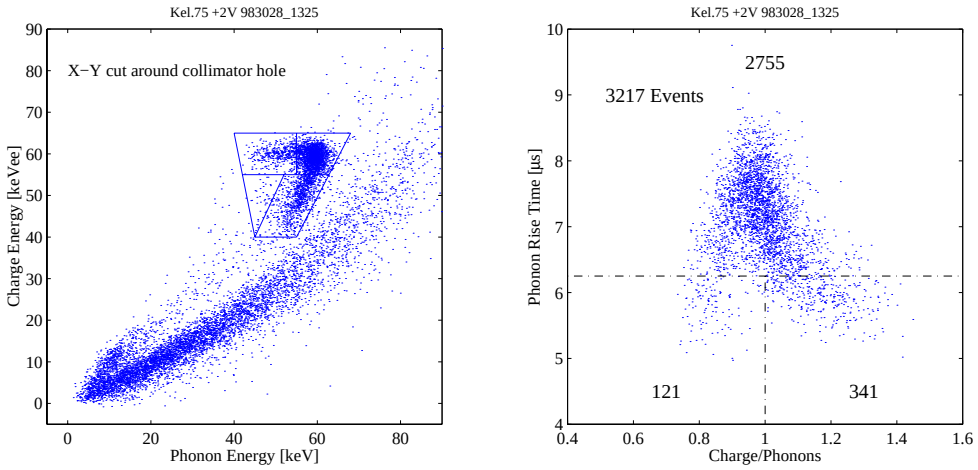

Figure 5.4: (a)Charge energy versus phonon energy. The 60keV peak has events that drop to low charge and events that move to lower phonon energy with equal charge. The cuts shown are used in (b). (b) Phonon rise time versus charge/phonons for events in the 60keV peak

From previous studies of ballistic phonon generation in semiconductors[107] it is reasonable to point to downconversion in the surface metal layer as the cause of

the enhanced rise time effect. In fact, years ago, B. Young[108] alluded to this as a possible cause of the large ballistic component in her alpha particle studies. By looking at the start time of the phonon signal with two sensors on the front and back of a 300 μm silicon wafer, she was able to estimate both the ballistic speed of sound and the ballistic phonon fraction. The area coverage and thicknesses of metal layers were quite similar to those in this detector and provide a reasonable consistency argument for a large ballistic phonon component from surface events in the presence of thin metalic layers. Let us explore a rudimentary model.

The energy density needed to raise a surface layer of gold to a temperature T is $Dtfc_vT$. Where D is the density, t is the thickness, f is the fraction of area covered, and c_v is the heat capacity of the film. If the event occurs a distance d away from the surface the energy density will look like

$$\frac{E}{4\pi}\frac{d}{(d^2+x^2)^{\frac{3}{2}}} \tag{5.1}$$

where x is the distance to each surface element. We now estimate how close a 60keV event must be to raise the surface gold layer to a temperature of 1K. At 1K, the heat capacity of gold is 5.6x10$^{-6}\frac{J}{g\,K}$[109] and the density is 19.3$\frac{g}{cm^3}$. The fractional area coverage of the gold film is 20%, and the thickness is 25nm. These parameters give an interaction distance of $\approx$100 μm quite a bit closer than the measured value of 500μm. This is assuming that the metal film warms up to an equivalent temperature of $2\Delta_{Al}$. This estimate is conservative when one considers the work of Perrin and Budd[110]. Their numeric work suggests that the distribution of phonons emitted from a metallic radiator could have a peak energy as much as three times that of the equivalent temperature black body.

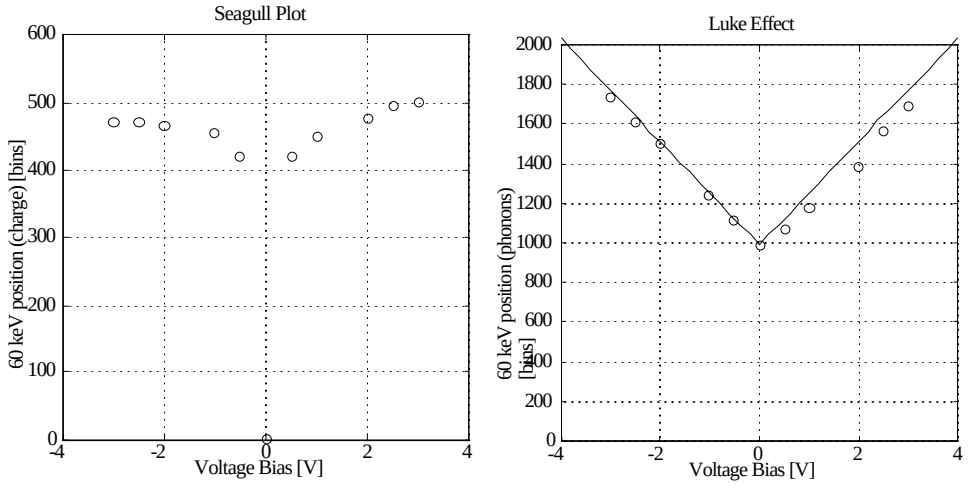

Figure 5.5: The position of the ionization and phonon peaks vs. applied voltage. The 'seagull' plot on the left shows that the ionization does not decrease until V<2. On the right, the phonon peak increases with applied voltage as one would expect if the absorption coefficient were equal for intrinsic and 'Luke' phonons. These data were taken in a previous calibration run performed without an electron source.

Voltage Dependence

By changing the ionization bias across the detector we were able to probe the nature of the phonons generated by drifting electron holes. The voltage was varied from 0 to 3 volts in the positive (with respect to the gold electrode) direction. The 60 keV peak was readily identifiable at all voltages and provided an excellent tracer for the rise time of bulk gamma interactions.

An example of the peak position variation for a previous calibration run is shown in Fig. 5.5a. The ionization peak shows the typical 'seagull' shape for a semiconductor in Mode II (see Ref. [88]). The decrease in ionization peak position means that the induced phonons from electron hole pairs are reduced from the expected yeV. This is a simple correction that has been added to the following data. The phonon peak position is shown in figure 5.5b. The phonon signal grows as one would expect

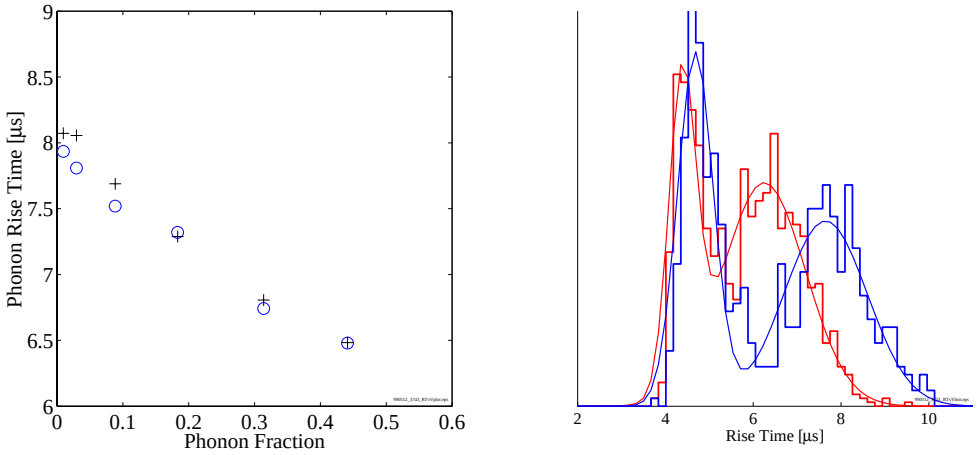

Figure 5.6: a: A plot of phonon rise time vs. the fraction of phonons created by drifting electron-hole pairs. Circles are measured values and crosses are model predictions. b: Phonon rise time distributions for 100 mV and 3 V with Gaussian fits.

if the collection efficiency were the same for intrinsic phonons as for those generated by electron-hole pairs (see solid line in figure 5.5b).

The phonon rise time of the 60 keV gamma peak was found to decrease with increasing ionization bias. While applying a bias of 100 mV, the rise time was measured at 8 μs (see Fig. 5.6a). When a bias of 3 Volts was applied, the rise time decreased to 6.5 μs. This is clear evidence that the phonons generated by electron-hole pairs are ballistic.

To explain this effect, we constructed a simple model involving two phonon species. One species would travel at the ballistic speed of sound and the other would travel 3 times slower. The factor of 3 is predicted by both Monte Carlos of phonon propagation and analytical solutions of phonon propagation in silicon[73]. The phonons then are absorbed with a 30% probability at the phonon sensor surface

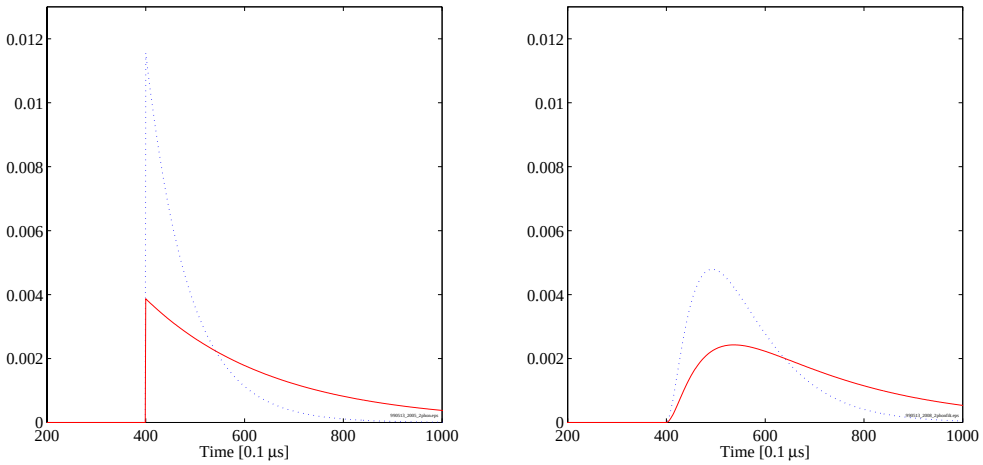

Figure 5.7: a: arrival distribution of intrinsic phonons (solid) and ballistic phonons (dotted). b: Pulses filtered by the detector response.

and are not absorbed at the charge electrode surface. This is a reasonable approximation given the 20% area coverage grid. Figure 5.7a shows the decay distribution of these two phonon populations. The detector response was modelled using single pole filters at the ETF time, τ_{etf}=10 μs, and the quasiparticle collection time, $\tau_{qp} = 2.5\,\mu$s. The relevent quasiparticle collection time has been measured to be approximately 3 μs for the test devices described in chapter 2. Although the aluminum distance was significantly shorter than the fins on the dark matter detector (350 μm versus 1.1 mm) this is still the relevent number since it represents an approximate exponential lifetime.

The integral of each pulse (shown in Fig. 5.7) is normalized and the final pulse is a mix of the two populations in the ratio given by the voltage (E_{eh}=yeV), corrected for the incomplete charge collection at that voltage (see Fig. 5.5). The combined manufactured pulses were then measured by the same analysis routine used for the actual data. Figure 5.6 shows the results of this simple two-phonon model.

5.1.3 Conclusions

This phonon detector has shown the ability to discriminate between surface events and bulk events using phonon rise time. The enhanced ballistic fraction is consistent with previous measurements by B. Young and A. Lee and resolves the discrepancy between the two systems. Surface event discrimination is a very powerful tool considering that the soft beta background is approximately the same as the gamma rate in the SUF. The enhanced phonon rise time is the first observation of its kind in detectors at such low energies[111]. The next chapter discusses the impact of this new discrimination on the WIMP-nucleon cross section. The confirmation that phonons generated by drifting electron-hole pairs are primarily ballistic suggests that a phonon filter may be constructed to discriminate between electron and nuclear recoils (see chapter 7).

5.2 Photon Calibration

The detector response to photons was calibrated using a ^{60}Co source placed inside of the lead shield. ^{60}Co decays with a half life of 5.27 years emitting 1.33 and 1.17 MeV gammas. These energies were ideal for penetrating the copper cans of the icebox and producing a uniform Compton gamma spectrum. Since absorption depth for silicon at these energies is many centimeters the probability of observing a peak was very small.

Two large photon calibration sets were taken during Run18. The first, in March, immediately prior to the low background data, and the second in June immediately after. The driving force for a large photon calibration set was the position resolution of the phonon sensor. In a detector where one is planning to perform background subtraction, it is sufficient to take as many calibration events as possible background events. Since the FLIP phonon sensor has ~ 3 mm position resolution, this effectively

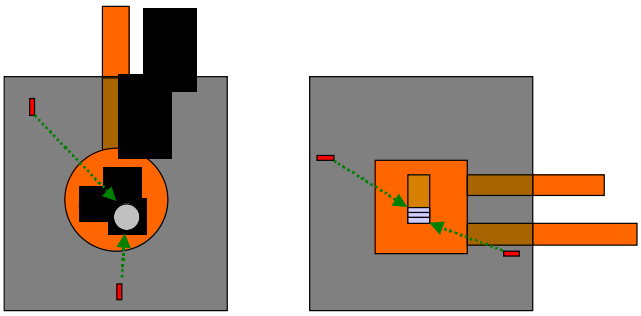

Figure 5.8: A diagram of the source positions for the two ^{60}Co gamma calibrations. In the initial run (in March) the source was placed above the detectors. In the subsequent calibration (in June) the source was lowered behind the detectors. Noise levels were much better in the June run.

means we must collect statistics on the discrimination capability for each of the 1200 independant regions in the crystal. The first calibration set consisted of nearly one million events. The second set contained only about 250,000. Figure 5.9 shows charge vs. phonon energy for the two calibration sets. One can see that the pollution into the nuclear recoil region is very small above $\sim 10\,\mathrm{keV}$.

The discovery of the two populations at low charge collection, later identified as neutrons and electrons (see preceding section) prompted us to take these two calibration sets with the ^{60}Co source in two different positions. The angular distribution of electrons would hopefully be different for the two data sets. Also, if the electrons were only visible on the electrode surface, the ratio would hopefully change depending on whether the source was above or below the detector.

Figure 5.10 is a plot of charge collection (y) versus phonon rise time for the two data sets. In march the resolution of the detector was $\sim 850\,\mathrm{eV}$ FWHM and in June the resolution had improved to $\sim 650\,\mathrm{eV}$ FWHM. This is the dominant effect in the two data sets. This greatly complicated the interpretion of any top-bottom effects.

To examine any possible systematic effect based on the position of the source, we

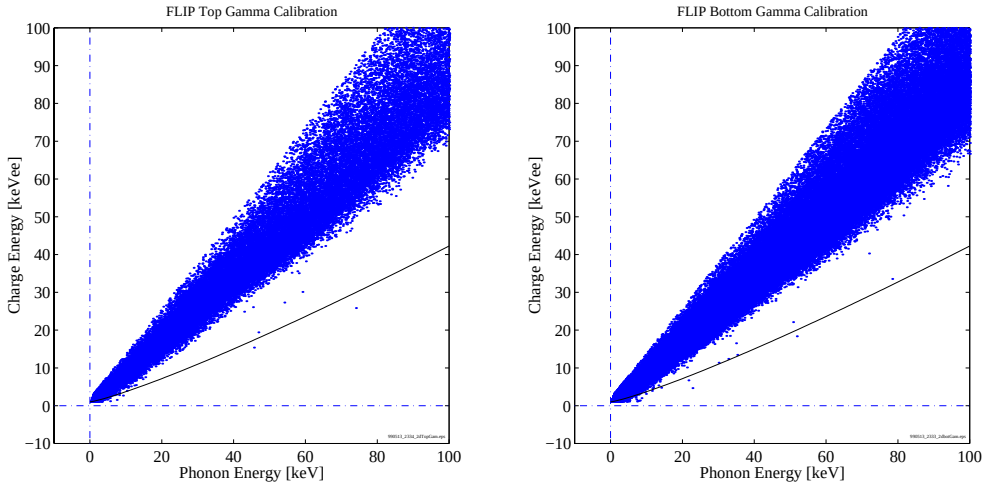

Figure 5.9: Ionization vs. phonon energy for the two ^{60}Co runs. Noise levels were much better in the later run. Fractions of electrons on both the top and bottom surface were remarkably constant.

defined two special classes of events. Bottom electrons were defined as charge/phonons less than 0.6 and rise time less than 5.5 μs. Top electrons were defined as charge/phonons greater than 1.1 and rise time less than 5.5 μs.

Particle	Top	Bottom
Total	69000	183000
Bottom beta	288	962
fraction	0.41%	0.52%
Top beta	1353	5147
fraction	1.95%	2.8%

The table above suggests that we observe no systematic effect due to the position of the ^{60}Co source. The is surprising due to the fact that the monte carlo predicts a measurable effect.

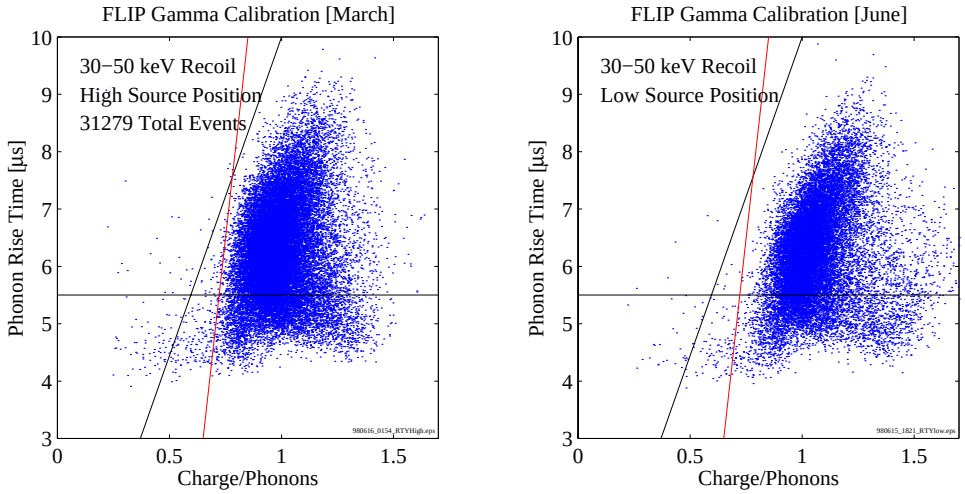

Figure 5.10: Phonon rise time vs. Charge yield for the two ^{60}Co runs. The fraction of off-axis events were consistent between the two runs suggesting no large bias in terms of the number of electron events produced on the top or bottom surface.

5.3 Neutron Calibration

The neutron calibration was performed by placing a ^{252}Cf source directly on the top of the shield assembly above the muon veto paddles. The source was the same as the one used in the BTF experiments, with an activity of **** mCi. The polyethylene above the icebox was removed, but the lead shield and the scintillation paddles remained in place.

Calibrating with a neutron source was necessary to analyze the efficiencies of all the cuts used on the low background data. Figure 5.11b shows the neutron population produced by the ^{252}Cf source at low charge/phonons. It was necessary to cut events that were in the outer ionization electrode only.

$$\left(\frac{Q_i}{P} - \frac{Q_o}{P}\right) > 0.8 - \frac{8}{E_r} \tag{5.2}$$

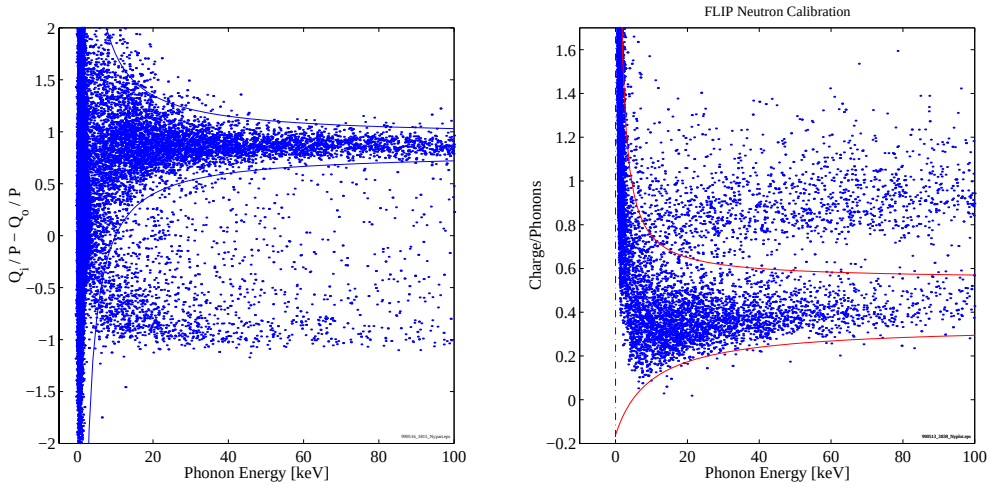

Figure 5.11: Data from the neutron calibration runs in the icebox. Lines show the bounds of the full acceptance cut to identify neutrons. All cuts are examined with respect to this data set to determine the relevant efficiency.

$$\left(\frac{Q_i}{P} - \frac{Q_o}{P}\right) < 0.95 + \frac{8}{E_r} \tag{5.3}$$

$$Q_o < \frac{Q_i}{5} + 3 \tag{5.4}$$

From the geometry of the electrode, we estimate this cut to effect 20% of the volume of the crystal. Figure 5.11a shows how this cut flares at low energies in an attempt to maintain a constant efficiency. The nuclear recoil cut attempts to be greater than 99% efficient and will be used in chapter 6 to estimate coincident and anti-coincident neutron rates. Total efficiencies, as can be found in table 6.2, are calculated directly from the residuals in the neutron calibration data.

$$Q/P > 0.34 - \frac{5}{E_r + 10} \tag{5.5}$$

$$Q/P < 0.55 + \frac{2}{E_r} \tag{5.6}$$

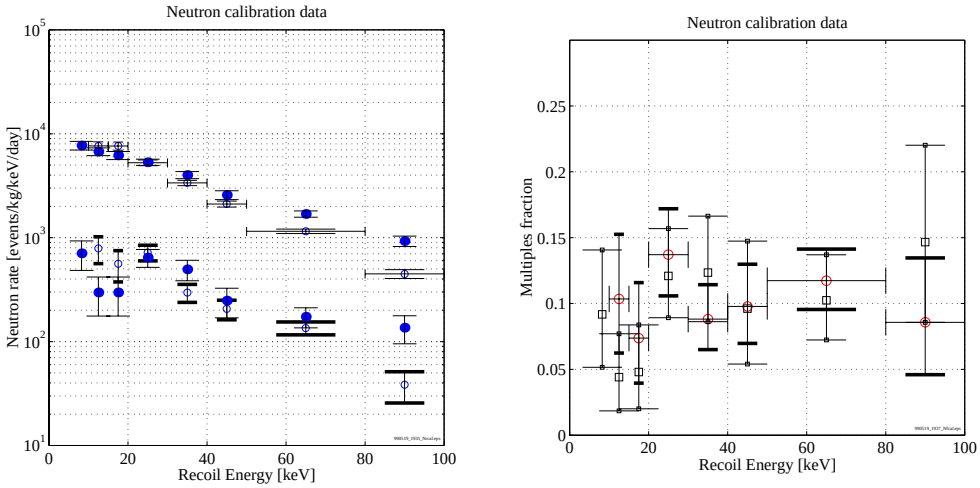

Figure 5.12: Neutron spectra in the icebox during calibration with the ^{252}Cf source. On the left are total neutron and multiples spectra (open circles) with a comparison to the Monte Carlo (solid dots), shown with 1σ errors. On the right we show the multiples to total ratio and compare to the Monte Carlo (squares). The errors shown on the right are 90% confidence limits.

The Q-outer cut and the nuclear recoil acceptance cut are the only cuts applied to the data that are not related to the discrimination parameters of charge/phonons or phonon rise time. Spectra shown in figure 5.12 are corrected for efficiency as a function of energy using the raw neutron data with only the nuclear recoil acceptance cut shown in figure 5.11b. For a summary of total efficiencies for nuclear recoils for these energy bins see table 6.2.

Comparing the neutron spectra, both in total rate and multiple scattering, to the Monte Carlo is critical at the shallow site. There is no question that we will soon be limited by the ambient neutron rate at the shallow site and will be forced to statistically subtract using multiply scattered neutrons as a probe of the total rate. See chapter 6 for a discussion and estimation of this ambient rate.

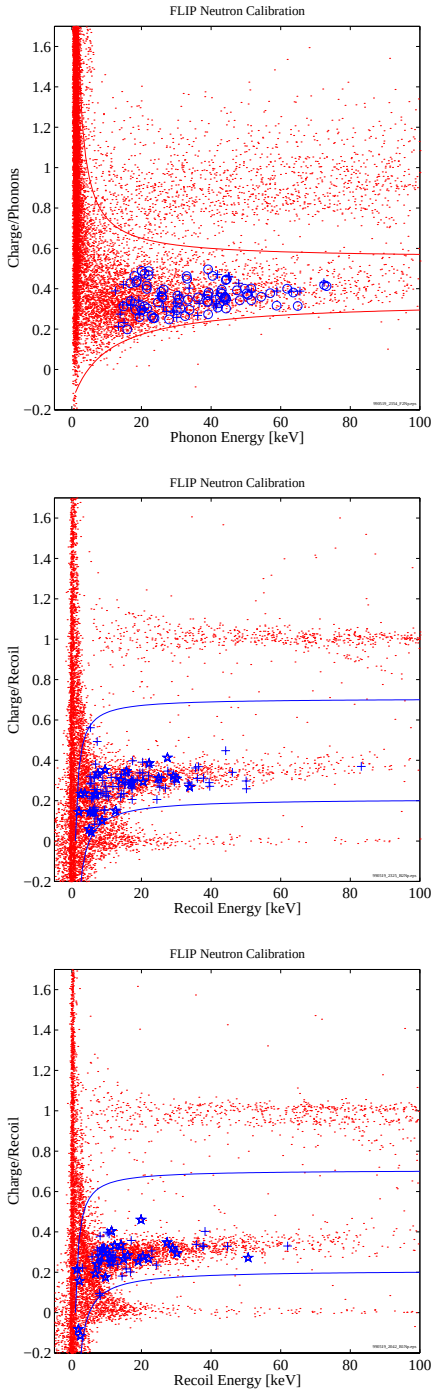

Figure 5.13: Charge/phonons vs. energy for the Alex, B2 and B1. Shown from top to bottom: the neutron calibration data for the silicon detector with B2 events (circles) and B1 events (crosses); Alex and B2 only events in B2 (crosses); Alex and B1 events in B1 (crosses). Triply scattered events (Hat tricks) are shown as stars.

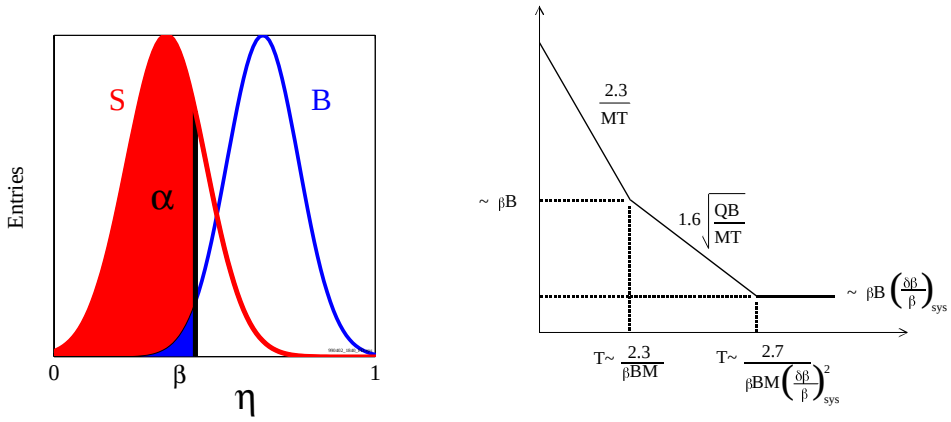

Figure 5.14: A diagram illustrating the background improvements obtained with discrimation. On the left is a cartoon showing the background distribution, B, the signal distribution, S, with α and β, the acceptance and rejection factors as a function of an arbitrary cut parameter η. On the right is a plot of the upper limit in background rate vs. time. We gain linearly in time until a background is detected, then as the square root through subtraction. Subtraction ultimately fails due to systematic uncertainties.

5.4 Discrimination

During a measurement run, we will acquire data during an exposure of some total mass-time product which we will call MT. The goal, ofcourse, is to obtain the lowest possible upper limit of our signal rate, S. To do this we attempt to model our signal and background distributions using calibration sources. We decide on a cut parameter (such as charge yield or phonon rise time), and plot the acceptance and rejection ratios as a function of this parameter. The number of events in our run to pass or fail any of our cuts can then be written

$$N_p = (\alpha S + \beta B)MT \tag{5.7}$$

$$N_f = ((1-\alpha)S + (1-\beta)B)MT \tag{5.8}$$

Where B and S are the background and signal rates, and α and β are the acceptance and rejection ratios of the cut (see Fig.5.14). Note that all discussion in this section will assume that the data has been divided into energy bins.

The first order approach is obviously to cut as much background as possible while preserving the most signal. Equation 5.7 implies

$$\alpha S < N_p \tag{5.9}$$

Making no assumptions about the ratio of background to signal events. Thus, the best cut position should be achieved when we minimize the quantity $\frac{\beta}{\alpha}$ as a function of our cut parameter η. In reality, we are after a 90% confidence upper limit in the background rate, so the quantity we minimize is

$$\frac{N_{90}(\beta \cdot N_B)}{\alpha} \tag{5.10}$$

where N_B is the number of background events actually measured of a given type. Equation 5.10 ensures that we do not continue to extend the cut unnecessarily into the signal region even though the calibration background set may still be rapidly decreasing.

Statistical Subtraction

The best limit we can hope for by the previous method is

$$S < \frac{N_{90}(\beta BMT)}{\alpha} \tag{5.11}$$

A limit that increases linearly with time after a non-zero number of events survive the cut. It might appear that the experiment was over. If, however, we return to

Eq.5.7 and Eq.5.8 and invert the expressions we see that

$$S = \frac{(1-\beta)N_p - \beta N_f}{(\alpha - \beta)MT} \tag{5.12}$$

With enough confidence that the distributions in our calibration set and our actual run are equivalent we can subtract the number of events we expect, βBMT, from N_p. The relevant quantity that will determine how close our limit can get to the true limit is now δS, with

$$\delta S^2 = \delta S^2_{stat} + \delta S^2_{sys} \tag{5.13}$$

Leaving δS^2_{sys} out of it for a moment, our statistical uncertainty in the upper limit on the background rate becomes

$$\delta S_{stat} = \sqrt{\frac{\beta(1-\beta)}{(\alpha-\beta)^2}\frac{B}{MT}} \equiv \sqrt{\frac{QB}{MT}} \tag{5.14}$$

Here we introduce the quality factor 'Q'. With statistical subtraction we now have a limit that improves with the square root of time. The strategy at this point would be then to minimize Q as a function of η.

In the situation that presents itself to us now we actually have two parameters that appear to lend themselves to statistical subtraction. I will briefly expand on the above analysis to include two types of backgrounds.

An easy extrapolation of Eq.5.7 with two quasi-independent backgrounds would be

$$N_p = \Big(\alpha S + \beta_1 B_1 + \beta_2 B_2\Big) MT \tag{5.15}$$

$$N_{f_1} = \Big((1-\beta_1)B_1 + (1-\alpha_1)S\Big) MT \tag{5.16}$$

$$N_{f_2} = \Big((1-\beta_2)B_2 + (1-\alpha_2)S\Big)MT \tag{5.17}$$

where $\alpha_1\alpha_2 \equiv \alpha$ and β_1 and β_2 are the leakages from each type of background. Equations 5.16 and 5.17 simply state that a loss in S must show up in one of the other distributions. This is an approximation.

Inverting this matrix is significantly harder, however following the same line of analysis as above we find that

$$\delta S_{stat} = \sqrt{\frac{(1-\beta_2)^2\beta_1(1-\beta_1)B_1 + (1-\beta_1)^2\beta_2(1-\beta_2)B_2}{\alpha_1\alpha_2(1-\beta_1\beta_2+)\beta_1\beta_2 - \beta_1\beta_2(\alpha_1+\alpha_2-2) - \beta_1\beta_2}\frac{1}{MT}} \tag{5.18}$$

Which, to first order, reduces to something like what we expect

$$\delta S_{stat} = \sqrt{\frac{Q_1B_1 + Q_2B_2}{MT}} \tag{5.19}$$

which tells us that we will be (linearly) dominated by the background with the largest Rate-Q product.

5.4.1 Discrimination Data

In order to align the photon, electron, and neutron distributions of the SUF data and BTF data several shifts were necessary. A shift in the charge/phonon distribution at SUF of

$$Y = (Y - .4) * 1.25 + 0.4 \tag{5.20}$$

was necessary match the photon and neutron distributions. This can be explained by perhaps slightly different neutralization conditions for the two runs. A shift in the rise time distribution at BTF of -0.4 was necessary to align the electron tail of

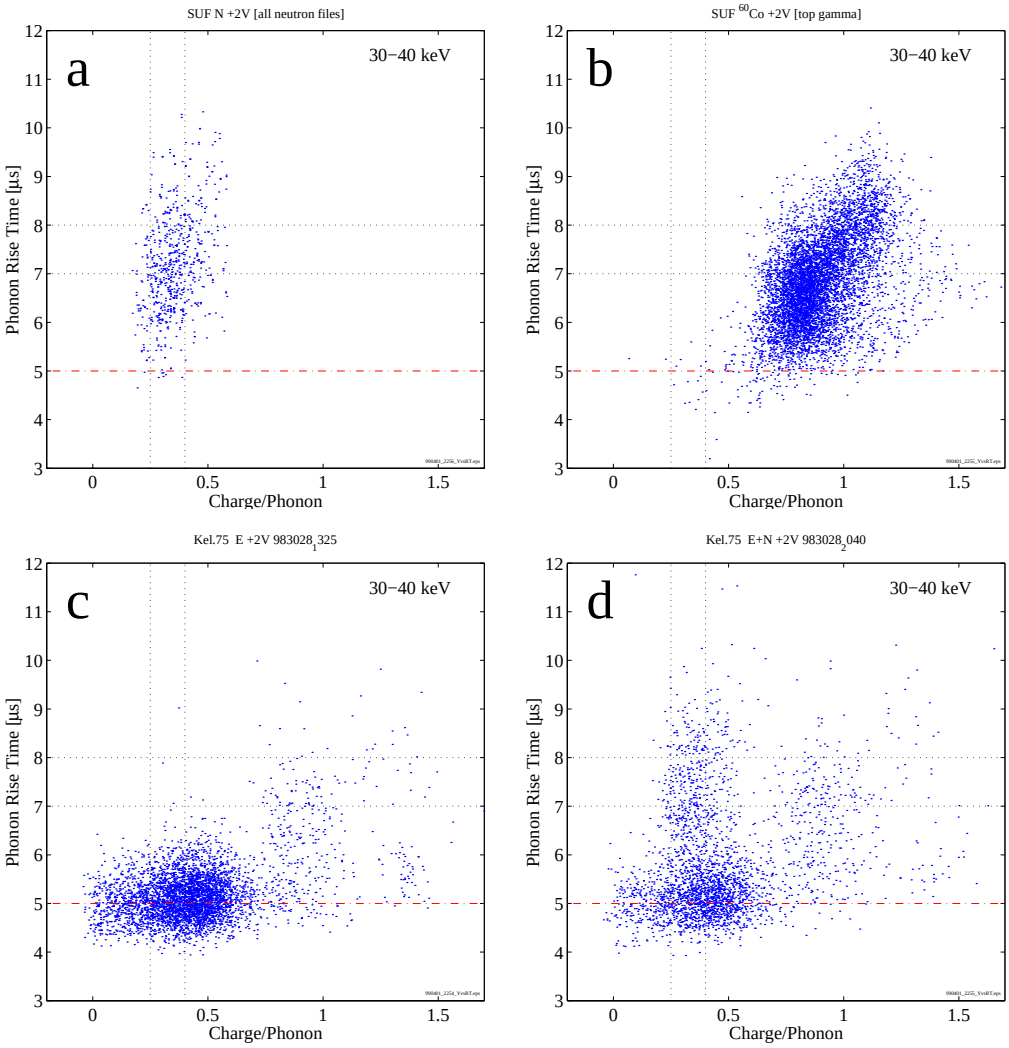

Figure 5.15: A plot of phonon rise time versus charge/phonons for four different calibration runs: a) Neutron calibration run in SUF with a ^{252}Cf source (gammas have been removed); b) Photon calibration in SUF with a ^{60}Co source; c) Electron calibration in BTF with a ^{14}C and an ^{241}Am source; d) same as c) with an external ^{252}C source. All data are 30-40 keV recoil energy. Dotted lines represent cut regions over which the optimal η_y and η_{rt} were calculated.

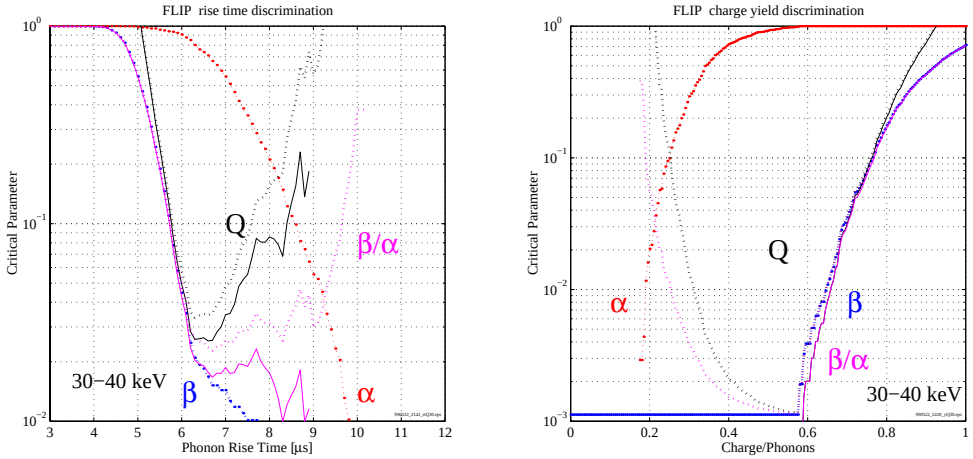

Figure 5.16: a)Phonon discrimination in the 30-40 keV range. Shown are α_r and β_r vs. rise time with the quality factor, Q_r, and β_r/α_r. Note that β_r/α_r is less sensitive to the cut position, η_r, than Q_r . b) Charge yield discrimination in the 30-40 keV range. Note that charge-based discrimination is an order of magnitude better than that of rise time at the same energy.

the photon calibration at SUF with the electron calibration at BTF. Figure 5.16 shows the variation of α, β and the quality factor, Q for both rise time and charge yield. [t] Note that the charge yield discrimination is over an order of magnitude better than the rise time discrimination at all energies. Table 5.1 lists the rejection factors calculated for a range of energy bins.

5.5 Conclusions

This 100 g silicon detector has clearly demonstrated the ability to discriminate between a soft surface beta background and nuclear recoils. The rise time enhancement seems due to phonon down-conversion in metallic layers on the surface, although

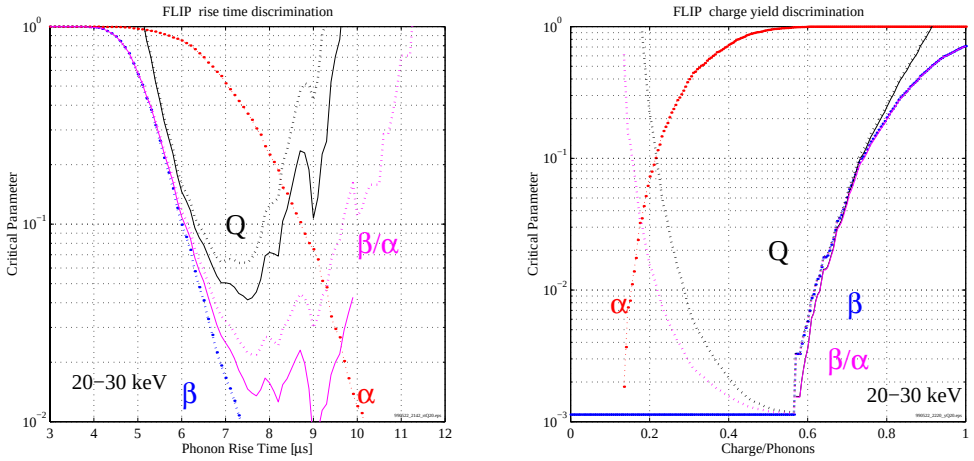

Figure 5.17: a)Phonon discrimination in the 20-30 keV range. b) Charge yield discrimination in the 20-30 keV range. Note that charge-based discrimination is an order of magnitude better than that of rise time at the same energy.

Recoil Energy	15-20	20-30	30-40	40-50	50-80	80-100	15-100
N_γ	933	1973	1990	2024	5756	3592	16268
η_y	0.465	0.5	0.5	0.5	0.5	0.5	
β_y	0.0	0.0	0.0	0.0	0.0	0.0	
$\delta\beta_y$	0.0	0.0	0.0	0.0	0.0	0.0	
$\beta_{y-90\%}$	0.002	0.0011	0.0011	0.0011	0.0011	0.0011	
N_β	839	1698	1348	961	1380	309	6535
η_{rt}	7.8	7.4	6.5	6.2	6.2	6.2	
β_{rt}	0.017	0.007	0.014	0.023	0.025	0.049	
$\delta\beta_{rt}$	0.004	0.002	0.003	0.005	0.004	0.012	
$\beta_{rt-90\%}$	0.023	0.0094	0.018	0.029	0.030	0.064	

Table 5.1: A summary of rejection factors from the calibration data. Shown are the best estimate of β for the charge yield and rise time rejection factors with the binomial errors and the 90% confidence upper limit.

more modelling is necessary to confirm the exact distance scale and phonon spectrum. The ability of this detector to resolve phonon arrival times on the order of a few microseconds has allowed a confirmation that phonons generated by drifting electron hole pairs are lower frequency and ballistic. Future work by the author will hopefully take advantage of this effect in the development of new detector technology.

Chapter 6

Low Background Data

6.0.1 Introduction

The background run discussed in this chapter is known as Run 18. Runs numbered 1 through 11 took place in Berkeley during the testing phase of the icebox/fridge assembly. Run 12 was the first test of the apparatus in SUF, and Run 13 was the first operational cool down with a 10 g NTD detector known as E5. This run yielded results that were suggestive of a large electron background, in the case of the slow NTD detectors, easily mistaken for a large neutron background. Run 14 consisted of E5 and the first 100 g silicon FLIP detector known as Mr. Smooth. The name is attributable to P. Brink, due to its surface morphology (Mr. Bumpy, fabricated on the wrong side, was its processing pair). The first silicon FLIP had a rather large threshold ($\sim$30-60 keV) but still managed to display important features of position sensitivity and high electron/nuclear recoil rejection efficiency. Run 15 employed the first 160 g BLIP detector in the place of E5, with similar limits to those of Run 14. The silicon detector was never activated during this run despite occupying space in the icebox. Run 16 was a BLIP only run with two 160 g Ge detectors with a large irreducible beta background. Run 17 was conducted largely by R. Gaitskell in

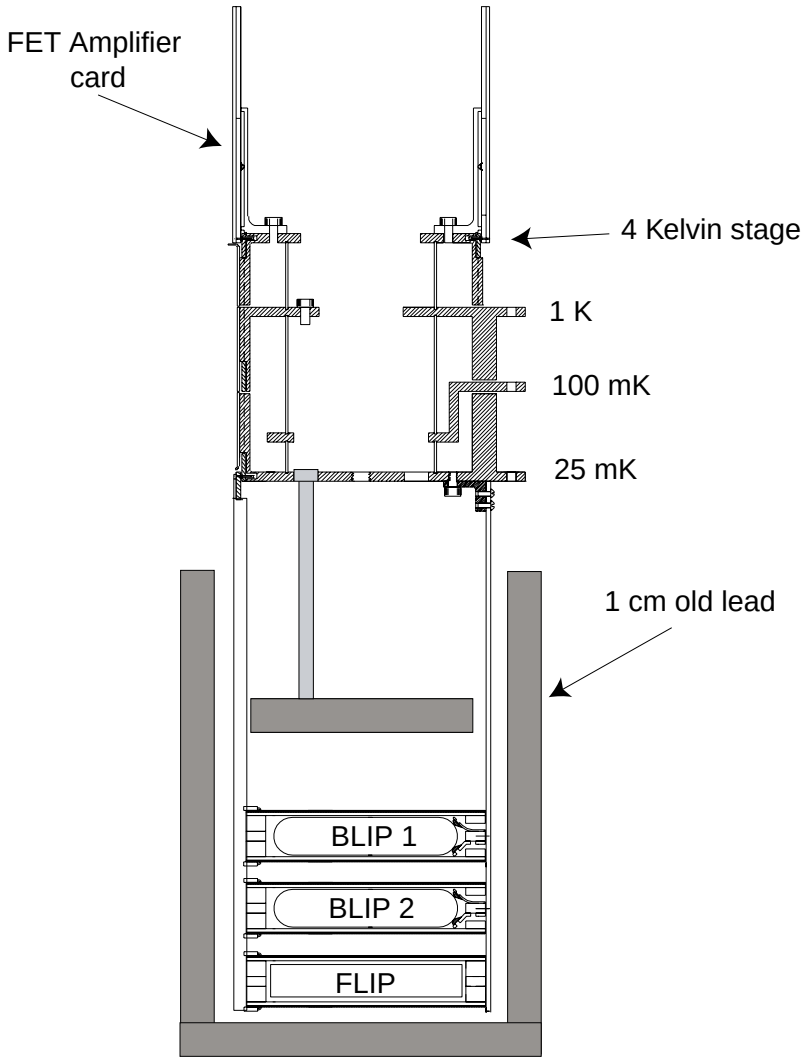

Figure 6.1: A diagram of the Run 18 geometry. Alex was placed at the bottom of a stack of three detectors. A 1 cm shield was placed close to the detectors in an effort to lower the photon background rate. The spacing between FLIP and BLIP 2 was approximately 2 cm.

an effort to determine whether the tritium signal in the BLIP detectors could be attributable to spallation production in the NTD's during neutron bombardment. The results were convincingly positive.

Run 18 began late in 1997, around November. During the initial cooldown the mixing chamber of the Oxford 400 began leaking. Due to the complexity of the icebox arrangement this represented a total disaster for the experiment. The dilution refrigerator was separated from the tail section (see figure 4.7) by a crane structure (constructed by M. Hennessey) and the outer dewar and heat shields were removed. The leak was eventually found by P. Colling and J. Jochem by carefully raising and lowering a bucket of water over the mixing chamber and dilution unit. A bad join around the outside of the heat exchangers was the cause of the leak. The initial cooldown of the icebox finally began on Elvis' birthday, 1998. Table 6.1 summarizes the major events and milestones of Run 18.

Date		Milestone
Jan. 8	->	Cooldown starts
Jan. 27	->	Initial calibration data
Jan. 28	->	Hardware debugging, Neutralization
Feb. 14	->	Stable running, Muon veto debugging
Feb. 25	->	Period of improved veto efficiency ($\sim$99 %)
Mar. 5	->	Phonon rise time RQ added
Mar. 19	->	Period of low FLIP threshold, BLIP μ-phonic susceptibility
Mar. 24	->	Million event ^{60}Co calibration
Apr. 3	->	^{252}Cf Neutron calibration
Apr. 8	->	33 live days of good data, new veto readout implemented
June 12	->	^{60}Co calibration in low source configuration
July 3		End of Run 18

Table 6.1: A summary of major events in Run 18. The rise time discrimination of the silicon detector was instrumental in distingiushing between a non-isotropic muon veto shield and an electron background.

6.1 Muon Veto

The story of Run 18 and how it relates to the understanding of the backgrounds at SUF was really the interplay between the ability of the silicon to detect neutrons and a growing confidence in the efficiency of the muon veto. It should be stated that prior to this run, there existed to reliable measurement of the veto efficiency for neutrons at SUF. The BLIP detectors of the time could barely estimate the coincident neutron rate due to extreme confusion between neutrons and electrons. When the run began (see table 6.1), the muon veto had degraded to a serious extent. The efficiency for muons traversing one of the dark matter detectors, the only direct measurement technique, was $\sim 90\%$. This was the result of drift in the thresholds of the photomultiplier tubes, and some damaged connections between the light guides. Due to intense effort on the part of A. Sonnenschein, the veto subsequently outperformed all estimations of its capability. Direct measurements from through-going muons indicated an efficiency of 99.995%! The efficiency for the creation of neutrons in the lead of the shield is very difficult to measure, however. Initial results from the silicon detector, showed an incredibly poor efficiency for nuclear recoils, $\sim 75\%$. The unvetoed events, however, were all at low phonon rise time. The rise time cut of the FLIP allowed a lower limit on the efficiency for neutrons created in the shield of about 99%.

6.2 Background Rates

6.2.1 Photons and Electrons

Measuring the rate of photons and electrons at SUF is critical. From the raw rate, we may be able to estimate how well a given detector will do with a measured rejection ratio. From the ratio of anti-coincident to coincident photons we may test

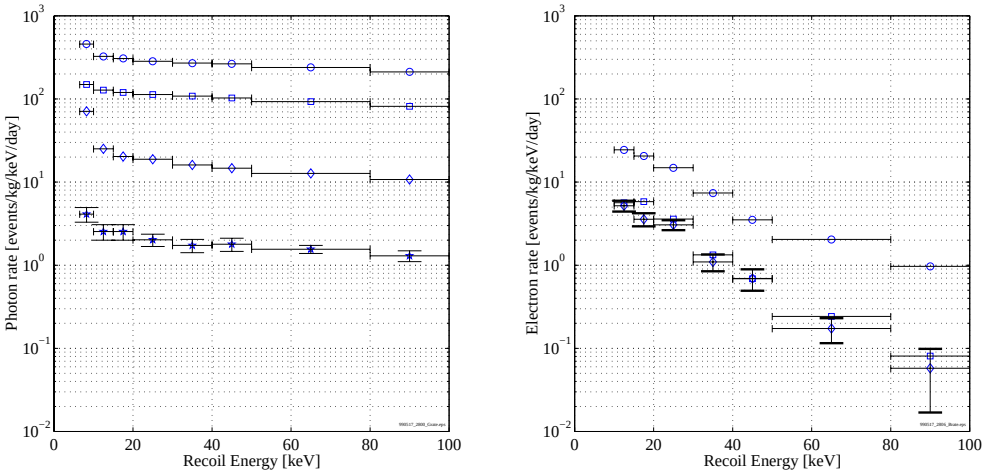

Figure 6.2: a: The photon rate for Alex at SUF. In order of decreasing rate are the coincident photons (circles), multiple coincident photons (squares), anti-coincident photons (diamonds), and anti-coincident multiply scattered photons. b: The electron background at SUF. Shown are the coincident electrons (circles), the multiply scattered coincident electrons (squares), and the anti-coincident electrons (diamonds). Anti-coincident multiply scattered electrons are not found.

the Monte Carlos of muon photon production in the shield. A photon, for the purpose of calculating rates, is defined as Q-inner, no rise time cut, and the Q/P ratio larger than the cut value for nuclear recoils. This is sufficient since the pollution from electrons and neutrons into the gamma band is usually negligible in terms of relative numbers. An electron is defined as that which would have passed all the acceptance cuts as a nuclear recoil except that it fails the rise time cut.

6.2.2 Neutrons

The success of CDMSI at the shallow site rests critically on the irreducible neutron background. Neutrons created by muons passing through the rock outside are shield are impossible to veto. These neutrons are created at high energies, $\sim$GeV, and

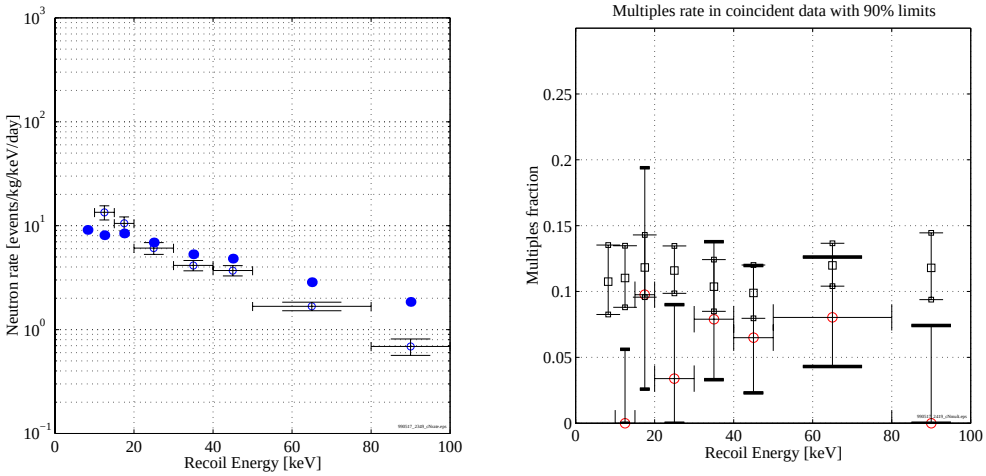

Figure 6.3: a: The rate of coincident neutrons at SUF measured by the 100 g silicon detector with 1σ error bars. Monte Carlo results are shown as dots. b: The fraction of neutrons that multiply scatter in the Run 18 geometry with data (circles) and MC (squares). Error bars are 90% confidence limits. The definition of a multiple event can be found in the text.

have a finite probability of penetrating the polyethylene of the shield. The most likely place for this to happen would be through the F or E stems. The cryogenic requirements of these stems prevent the placement of large amounts of moderator along their length. When the experiment begins to measure this background, and there is some evidence that the silicon FLIP detector has encountered it, the only recourse is to begin to statistically subtract based on the singles to multiples ratio. This ratio is predicted by Monte Carlo, however, and must be verified by the relatively abundant population of coincident neutrons.

Recoil Energy	15-20	20-30	30-40	40-50	50-80	80-100	15-100
Total N	41	59	76	77	112	31	396
Single N	37	57	70	72	103	31	370
Multiple N	4	2	6	5	9	0	26
B2 only	1	2	3	3	7	0	16
B1 only	1	0	3	2	1	0	7
Hat trick	2	0	0	0	1	0	3
Efficiency	0.24	0.29	0.55	0.63	0.68	0.68	
Anti-coincident	0	1	0	3	0	0	4
Monte Carlo							
Total N	32.9	66.8	97.0	100	191	83.2	571
Single N	29.0	59.1	87.0	90.4	168	73.4	507
Multiple N	3.9	7.7	10.0	9.9	22.9	9.8	64
B2 (20%)	2.8	4.5	7.6	6.5	15.5	6.1	43.0
B1 (30%)	0.9	2.5	2.5	3.2	5.3	3.3	17.7
Hat trick	0.2	0.7	0	0.2	2.1	0.5	3.6

Table 6.2: A compilation of neutron data for the 100 g silicon detector at SUF. These data were used to create figure 6.3. Note that the raw number of neutrons differs from the Monte Carlo by 30% in addition to having a steeper slope (see figure 6.3).

6.3 Limits

The final 4 muon anti-coincident nuclear recoil candidates6.2 were used to calculate a preliminary limit on the WIMP-nucleon cross section for Alex in Run 18. In order to determine a 90% confidence upper limit for a WIMP of a given mass we ask the question 'what WIMP-nucleon cross section would yield a larger number of events in a selected energy bin 10% of the time. In this regime of sparse data one must take great care not to arbitrarily choose energy bins, to avoid biasing the data. To overcome this problem, a special method was developed by S. Yellin which allows the data to select energy bins by itself. Since the best limit will always be obtained by taking the largest energy bin, with the fewest relative events, one by pick bins which

Recoil Energy	15-20	20-30	30-40	40-50	50-80	80-100	15-100
N_β	31	53	19	12	9	2	126
$N_\beta\beta_{rt}$	0.52	0.34	0.27	0.27	0.22	0.10	1.7
$\delta(N_\beta\beta_{rt})$	0.14	0.10	0.06	0.06	0.04	0.02	0.4
N_γ	154	291	249	224	581	327	1826
$N_\gamma\beta_y$	0	0	0	0	0	0	0
Total Expected	0.52	0.34	0.27	0.27	0.22	0.10	1.7

Table 6.3: An estimate of the expected residual signal rate in SUF. Electrons are defined as events which pass every other signal cut except phonon rise time. Gamma events are merely defined as events with large charge/phonons. Note that of the 4 anti-coincident neutrons found in 33 live days we expect 1.7 from the known background distributions.

lie in between the events themselves. As long as one pays the statistical penalty for searching among all the gaps between all the events (in our case 4) one will achieve the best limit. It is the implimentation of this 'maximal gap' method (coded by R. schnee) that was used to calculate the limit for Alex in Run 18 with a total exposure of 33 days.

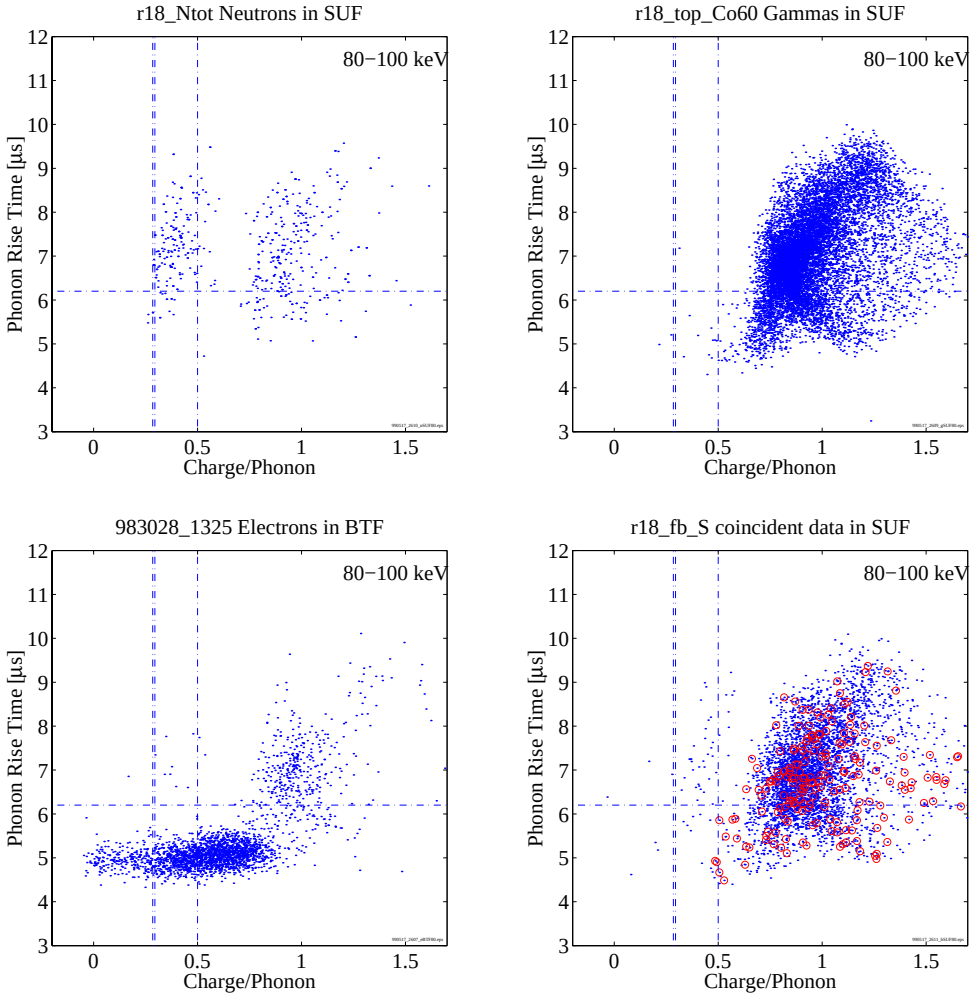

Figure 6.4: 4 sets of phonon rise time vs. Q/P 80-100 keV. The optimal phonon rise time position is 6.2 μs, the optimal Q/P value is 0.5. $\beta_r = 0.0640$ and $\beta_y = 0.001$. The total efficiency for this energy range is 48%.

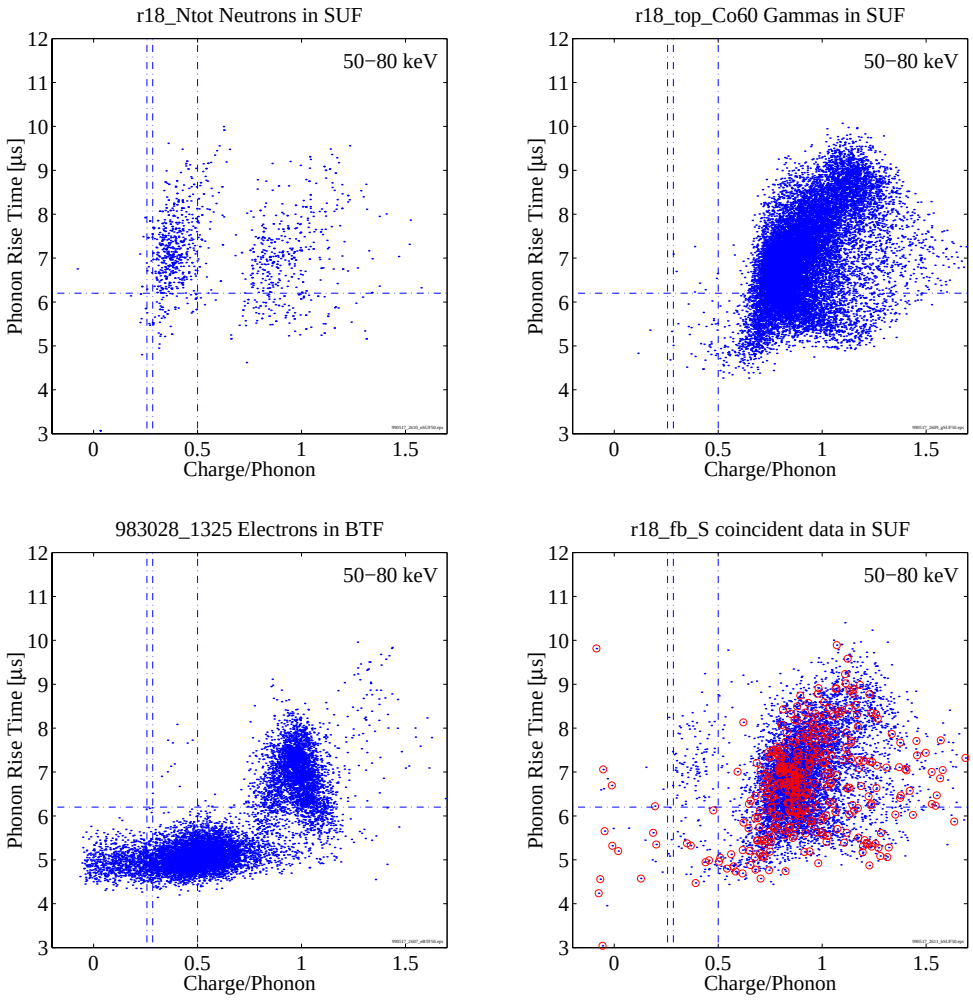

Figure 6.5: 4 sets of phonon rise time vs. Q/P 50-80 keV. The optimal phonon rise time position is 6.2 μs, the optimal Q/P value is 0.5. $\beta_r = 0.03$ and $\beta_y = 0.001$. The total efficiency for this energy range is 47%.

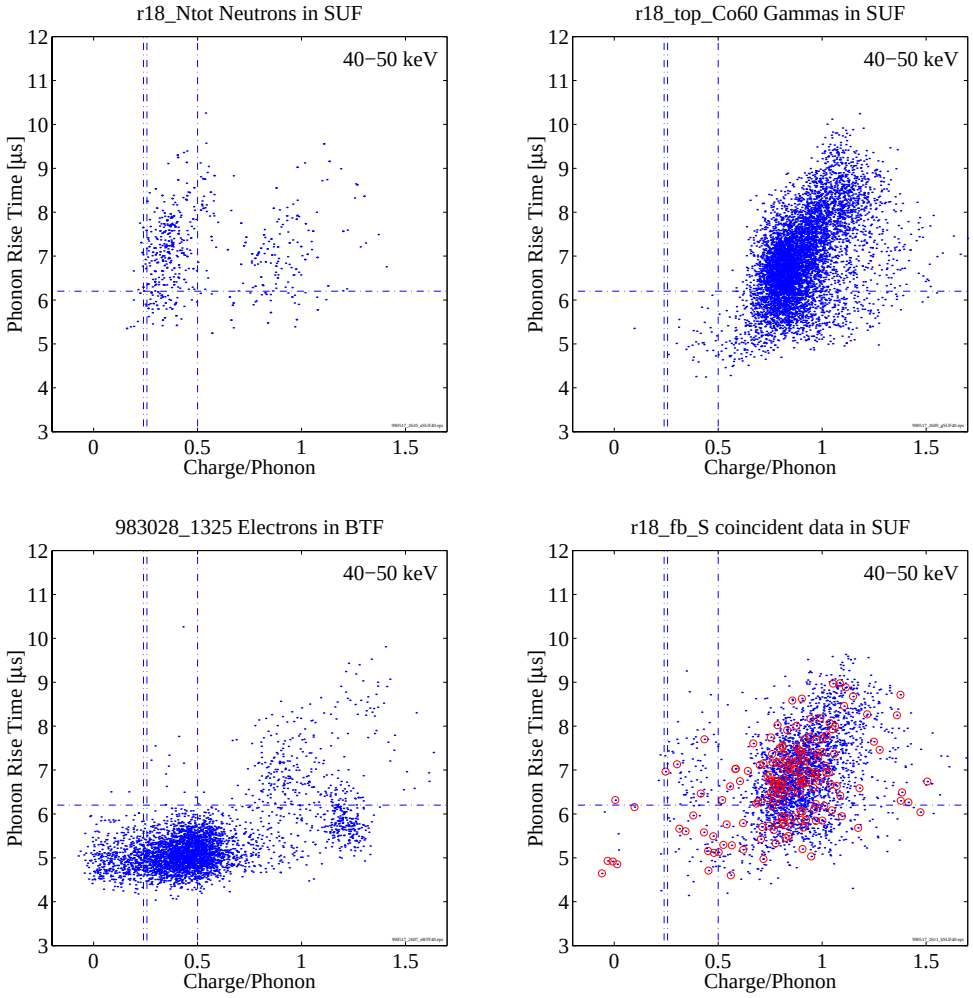

Figure 6.6: 4 sets of phonon rise time vs. Q/P 40-50 keV. The optimal phonon rise time position is 6.2 μs, the optimal Q/P value is 0.5. $\beta_r = 0.03$ and $\beta_y = 0.001$. The total efficiency for this energy range is 44%.

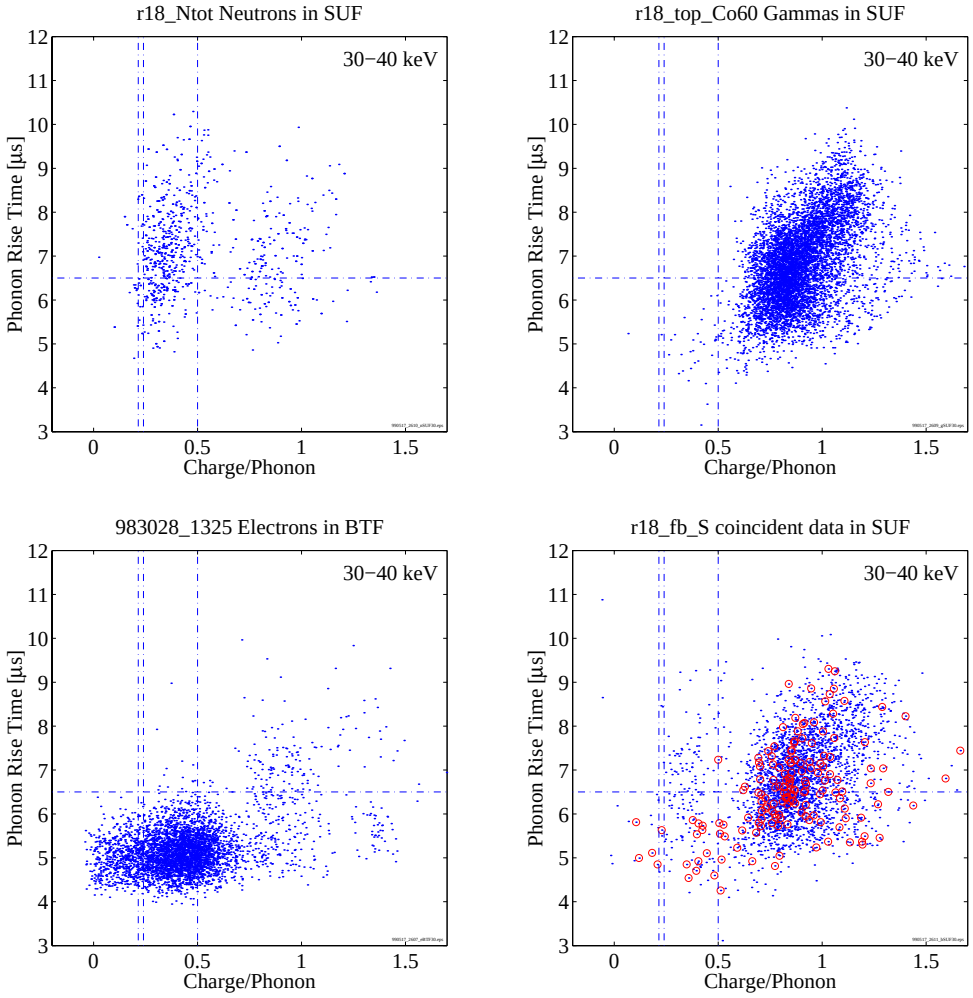

Figure 6.7: 4 sets of phonon rise time vs. Q/P 30-40 keV. The optimal phonon rise time position is 6.5 μs, the optimal Q/P value is 0.5. $\beta_r = 0.02$ and $\beta_y = 0.001$. The total efficiency for this energy range is 39%.

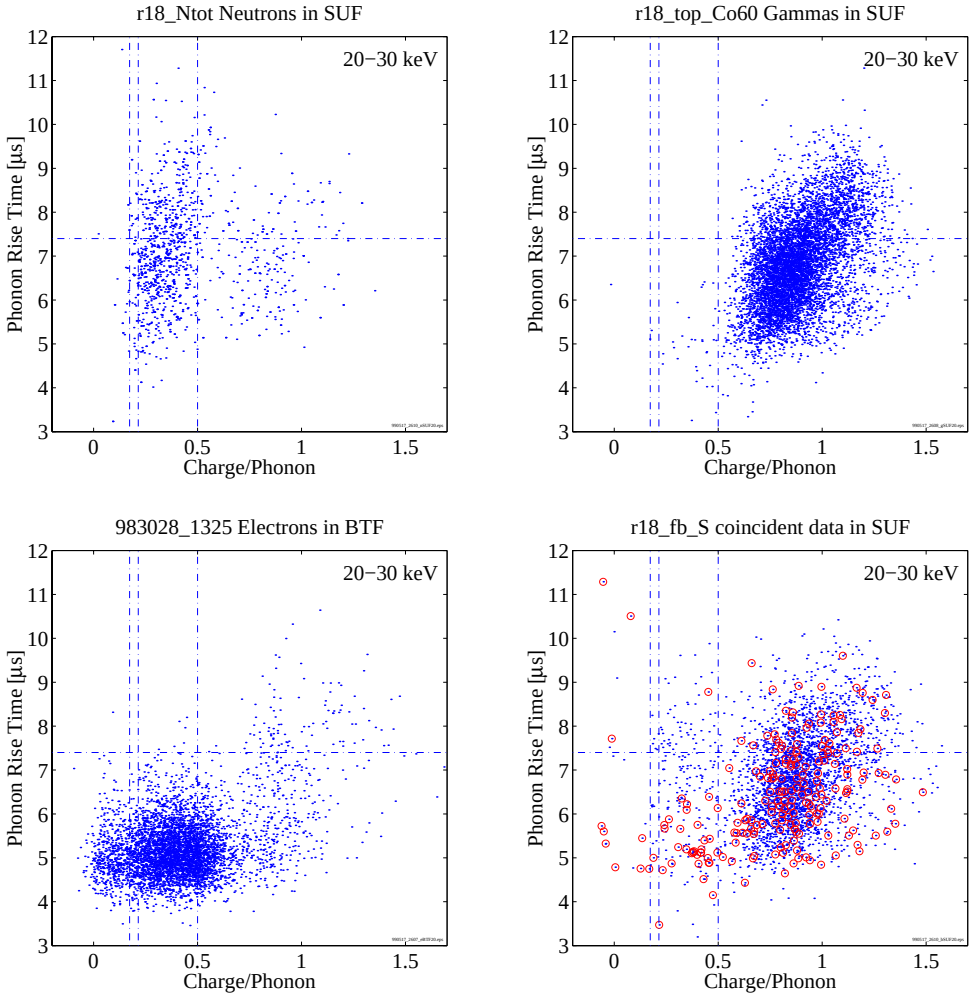

Figure 6.8: 4 sets of phonon rise time vs. Q/P 20-30 keV. The optimal phonon rise time position is 7.4 μs, the optimal Q/P value is 0.5. $\beta_r = 0.01$ and $\beta_y = 0.001$. The total efficiency for this energy range is 21%.

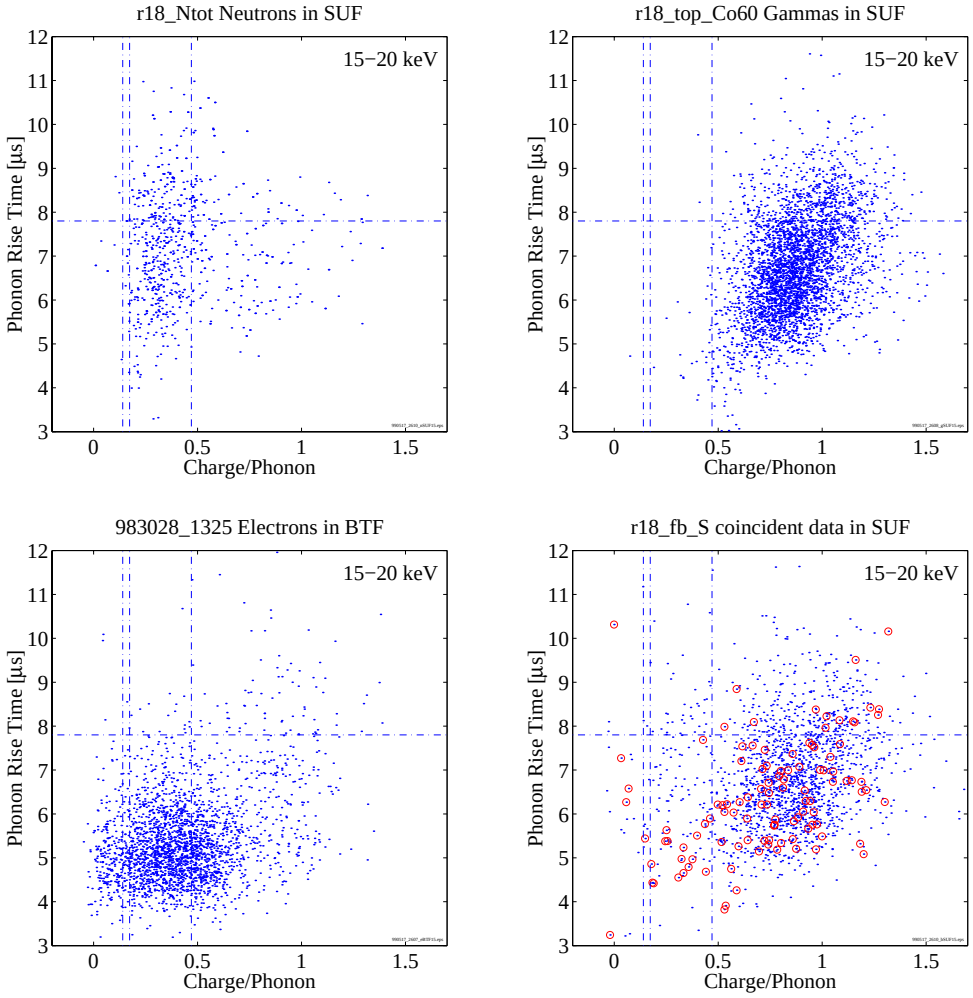

Figure 6.9: 4 sets of phonon rise time vs. Q/P 15-20 keV. The optimal phonon rise time position is 7.8 μs, the optimal Q/P value is 0.5. $\beta_r = 0.02$ and $\beta_y = 0.002$. The total efficiency for this energy range is 17%.

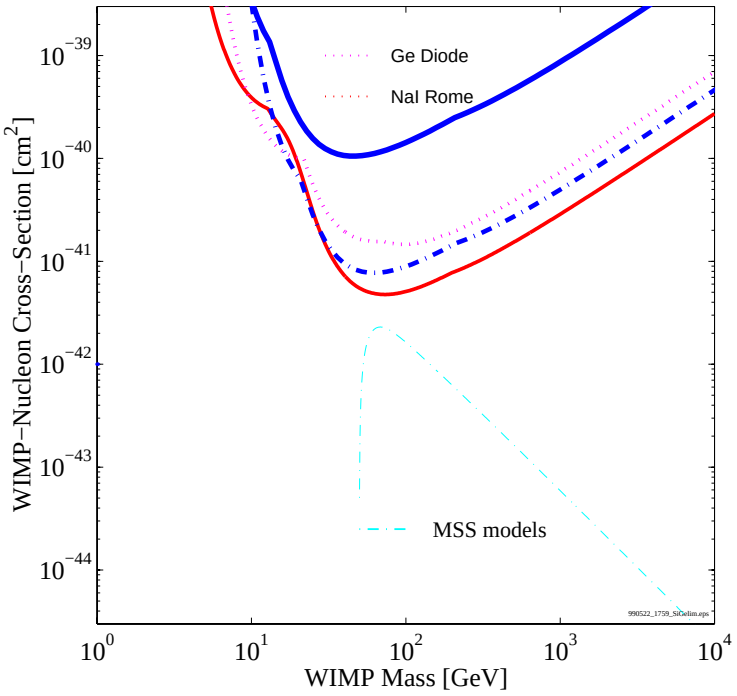

Figure 6.10: Plot of 90% confidence upper limits in the WIMP-nucleon cross section. Thick line is the limit from Alex, thick dashed line is the limit that would have been obtained if Alex was made of Ge. Silicon is about 15 times less sensitive to WIMPS than Ge for a given detector volume, since σ scales as A^2 and the density down by 2.3.

Chapter 7

Phonon Discrimination

7.1 Introduction

The idea of discriminating between electron and nuclear recoils using only phonons is not a new one. Using an enhanced ballistic phonon component from nuclear recoils looked quite promising[112] but later turned out to be too optimistic[113]. Titanium TES detectors have also been fabricated on thermal oxide layers[114] and have shown large phonon attenuation, although no comparisons between nuclear and electron recoils were made, and no bias voltage was applied to examine a possible difference in attenuation between Luke phonons and intrinsic phonons.

There are many intrinsic advantages to a phonon-based discrimination scheme. As phonon technology improves, the discrimination ability will clearly be limited by charge noise. This has a lower limit of ~ 50 electrons with a large capacitance detector ($\sim 40\,\mathrm{pF}$). Phonon discrimination will be continue to improve with greater phonon collection which may, in the future, give us a detector with less than 100 eV FWHM.

The proven spectral difference between phonons generated by an event and phonons generated by electron-hole pairs (Luke phonons) should enable us to use

the same nuclear recoil quenching factor for a phonon-based discrimination scheme. By applying a voltage bias across the crystal we will create more Luke phonons for electron recoils than for nuclear recoils by the ratio of the nuclear quenching factor. A material that could filter out high frequency phonons placed between some of the phonon sensors and the substrate would enable us to discriminate between gammas and neutrons. Let us examine in detail the operation of such a phonon filter device.

Charge-based discrimination suffers from a degradation in performance as the bias voltage is increased. Figure 7.1 shows a cartoon of the two systems. If one considers the separation in charge between a gamma (Q = $y\mathrm{E}_r$, where y is the ionization yield) and a neutron (Q = $f_n y\mathrm{E}_r$, where f_n is the nuclear quenching factor) of equivalent recoil energy E_r biased at a voltage V, we obtain

$$yE_r - f_n yE_r\left(\frac{1+yeV}{1+f_n yeV}\right) = \frac{(1-f_n)}{(1+f_n yeV)}E_r \tag{7.1}$$

which obviously depends on 1-f_n but decreases as 1+$f_n y$eV. The more voltage we apply to improve the charge collection, the worse discrimination we have. This is because one must correct for the different phonon energies that are added for gammas and neutrons. If we do the same analysis for a discriminating phonon detector the results are quite different. Assume that a fraction f_i of intrinsic phonons and a fraction f_l of Luke phonons are absorbed by the one of the detectors (P_α). We see that the separation is now

$$(f_i + f_l yeV)E_r - (f_i + f_n f_l yeV)E_r\left(\frac{1+yeV}{1+f_n yeV}\right) \tag{7.2}$$

$$= \frac{(f_l - f_i)(1-f_n)yeV}{(1+f_n yeV)}E_r \tag{7.3}$$

which has an extra yeV term. This essentially says that the phonon discrimination scheme will produce equivalent results if $(f_l - f_i)yeV \sim 1$. Including the ratio of

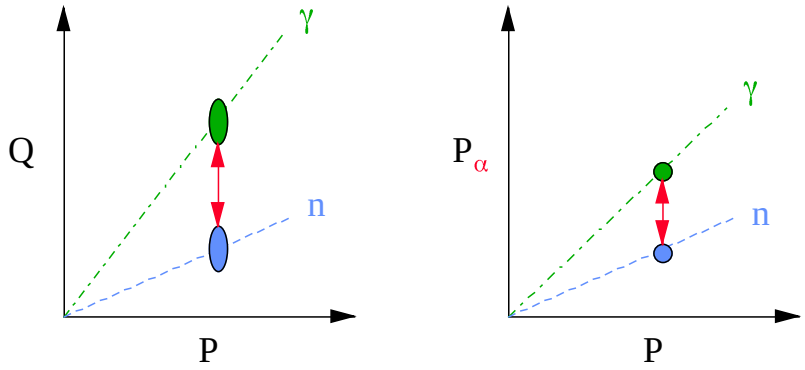

Figure 7.1: A cartoon of charge (Q) versus phonons (P) and filtered phonon signal (P_α) versus raw phonon signal. Noise in P_α is expected to be less than in Q. See text for a discussion of the increased discrimination ability of the second scheme.

charge to phonon noise, the full figure of merit is then

$$(f_l - f_i) yeV \frac{\sigma_q}{\sigma_{ph}} \tag{7.4}$$

So, for large voltages, the difference $(f_l - f_i)$ need not be large. The advantage of not being limited in bias voltage is quite significant since the threshold of a phonon sensor can be expressed as

$$threshold = N \frac{\sigma_{ph}}{1 + yeV} \tag{7.5}$$

where N is an arbitrary factor of about 3. In the extreme case, if we allow V to increase without bound, we will eventually be limited by the statistical noise in the number of generated charges. This will not present itself until

$$E_r > \frac{\sigma_{ph}^2}{(eV)^2 Fy} \tag{7.6}$$

where F is the Fano factor in silicon ($\sigma_{stat} = \sqrt{FyE_r}$). This statistical noise will

dominate the threshold when $eV \sim \sigma$ which will be around 500 volts.

Even without this constraint, there is another practical limit to the voltage that we will apply. The difference $(f_l - f_i)$ relies on a frequency difference between the intrinsic phonons and the Luke phonons. Since it can be shown that there is a roughly $eV^{2/5}$ dependence on the frequency of the Luke phonons[76], as the voltage increases our Luke fraction f_l will eventually equal our intrinsic fraction. This practical limit may be measured experimentally and could provide an additional confirmation of the frequency dependence of the Luke phonons.

7.2 Amorphous Materials

The next practical question which must be answered is whether it is possible to construct such a phonon filter. It has long been known that amorphous materials exhibit unusual thermal properties[115]. Many amorphous materials, such as SiO_2, photo resist, PMMA, epoxy, and sputtered Si and Ge, exhibit a plateau in thermal conductivity between 1 and 10 K[116, 117]. This effect is attributed to the localization of phonons that have a wavelength close to the characteristic length scale of disorder in the material. Since 10 K is equal to 200 GHz this represents a rapid reduction in mean free path exactly at the frequencies which interests us.

Direct experimental measurements of the phonon mean free paths in these materials have been made at a variety of temperatures. Using tunnel junctions fabricated on silicon with an amorphous SiO_2 layer, Dietsche and Kinder[118] found evidence for strong frequency dependent scattering proportional to v^{-3}. These experiments were performed around 1 K, and could an estimate of Λ_{ph} at lower temperatures. Later experiments in similar systems confirmed a strong frequency dependence but failed to confirm the inelastic mechanism claimed by Dietsch and Kinder[119]. A weak temperature dependence of the mean free path of 30-400 GHz phonons was

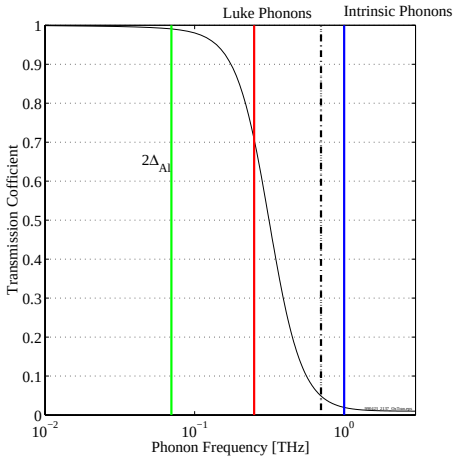

Figure 7.2: Estimated transmission coefficient for 50 nm of SiO_2 vs. frequency. Vertical lines are: $2\Delta_{Al}$ ($\sim$ 70 GHz), Luke phonons ($\sim$250 GHz), and Intrinsic phonons ($\sim$1 THz). Dotted vertical line is at 800 GHz where the mean free path of silicon reaches 1 cm.

found using picosecond optical techniques[120]. In this experiment the frequency dependence was weaker than ν^{-3} but stronger than ν^{-2}. In a very elegant series of experiments using tunnel junctions at 0.7 K Long[121] found a ν^{-4} dependent Λ_{ph} that was about 10 times smaller than bulk silicon at the equivalent frequency. A recent experiment by Mebert[122] using tin tunnel junctions suggests that the scattering mechanism may vary depending on the type of amorphous material. α-Si and α-Ge showed only elastic scattering processes, yet if SiO_2 was prepared in an oxygen or hydrogen atmosphere strong inelastic scattering was evident. A difference in preparation technique may therefor explain the discrepancy between the results of Kinder and those of Wolter. In terms of device manufacture it may in fact be possible to tune the frequency response of the amorphous films by adjusting the chemical composition, or the deposition techniques.

The phonon scattering mechanism is generally thought to be an elastic process

similar in formulation to isotopic scattering[123].

[Reference to Doug's thesis on scattering mechanisms[124]]

Phonons encounter domains of varying density and scatter off the perturbations created by them. The scattering is then expected to be fourth order in frequency and second order in density perturbation. If we assume the form and magnitude of the mean free path of amorphous SiO_2 as calculated in Graebner[116]

$$\Lambda_{1THz} = 1\nu^{-4}[nm] \tag{7.7}$$

and assume an elastic form of attenuation through backscattering, the transmission can be calculated by

$$T = \left(1 + \frac{t}{\Lambda}\right)^{-1} \tag{7.8}$$

Using equations 7.8 and 7.7 we can estimate the most effective thickness of amorphous SiO_2 (in terms of equation 7.4) by maximizing $(f_l - f_i)$. Luke phonons are expected to be at a frequency of $\sim$250 GHz and are known to be ballistic (see chapter 5) and intrinsic phonons are expected to be at $\sim$1 THz. This gives us an optimal thickness of about 50 nm. The transmission coefficient of this thickness of oxide as a function of frequency is plotted in figure 7.2. Luke phonons have a small expected attenuation of 70-80% while intrinsic phonons are almost completely blocked. Phonons close to the acceptance frequency of our detector ($2\Delta_{Al}$=70 GHz) are completely unaffected. The minimally ballistic phonon, with a frequency of about 700-800 GHz, will only have a small relative attenuation to intrinsic phonons. In the next section we will describe a device that was fabricated to these specifications.

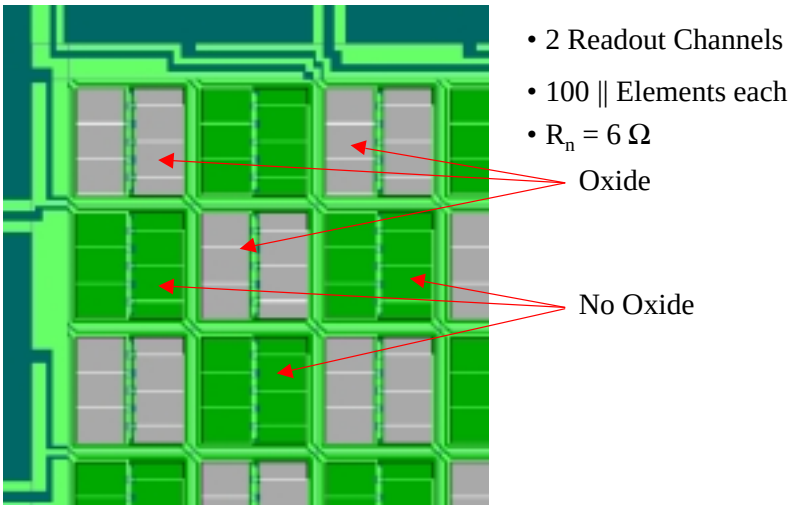

Figure 7.3: The physical layout of the oxide filter device. Every other sensor had an oxide filter layer so that each event would be shared as equally as possible. The Aluminum fins were only 150μm X 100μm, and the quasiparticle trap region was 10μm long. The TES itself was 270μm, slightly larger than the 250μm long TES of the Alex design.

7.3 Test Device

A specialized device was constructed to examine the possibility of a frequency dependent attenuation in SiO_2 leading to phonon-based discrimination. It consisted of two sensors, each having 100 parallel elements, interleaved in a checkerboard pattern that filled a 1 cm die. The voltage bias rails were connected along diagonals (see Fig. 7.3a) with one sensor's bond pads running horizontally and the other sensor's bond pads running vertically. This necessitated a large number of bonds on the perimeter of the device to ensure full connectivity for the separate diagonal rows. Also, the large number of bond pads created a situation where the area of the inactive metal was equal to that of the quasiparticle collection fins. The effect of this on the data will be discussed later. Figure 7.3 shows the upper left corner of an interleaved sensor pair. The length of a TES element was 270 μm and the width was 2 μm leading to

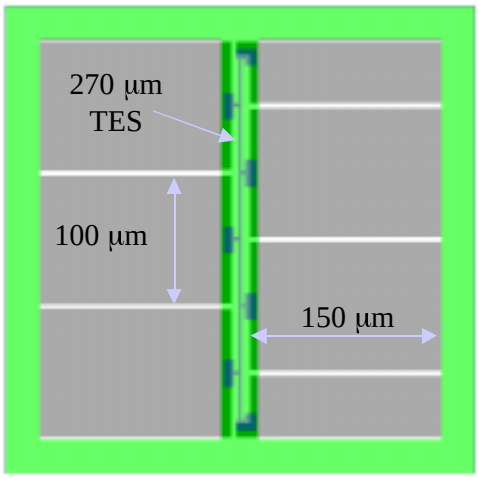

Figure 7.4: The physical layout of the oxide filter device. Every other sensor had an oxide filter layer so that each event would be shared as equally as possible. The Aluminum fins were only 150μm X 100μm, and the quasiparticle trap region was 10μm long. The TES itself was 270μm, slightly larger than the 250μm long TES of the Alex design.

an estimated 6.75 Ω normal resistance, given the 5 $\Omega/\square$ tungsten resistivity. Other aspects of the single QET element design were made similar to the Alex design. There were a total of seven quasiparticle collection fins per TES element, but they were much smaller than the ones on Alex since the area coverage requirement was very much more relaxed. Each fin was only 100 μm wide and 150 μm long. Based on estimates of the quasiparticle diffusion length, we expect close to the theoretical maximum in energy collection for this device. Figure 7.4 shows a close up of the individual sensor element.

The goal of this device was also to be as fast as possible to detect any difference in the arrival time of the different phonon species. The shortening of the quasiparticle fins would reduce the diffusion time to $\sim$1 μs, so the W/Al overlap region leading to the W spurs was shortened to 5 μm on each side. The W spurs, like the Alex design, were 4 μm long.

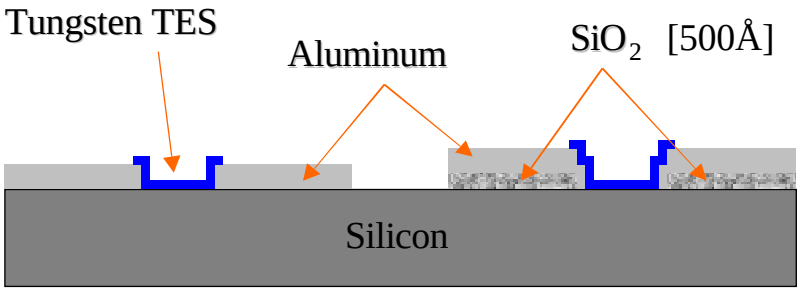

Figure 7.5: The process layers of the oxide filter device. Note that amorphous silicon exists only under the aluminum quasiparticle fins and not below the tungsten TES. This was to prevent any variation in T_c due to substrate conditions.

The substrate used was a 1 mm thick 2 kΩ-cm p-type [100] 3 inch silicon wafer. An oxide layer of 50 nm was grown prior to any the application of any metal film to the substrate. Etching of the oxide was performed with dilute HF after a patterning step to define the checkerboard pattern. Alignment marks were laid down in the oxide in the same step (See Fig. 7.5) to allow the registration of the QET sensor on the oxide layer. Subsequent patterning was very similar to the processing of a standard QET device and the sensors over the oxide were identical to the ones without oxide. Aluminum fins were 150 nm thick and completely covered the oxide below. This was to ensure that the presence of exposed oxide in the sputtering chamber would not degrade the T_c of the tungsten. The final TES tungsten was the standard 35 nm. Although the TES was not placed over an oxide layer, and so not subject to the filtering effect directly, the area ratio was only 1% of the aluminum area. Any effect associated with the direct absorption of phonons into the TES would be small.

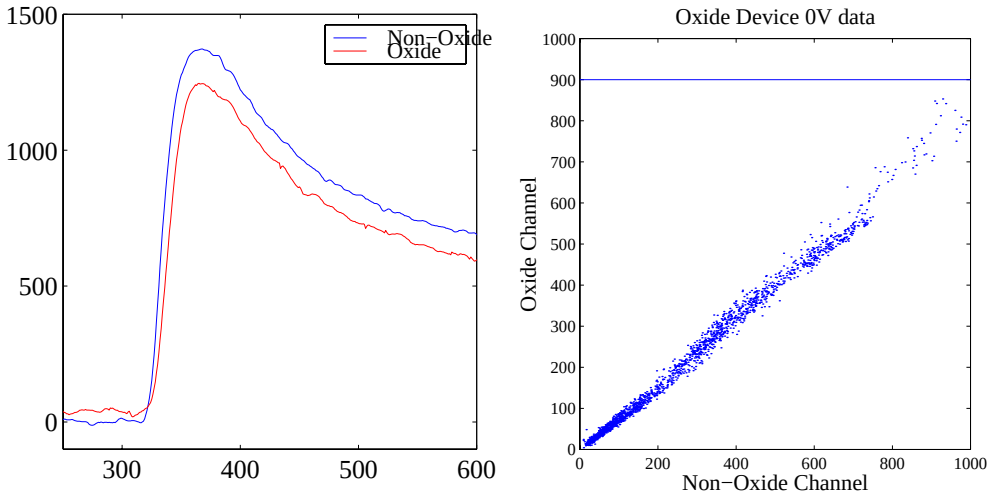

Figure 7.6: a. A set of sample pulses from the oxide and non-oxide sensor. The horizontal axis is in tenths of μs. Rise times were $\sim 1\,\mu$s and fall times were $\sim 50\,\mu$s. b. A plot of signal height in A vs. signal height in B. The 60 keV photons are spread by a factor of 2 and clearly shows evidence of downconversion.

7.4 Results

The two devices were very well matched in critical parameters. The superconducting transition temperature was 140 mK, and was the same in both sensors to ~ 0.1 mK. The resistance was very close to the design value of $6.75\,\Omega$ in both sensors ($\pm\, 0.25\,\Omega$), which was strong evidence of full connectivity. The phonon sensors had rise times of $\sim 1\,\mu$s, taking advantage of the short quasiparticle diffusion length (see figure 7.4). Fall times were on the order of 50 μs. IbIs data was taken at a variety of temperatures to ensure that both sensors were identical in all respects.

Figure 7.6a shows pulses from the two sensors. The resolution of each sensor was ~ 1 keV FWHM, taking the maximum of the 60 keV swath as an energy calibration. Note the clear signature of a ballistic component in the peaked structure of the pulse in the first 10 μs. There was no visible difference in the rise times or fall times in

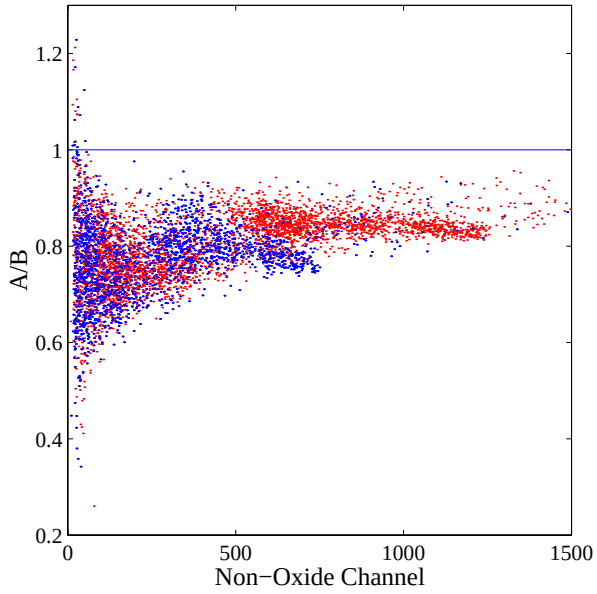

Figure 7.7: Plot of signal height ratio of oxide over non-oxide versus height in non-oxide sensor for 0 volts and 3 volts. The smear in the 60 keV photons is from down conversion of phonons in the perimeter metal layer.

the two detectors. The sensor with the smaller pulse ($\sim 85\%$) was in fact the sensor with 50 nm of Oxide. This difference could have easily been due to different shunt resistors, creating different voltage biases and therefor different signal heights.

If we assume that this attenuation is actually due to oxide, we measure a 200 nm ($\pm$ 50 nm) mean free path for intrinsic phonons in our thermal oxide. A much more likely explanation is that the 80% line is realy due to electronics and the attenuation is the difference in ratio across the 60 keV peak. If we use this ratio of more like 90% we find a mean free path of about 500 nm. Both of these estimates are much longer than the previously measured value of 20-35 nm at 875 GHz[122]. Either there is a systematic difference in the preparation of the thermal oxides used in the two experiments, or there is an unforseen temperature effect. From measurements made

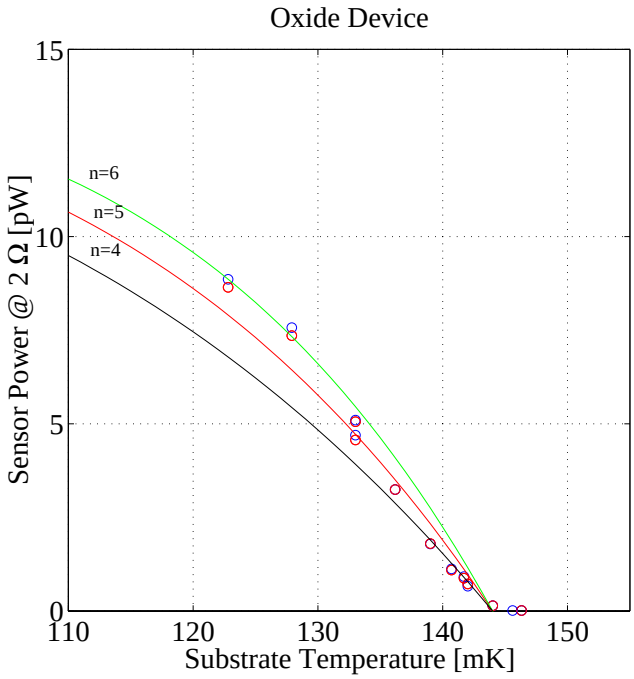

Figure 7.8: Plot of power dissipated vs. substrate temperature for one of the oxide sensors. Curves represent a T^4, T^5, and T^6 thermal conductivity dependence. At low powers ($T_s > 130\,\mathrm{mK}$) a T^5 dependence appears to be the best fit.

on the dark matter detectors, we have great confidence that the Luke phonons are of low frequency.

The energy resolution of this detector allows us to estimate the improvement in collection efficiency from the shorter aluminum fins. From equation 2.15 we calculate a FWHM that would be five times worse than Alex. This comes from the elevated T_c of 140 mK and the smaller W area by a factor of 4 (100 - 2 X 270 X 0.035 compared to 444 - 2 X 250 X 0.035). The resolution was only about twice as bad implying a 2.5 times better collection efficiency, or $\approx 4\%$ total phonon collection.

Figure 7.7 shows the ratio of sensor A over sensor B plotted versus sensor B for two voltages. We explain the spread in phonon energy of the 60 keV photons by the

downconversion of phonons at the edges of the detector. The area coverage of bond pads compared to collector fins are about equal, as are the number of events in the high and low portion of the 60 keV peak. Thus, downconverted phonons (that have interacted once in an inactive metal layer) show a systematically smaller phonon attenuation than the undownconverted phonons. This is a proof of concept of the principle of phonon discrimination. Unfortunately the effect is small (of order 10%) and did not create a measurable shift in the ratio of neutrons to gammas at any bias voltage. The next step is clearly to fabricate a device with a much thicker oxide (or other suitable amorphous material) commensurate with the correct mean free path.

Finally, by taking repeated IbIs curves as the substrate temperature was swept, we could attempt to measure the thermal conductivity exponent and confirm an electron-phonon decoupling form of T^5. At each temperature the full V vs. Ib, R vs. Ib, and P vs. Ib was deconvolved. We then took the value of the power the TES was flowing into the substrate while at a resistance of $2\,\Omega$ at each substrate temperature. In figure 7.8 we plot the results of this study. Included in the plot are curves representing a T^4, T^5, and T^6 thermal conductivity dependence. The data is not conclusive in differentiating between these exponents.

Chapter 8

Future Improvements

The rapid progress that has been acheived with this new QET-based dark matter detector has been remarkable. There has been a factor of 10 or more improvement in signal to noise, athermal phonon physics has been probed, and a promising dark matter result has been acheived. We are now in the position to talk about goals which the author believes are attainable in the short term.

8.1 600mK SQUID system

The noise of the detector, in its present tower configuration, is dominated by the johnson noise of the voltage bias resistor placed on the 4 K stage of the tower (see chapter 2 and chapter 4). Figure 8.1 shows a series of noise measurements versus current bias with the theory (Equation 2.14) in a solid line. By moving this bias resistor to 600 mK and lowering the value to 10 mΩ the relevant product would be $T_b R_b = 6\,mK\Omega$ whereas the sensor would have $T_s R_s \sim 14\,mK\Omega$. The engineering task to move these components is significant, however, and required the manufacture of many new cryogenic parts. Figure 8.2 is a diagram of the top of the tower with the new 're-entrant' 600 mK SQUID system depicted. The advantages of this system are

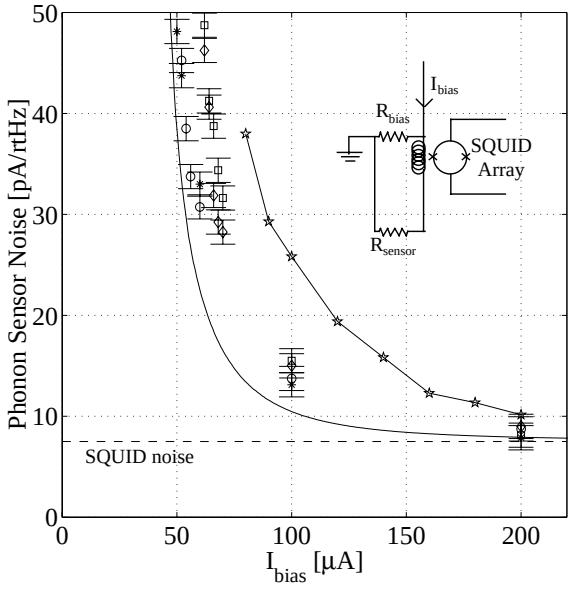

Figure 8.1: A plot of sensor noise vs. current bias, measurement and theory, with SQUID noise shown as the dotted horizontal line. Also shown is

not limited to the improvement gained in baseline noise. In the hybrid SQUID/FET card, the SQUID operating point was directly affected by the bias point of the heated JFETs. This was a subtle type of cross talk and greatly frustrated the setup proceedure. The movement of the SQUIDs to a different temperature stage should completely eliminate any interference between the SQUID and FET systems.

Since the task of mounting the SQUID chips on the tower face proved too difficult, it was decided to create an area on the top of the tower that was thermally connected to the Still flange. Wiring to the FET card would be superconducting, and therfore cause a negligible heat leak. The current signal from the sensor below would now travel up the tower face to 4 K, jump across to the 600 mK card containing SQUIDs and bias resistors, and then back to the 4 K FET card for a common ground. See figure 8.3 for a schematic of the new re-entrant design with temperature stages and

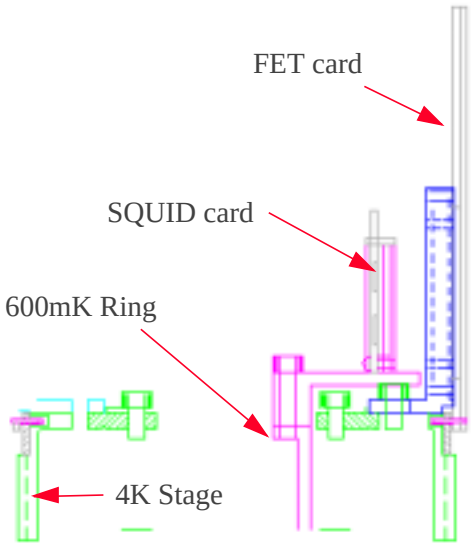

Figure 8.2: A diagram of the 600mK SQUID system showing the 600mK interface ring, a 4K FET card and the top section of a tower.

4 K to 600 mK with jumpers labeled.

8.2 Close Packed Detectors

A redesign of the detector housing was long overdue. The original mount (see chapter 4) was very labour intensive, and used materials that are now know to be unacceptable in terms of radiopurity. The phosphor bronze fingers have high levels of ^{40}K (20 ppm as measured by Al Smith) a high energy beta emitter. Kapton feet will now be used on all portions of the detector mount. The primary worry in this scheme is that the thermal conductivity would be insufficient through the Kapton to cool the detectors. A simple calculation will allow us to lay this fear to rest. The heat capacity of germanium at 1 K is approximately $1900(1/300)^3 \approx 7 \times 10^{-5}$ J/mol.

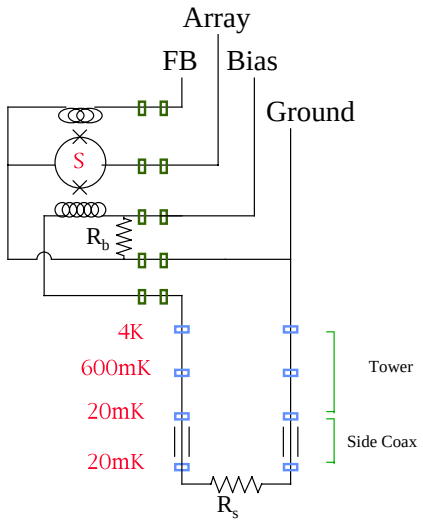

Figure 8.3: A schematic of the 600mK phonon sensor circuit. Five flying wire fly-overs are required for each sensor. Connection are shown as small boxes. The temperature of each point of parasitic resistance is shown.

Our detectors will weigh about 4 moles so they contain about helf a milliJoule of energy. Kapton has a conductivity of about 6×10^{-3} W/m/K so for a length scale of about a centimeter (1 mm thick, contact area 0.1 cm^2) we get a c/g time constant of ~ 5 seconds. This is acceptable. At 100 mK the time constant is reduced to about 1/2 second since the conductivity of Kapton goes like $T^{1.8}$ and the heat capacity of germanium goes like T^3.

The packing fraction on the old mount was only 50% (at best) due to the circuit boards and the copper rings, and two detectors did not have an unobscured view of each other. The future design (see fig. 8.4) will have only 2 mm between detectors and a clear, unobscured view of the adjacent silicon or germanium surface. The gap between the detector and the mount must be atleast 1 mm to avoid a large parasitic capacitance.

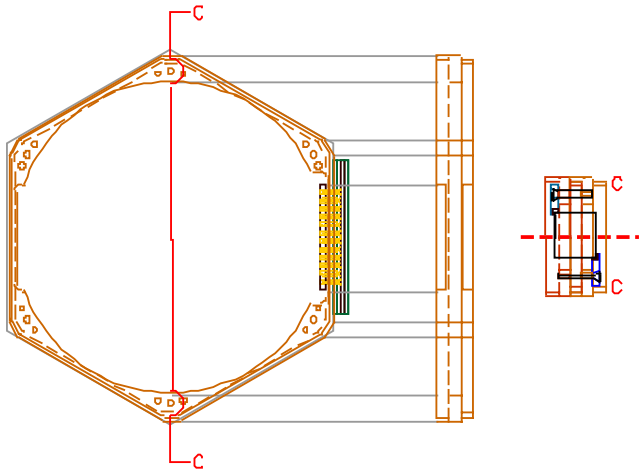

Figure 8.4: A design drawing of the new close-packed detector mount. MillMax sockets now are now in the same plane as the detector to save vertical space. To the right is a view of one face of the hexagon with a 1 cm detector inserted.

8.3 Double Sided Detector

If viable phonon discrimination could be proven in smaller devices (see chapter 7) it would be straight forward to extrapolate the technique for larger detectors. Figure 8.5 shows a schematic of how this detector might be configured. A double sided phonon detector could be patterned with two sensors on each side. Rotating the axis of symmetry would preserve the X-Y resolution, while adding the relative timing across the crystal to determine depth. One side of the detector would be constructed with a phonon filter material, to allow discrimination. This phonon sensor would have to be floated at a voltage relative to ground (and the other sensor) to create the necessary Luke phonons. Such a detector could be installed into the tower, new copper mounts, and present room temperature electronics with minimal impact on the infrastructure.

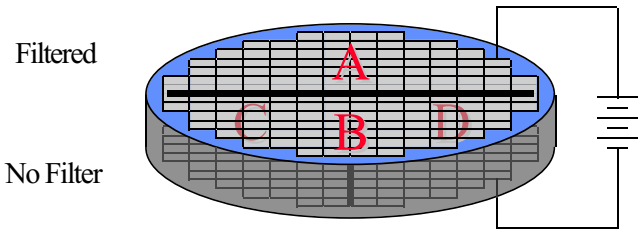

Figure 8.5: A double sided detector employing phonon-based discrimination. Each side would have two phonon sensors, set at right angles to maintain X-Y position sensitivity. One side would have a coating that would attenuate intrinsic phonons and the other would be unaltered.

8.4 SQUID preamplifier system

The limit in energy collection discussed in chapter 2 due to the lower limit on the normal resistance of the sensor can be overcome by using a single SQUID as a preamplifier to the array of SQUIDs that is used at present[125]. Such a single SQUID could have an input coil with an inductance of a few nH [ref.] or ∼200 times less than the presently employed array. This would allow the sensor itself to have a normal resistance 200 times less than at present (or a few mΩ) and maintain the same bandwidth allowed by L/R. This SQUID could be placed close to the detector to limit the parasitic inductance, because the power dissipated would only be ∼5nW. It would be *voltage* biased with a shunt resistor (∼20mΩ) placed at 600mK and the SQUID array would measure the it current modulation in much the same way that the array is used to measure the sensor in the present design.

The main advantage of this approach is that the entire surface of the detector can now be covered by the aluminum quasiparticle collector fins. This would allow collection efficiencies to approach the fundamental limit of about 25%. It would also minimize multiple-bounce phonon collection created by the grid solution and allow an improvement in timing accuracy.

Another advantage of this is that one could decrease the total area of tungsten, thus decreasing the equilibrium power that the TES must dissipate into the substrate. Using a simple scaling, if the number of TES elements must be increased by a factor of 5 to enable maximum collection efficiency, the length of each TES would have to be decreased by the same factor to keep the total tungsten volume the same. This would imply a normal resistance of 80 mΩ (25 times less than the Alex design). Assuming that the TES would require a voltage bias of $\sim 2\mu$V, this would mean that the bias resistor could be no smaller than 500 $\mu\Omega$ from the practical limit of $\sim$4 mA that one could sink down the striplines. If we push the normal resistance down to 40 mΩ the power dissipated to the substrate would then drop by half.

Lets examine the case where R_n=40mΩ, $R_b = 5\mu\Omega$, a bias point of $R_s = 4$mΩ, T_c=95mK, and a collection efficiency 25 times larger than the Alex detector. The Alex detector was blessed with a T_c of 65 mK, the shift to 95 gives us an automatic loss in signal to noise of $\left(\frac{95}{65}\right)^3 \approx 3$. We gain all of this back and more from the factor of 25 in collection efficiency and the factor of $\sqrt{2}$ from the lower power dissipation. In the end we would have a detector with more than ten times the signal to noise in the Alex design. If we assume that we can achieve a T_c of 70 mK (using the new Fe implantation techniques developed by B.A. Young), and maintain the 25% collection efficiency, it is forseeable that we may be blessed in the near future with a phonon detector that has $\sim$ 10 eV FWHM resolution.

An simple wiring diagram (with temperature stages) of this 'two-stage' detector is shown in Figure 8.6 to illustrate the ease to which such a scheme could be implemented. The correspondences between this and the present detector scheme are so great in fact that the exact same room temperature electronics (in 3U or 9U format) could be employed with minor wiring reallocations.

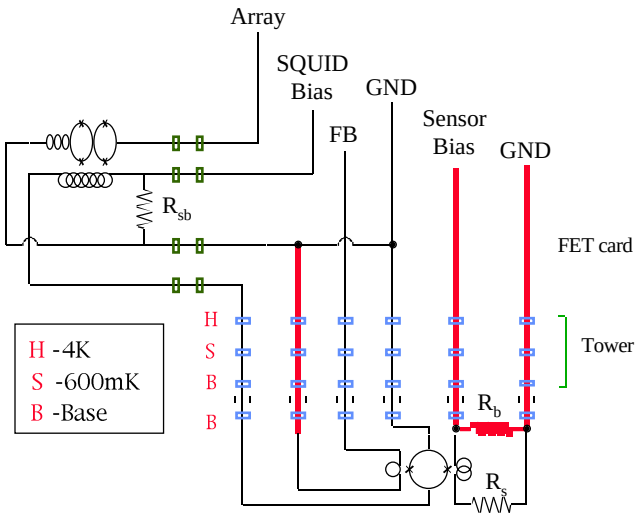

Figure 8.6: A circuit diagram of a two stage SQUID system for the tower geometry. Two feedback lines are now required: one active on the first stage single SQUID, and one passive on the array (to maintain the appropriate position on the V-Phi curve). Note: double lines represent wires that are not repeated for each sensor. The total number of wires (from 4K to base) using this system and four phonon sensors would be 15.

Chapter 9

Conclusion

Created 100g detector

Measured Surface electrons

Appendix A

Analysis Code

A.1 Description

Analysis algorithms were coded in matlab with some embedded C routines (initially coded by S.W. Nam and later improved and documented by R. Schnee and S. Golwala). The goal of the analysis software was to derive useful quantities from the raw pulse data as fast as possible. The point of including the software here is to provide a snapshot of the code as it was used in Run 18 and in the electron calibration runs. The author acknowledges the enormous room for improvement, and encourages criticism of the methods presented here.

A.2 Matlab code

A.2.1 Height and Delay estimation

[crap,tcrap,submF2(:,F2PApk),submF2(:,F2PAdel)]= ...

speed_racer(F2maxdelay,F2delstart,F2maxdelay,F2Pfunct,F2_arise,1);

```
Prise=5; %Phonon rise time in us%
trise=Prise*F2samplerate; %convert to digitization rate of 10 MHz%
Pfall=20; %Phonon fall time ***for the filter*** in us%%
tfall=Pfall*F2samplerate; %convert to digitization rate of 10 MHz%
F2Pfunct=tfall*((t>0).*(exp(-(t)/tfall)-exp(-(t)/trise))- ...
(t<0).*(exp((t)/tfall)-exp((t)/trise)))/(tfall-trise);
%filter function for phonons%
F2Pfunct=F2Pfunct/sum(F2Pfunct(t>0));
```

A.2.2 Rise time estimation

```
function [start,rt,ft] = rtft_f (tracem,prisebase,qrtf,prtf);
%function [start,rt,ft]=rtft_f(tracem,prisebase,qrtf,prtf);
%
% Finds 20 to 80 rise time of pulses
% Finds 1/e fall time of pulses
%
% Very susceptable to glitching
%
% tracem = rise portion of trace
% prisebase = indices of bins used to find baseline
% qrtf = q parameter for risetime filter
% prtf = p parameter for risetime filter
%
% Nov. 24 96 RMC
% Renamed as of Sept. 28 1997 RMC (was F1Prtft)
% rws 14 Oct 97 Added comments
% rws 29 Oct 97 Changed to use booleans to speed up (25
```

```
% This is still slow enough it should be made into a mex-function!
% RMC 12 Nov 97 Added a filter to allow a better rise time determination
% rws 18 Nov 97 fixed bug: now flip trace back after refiltering
temp=size(tracem);
cols=temp(2);
rows=temp(1);
base=mean(tracem(prisebase,:)); % find the baseline
tracem=tracem-base(ones(rows,1),:); % subtract off the baseline
% filter trace with no time delay
tracem = filter(qrtf,prtf,tracem);
% This runs the filter backwards to
% remove the time delay
tracem=flipud(tracem);
tracem = filter(qrtf,prtf,tracem);
tracem=flipud(tracem);
[peak,idx]=max(tracem);
mididx=idx;highidx=idx;lowidx=idx;ftidx=idx;
for i=1:cols; % do for each event in turn
%move from peak down to last 50% point before peak:
temp = find( tracem(:,i) <= .5*peak(i) ); % bins below 50%
temp = temp(temp<idx(i)); % pre-peak bins below 50%
if isempty(temp)
mididx(i) = 1;
else
mididx(i) = temp(length(temp)); % last pre-peak bin below 50%
end
%move from last 50% point back up to first 80% point:
```

```
temp = find( tracem(:,i) >= .8*peak(i) ); % bins above 80%
temp = temp(temp¿mididx(i)); % post-50% bins above 80%
if isempty(temp)
highidx(i) = idx(i);
else
highidx(i) = temp(1); % first post-50% bin above 80%
end
%move from last 50% point down to last 20% point:
temp = find( tracem(:,i) <= .2*peak(i) ); % bins below 20%
temp = temp(temp<mididx(i)); % pre-50% bins below 20%
if isempty(temp)
lowidx(i) = 1;
else
lowidx(i) = temp(length(temp)); % last pre-50% bins below 20%
end
%move from peak down to first 37% point after peak:
temp = find( tracem(:,i) <= .37*peak(i) ); % bins below 37%
temp = temp(temp>idx(i)); % post-peak bins below 37%
if isempty(temp)
ftidx(i) = rows;
else
ftidx(i) = temp(1); % first post-peak bin below 37%
end
end
ft=ftidx'-idx';
rt=1.5850*(highidx'-lowidx'); % Converts risetime from 20-80 to 10-90
start=lowidx';
```

```
%% qrtf and prtf are the filter parameters
%% set at 90 kHz to help the determination
%% of the rise times
rtf_cfreq=2*0.09/F2samplerate;
[qrtf,prtf]=butter(3,rtf_cfreq);
```

Bibliography

[1] V. trimble. existence and nature of dark matter in the universe. *Ann. Rev. Astron. Astrophysics*, 25:425–72, 1985.

[2] David R. Lide, editor. *handbook of chemistry and physics.* CRC press, 1992.

[3] David Leverington. *A history of astronomy from 1890 to the present.* Springer-Verlag, 1995.

[4] J.A. Willick. Measurement of galaxy distances. *astro-ph*, 9610200:1–39, 1996.

[5] M.S. Longair. *Galaxy Formation.* Springer, 1998.

[6] B. Moore. Constraints on the global mass-to-light ratios and on the extent of dark matter halos in globular clusters and dwarf spheroidals. *Astrophysical Journal, Letters*, 461:L13–16, 1996.

[7] F. Zwicky. *Helv. Physica Acta*, 6:110, 1933.

[8] D. Merritt. The distribution of dark matter in the coma cluster. *Astrophysical Journal*, 313:121–35, 1987.

[9] E. Ellingson *et al.* The cnoc cluster redshift survey catalogs. vi. ms 0015.9+1609 and ms 0451.5-0305. *Astrophysical Journal Supplement Series*, 116:247–62, 1998.

[10] R.G. Carlberg *et al.* The cnoc cluster survey. In *Early Universe with the VLT*, volume 1, pages 231–8, 1996.

[11] P. Schneider. *Gravitational lenses.* Springer-Verlag, 1992.

[12] F. Zwicky. On the probability of detecting nebulae which act as gravitational lenses. *Physical Review*, 51:679, 1937.

[13] D. Walsh *et al.* 0957+561 a, b: twin quasistellar objects or gravitational lens? *Nature*, 279:381–4, 1979.

[14] R. Narayan. A review of astrophysical results from gravitational lensing. *New Astron. Rev. (Netherlands), New Astronomy Reviews*, 42:73–9, 1998.

[15] M.R.S. Hawkins. Evidence for dark galaxies. *New Astron. Rev. (Netherlands), New Astronomy Reviews*, 42:85–8, 1998.

[16] H. Hoekstra *et al.* A weak lensing analysis of cl 1358+62. *New Astron. Rev. (Netherlands), New Astronomy Reviews*, 42:137–40, 1998.

[17] H.M. AbdelSalam. Mass reconstruction from combined strong and weak lensing. *New Astron. Rev. (Netherlands), New Astronomy Reviews*, 42:157–61, 1998.

[18] P. Fischer. A new weak lensing analysis of ms1224.7+2007. *astro-ph*, 9901407:1–22, 1999.

[19] G. Gamow. *My World Line.* Viking Press, 1970.

[20] K.A. Olive. big bang nucleosynthesis. *astro-ph*, 9903309, 1999.

[21] R.A. Alpher *et al. Physical Review*, 73:803, 1948.

[22] P.J.E. Peebles. primeval helium abundance and the primeval fireball. *Physical Review Letters*, 16:410, 1966.

[23] R.V. Wagoner *et al.* on the synthesis of elements at very high temperatures. *the astrophysical journal*, 148:3–49, 1966.

[24] G. Gamow. expanding universe and the origin of elements. *Physical Review*, 70:571, 1946.

[25] R.V. Wagoner. Big-bang nucleosynthesis revisited. *Astrophysical Journal*, 179:343–60, 1973.

[26] Edward W Kolb. *The early universe.* Addison-Wesley, 1990.

[27] K.A. Olive and G. Steigman. A new look at neutrino limits from big bang nucleosynthesis. *Physics Letters B*, 354:357–62, 1995.

[28] L.M. Krauss and P.J. Kernan. Big bang nucleosynthesis constraints and light element abundance estimates. *Physics Letters B*, 347:347–53, 1995.

[29] C.J. Hogan. *Big Bang Nucleosynthesis and the Observed abundances of the Light elements*, chapter 1, page 50. World Scientific, 1997.

[30] J.A. Willick *et al.* Homogeneous velocity-distance data for peculiar velocity analysis. iii. the mark iii catalog of galaxy peculiar velocities. *Astrophysical Journal Supplement Series*, 109:333–66, 1997.

[31] A. Dekel and M.J. Rees. Omega from velocities in voids. *Astrophysical Journal, Letters*, 422:L1–4, 1994.

[32] K. Griest and K. Griest. Galactic microlensing as a method of detecting massive compact halo objects. *Astrophysical Journal*, 366:412–21, 1991.

[33] M. Kamionkowski. Microlensing by stars. *Astrophysical Journal, Letters*, 442:L9–12, 1995.

[34] C. Alcock *et al.* Possible gravitational microlensing of a star in the large magellanic cloud. *Nature*, 365:621–3, 1993.

[35] E. Aubourg *et al.* Evidence for gravitational microlensing by dark objects in the galactic halo. *Nature*, 365:623–5, 1993.

[36] A. Udalski *et al.* The optical gravitational lensing experiment, discovery of the first candidate microlensing event in the direction of the galactic bulge. *Acta Astronomica*, 43:289–94, 1993.

[37] D. Bennett. Magellanic cloud gravitational microlensing results: what do they mean? *Phys. Rep. (Netherlands), Physics Reports*, 307:97–106, 1998.

[38] D.P. Bennett *et al.* Planetary microlensing from the macho project. *Astron. Soc. Pac. Conf. Ser. (USA), Astronomical Society of the Pacific*, 119:95–9, 1997.

[39] B. Paczynski *et al.* Results from the optical gravitational lensing experiment (ogle). *Int. Astron. Union Symp. (Netherlands), International Astronomical Union*, pages 93–102, 1996.

[40] D. Branch. The hubble constant from nickel radioactivity in type ia supernovae. *Astrophysical Journal*, 392:35–40, 1992.

[41] S. Perlmutter *et al.* High-redshift supernovae discoveries on demand. *Nuclear Physics B (Proc. Suppl.)*, 51B:20–29, 1996.

[42] A.V. Filippenko and A.G. Riess. Type ia supernovae and their cosmological implications. *astro-ph*, 9905049:1–16, 1999.

[43] A.A. Penzias and R.W. Wilson. A measurement of excess antenna temperature at 4080 mc/s. *Astrophysical Journal*, 142:419, 1965.

[44] M. Kamionkowski and A. Kosowsky. The cosmic microwave background and particle physics. *astro-ph*, 9904108:1–43, 1999.

[45] B.E. Corey and D.T. Wilkinson. A measurement of the cosmic microwave background anisotropy at 19 ghz. *Bull. Am. Astron. Soc.*, 8:351, 1976.

[46] G.F. Smoot *et al.* Detection of anisotropy in the cosmic blackbody radiation. *Physical Review Letters*, 39:898–901, 1977.

[47] G. Smoot *et al.* Cobe differential microwave radiometers: instrument design and implementation. *Astrophysical Journal*, 360:685–95, 1990.

[48] A.N. Lasenby *et al.* Observations of the cosmic microwave background and implications for cosmology and large-scale structure. *Philos. Trans. R. Soc. Lond. A, Math. Phys. Eng. Sci. (UK), Philosophical*, 357:35–56, 1999.

[49] Y. Fukuda *et al.* Evidence for oscillation of atmospheric neutrinos. *Physical Review Letters*, 81:1562–7, 1998.

[50] J.R. Primack and M.A.K. Gross. Cold + hot dark matter after superkamiokande. *astro-ph*, 9810204:1–8, 1998.

[51] R.D. Peccei and H.R. Quinn. Cp conservation in the presence of pseudoparticles. *Physical Review Letters*, 38:1440–3, 1977.

[52] R.D. Peccei and H.R. Quinn. Constraints imposed by cp conservation in the presence of a pseudoparticle. *Physical Review D (Particles and Fields)*, 16:1791–7, 1977.

[53] S. Weinberg. A new light boson? *Physical Review Letters*, 40:223–6, 1978.

[54] E.P.S. Shellard and R.A. Battye. Origin of dark matter axions. *Phys. Rep. (Netherlands), Physics Reports*, 307:227–34, 1998.

[55] G. Jungman *et al.* Supersymmetric dark matter. *Physics Reports*, 267:195–373, 1996.

[56] L. Baudis *et al.* New limits on dark-matter weakly interacting particles from the heidelberg-moscow experiment. *Physical Review D*, 59:022001/1–5, 1999.

[57] L. Baudis *et al.* Direct detection of wimps with the hdms-experiment and new wimp-limits from the heidelberg-moscow experiment. *Phys. Rep. (Netherlands), Physics Reports*, 307:291–5, 1998.

[58] L. Baudis *et al.* Genius: a new dark matter project. *Phys. Rep. (Netherlands), Physics Reports*, 307:301–8, 1998.

[59] P. Belli *et al.* The dama experiments at gran sasso. *Phys. Rep. (Netherlands), Physics Reports*, 307:269–73, 1998.

[60] P.F. Smith *et al.* Improved dark matter limits from pulse shape discrimination in a low background sodium iodide detector at the boulby mine. *Physics Letters B*, 379:299–308, 1996.

[61] P.F. Smith *et al.* Dark matter experiments at the uk boulby mine. *Phys. Rep. (Netherlands), Physics Reports*, 307:275–82, 1998.

[62] D. LHote *et al.* Systematic study of massive germanium pin diode detectors at 20 mk. *Nucl. Instrum. Methods Phys. Res. A, Accel. Spectrom. Detect. Assoc. Equip.*, 370:193–5, 1996.

[63] D. Drain *et al.* Status of the edelweiss experiment. *Phys. Rep. (Netherlands), Physics Reports*, 307:297–300, 1998.

[64] J.D. Lewin and P.F. Smith. Review of mathematics, numerical factors, and corrections for dark matter experiments based on elastic nuclear recoil. *Astroparticle Physics*, 6:87–112, 1996.

[65] E.I. Gates *et al.* The local halo density. *Astrophysical Journal, Letters*, 449:L123–6, 1995.

[66] B. Sadoulet. Cryogenic detectors of particles: hopes and challenges. *IEEE Trans. Nucl. Sci. (USA), IEEE Transactions on Nuclear Science*, 35:47–54, 1988.

[67] B. Cabrera *et al.* Bolometric detection of neutrinos. *Physical Review Letters*, 55:25–8, 1985.

[68] T. Peterreins *et al.* A new detector of nuclear radiation based on ballistic phonon propagation in single crystals at low temperatures. *Physics Letters B*, 202:161–8, 1988.

[69] B. Neuhauser *et al.* Acoustic detection of single particles for neutrino experiments and dark matter searches. *IEEE Trans. Magn. (USA), IEEE Transactions on Magnetics*, pages 469–72, 1987.

[70] S. Tamura and H.J. Maris. Spontaneous decay of la phonons. *Physical Review B (Condensed Matter)*, 31:2595–8, 1985.

[71] James P. Wolfe. *Imaging Phonons.* Cambridge University Press, 1998.

[72] H. Maris. The vibrational spectrum of an isotopically disordered crystal. *Philos. Mag.*, 13:465, 1966.

[73] S. Tamura. Numerical evidence for the bottleneck frequency of quasidiffusive acoustic phonons. *Physical Review B (Condensed Matter)*, 56:13630–3, 1997.

[74] P.N. Luke. Voltage-assisted calorimetric ionization detector. *J. Appl. Phys.*, 64:6858–60, 1988.

[75] B.S. Neganov and V.N. Trofimov. A possible massive ultrasensitive heat detector at a temperature close to absolute zero. *Pis'ma v Zhurnal Eksperimental'noi i Teoreticheskoi Fiziki*, 28:356–8, 1978.

[76] B. Cabrera *et al.* Prompt phonon signals from particle interactions in si crystals. *J. Low Temp. Phys. (USA), Journal of Low Temperature Physics*, 93:365–75, 1993.

[77] N.E. Booth. Quasiparticle trapping and the quasiparticle multiplier. *Applied Physics Letters*, 50:293–5, 1987.

[78] W.A. Little. The transport of heat between dissimilar solids at low temperatures. *Can. J. Phys.*, 37:334–349, 1959.

[79] S.B. Kaplan *et al.* Quasiparticle and phonon lifetimes in superconductors. *Physical Review B*, 14:4854–4873, 1976.

[80] K.E. Gray. Steady state measurements of the quasiparticle lifetime in superconducting aluminum. *J. Phys. F*, 1:290–308, 1971.

[81] A. Mrzyglod and O. Weis. Mean free path of thz phonons in aluminum films. *Journal of Low Temperature Physics*, 97:275–286, 1994.

[82] Paul Brink. Efficiency of quasiparticle generation. Group Discussion, 1996.

[83] S.M. Grannan *et al.* Collection of athermal phonons into doped ge thermistors using quasiparticle trapping. *Journal of Applied Physics*, 77:4887–91, 1995.

[84] H. Kraus *et al.* Quasiparticle trapping in a superconductive detector system exhibiting high energy and position resolution. *Physics Letters B*, 231:195–202, 1989.

[85] P. Colling *et al.* A quasiparticle trapping efficiency study using qet detectors. Unpublished, 1998.

[86] K.D. Irwin *et al.* A self-biasing cryogenic particle detector utilizing electrothermal feedback and a squid readout. *IEEE Trans. Appl. Supercond. (USA), IEEE Transactions on Applied*, 5:2690–3, 1995.

[87] S.W. Nam. *Development of Phonon-Mediated Cryogenic Particle Detectors with Electron and Nuclear Recoil Discrimination.* PhD thesis, Stanford University, 1998.

[88] M.J. Penn. *Nuclear-Recoil/Electron-Recoil Discrimination in Cryogenic Silicon Detectors for use in Dark Matter Searches.* PhD thesis, Stanford University, 1995.

[89] B. Chugg *et al.* Design of kilogram mass scale tes for the cryogenic dark matter search. *J. Low Temp. Phys. (USA), Journal of Low Temperature Physics*, 93:429–32, 1993.

[90] P.L. Brink. *Non-Equilibrium Superconductivity induced by X-ray Photons.* PhD thesis, Magdalen College, Oxford, 1995.

[91] P. Colling *et al.* Low-energy x-ray detection in cryogenic detectors with tungsten thermometers. *Nuclear Instruments and Methods in Physics Research*, 354:408–16, 1995.

[92] J.W. Gibson *et al.* superconductivity of tungsten. *Phys. Rev. Lett.*, 12:688–90, 1964.

[93] O.F. Kammerer*et al.* superconductivity in tungsten films. *Physics Letters*, 17:224–5, 1965.

[94] W.L. Bond *et al.* superconductivity in films of β tungsten. *Phys. Rev. Lett.*, 15:260–1, 1965.

[95] R.T. Johnson *et al.* superconductivity of tungsten. *Phys. Rev. Lett.*, 16:101–4, 1966.

[96] S. Basavaiah *et al.* superconductivity in β-tungsten films. *Journal of Applied Physics*, 39:5548–5556, 1968.

[97] P.H. Schmidt *et al.* Variation of superconducting transition temperatures of transition metal thin films deposited with nobel gases. *Journal of Applied Physics*, 44:1833–36, 1973.

[98] A. Smith. Activity in beryllium from uranium. Personal communication.

[99] W.K. Stockwell. *A Cryogenic Search for WIMP Dark Matter.* PhD thesis, University of California at Berkeley, 1996.

[100] Y.S. Tovloukian. *Thermophysical Properties of Matter*, volume 2, page 53.

[101] G. Heusser. Low radioactivity background techniques. *Ann. Rev. Nucl. Part. Sci.*, 45:543–590, 1995.

[102] A.J. Da Silva. *Development of a Low Background Environment for the Cryogenic Dark Matter Search.* PhD thesis, University of British Columbia, 1996.

[103] D.S. Akerib *et al.* Production of solder and flux with low radioactivity. *Nuclear Instruments and Methods in Physics Research, Section A*, 400:181–3, 1997.

[104] P.D. Barnes. *The Cryogenic Dark Matter Search (CDMS).* PhD thesis, University of California at Berkeley, 1996.

[105] J.D. Taylor *et al.* Low radioactivity cryostat system for a 20 mk particle detector. *Proceedings of the 1995 Cryogenic Engineering Conference*, 2:1971–8, 1996.

[106] R.P. Welty and J.M. Martinis. A series array of dc squids. *IEEE Trans. Magn. (USA), IEEE Transactions on Magnetics*, 27:2924–6, 1991.

[107] G.A. Northrop and J.P. Wolfe. Ballistic phonon imaging in germanium. *Physical Review B (Condensed Matter)*, 22:6196–6212, 1980.

[108] B.A. Young *et al.* Observation of ballistic phonons in silicon crystals induced by alpha particles. *Physical Review Letters*, 64:2795–8, 1990.

[109] Frank Pobell. *Matter and Methods at Low Temperatures.* Springer, 1996.

[110] N. Perrin and H. Budd. Phonon generation by joule heating in metal films. *Physical Review Letters*, 28:1701–3, 1972.

[111] R.M. Clarke *et al.* Observation of an enhanced ballistic phonon fraction for surface events in a cryogenic silicon detector. Submitted to Phys. Rev. Lett.

[112] A.T. Lee *et al.* Measurements of the ballistic phonon component resulting from nuclear recoils in crystalline silicon. *Physical Review Letters*, 71:1395–8, 1993.

[113] A.T. Lee *et al.* Measurements of the ballistic-phonon component resulting from nuclear and electron recoils in crystalline silicon. *Physical Review B (Condensed Matter)*, 54:3244–56, 1996.

[114] T. Dumas *et al.* The use of sio_2 sublayers beneath titanium transition edge sensors for the purpose of phonon spectroscopy. *Nucl. Instrum. Methods Phys. Res. A, Accel. Spectrom. Detect. Assoc. Equip.*, 370:183–6, 1996.

[115] W.A. Phillips. Two-level states in glasses. *Reports on Progress in Physics*, 50:1657–708, 1987.

[116] J.E. Graebner *et al.* Phonon localization in glasses. *Physical Review B (Condensed Matter)*, 34:5696–701, 1986.

[117] R.C. Zeller and R.O. Pohl. Thermal conductivity and specific heat of noncrystalline solids. *Physical Review B (Solid State)*, 4:2029–41, 1971.

[118] W. Dietsche and H. Kinder. Spectroscopy of phonon scattering in glass. *Physical Review Letters*, 43:1413–17, 1979.

[119] J. Wolter and R.E. Horstman. Transmission of high-frequency phonons through thin glass films. *Solid State Communications*, 37:171–4, 1981.

[120] T.C. Zhu *et al.* Attenuation of longitudinal-acoustic phonons in amorphous sio_2 at frequencies up to 440 ghz. *Physical Review B (Condensed Matter)*, 44:4281–9, 1991.

[121] A.R. Long *et al.* The scattering of phonons in thin films of amorphous silica. *Journal of Physics C (Solid State Physics)*, 19:467–85, 1986.

[122] J. Mebert and W. Eisenmenger. Phonon spectroscopy measurements at amorphous films. *Zeitschrift fur Physik B (Condensed Matter)*, 95:231–41, 1994.

[123] S.R. Elliott. A unified model for the low-energy vibrational behaviour of amorphous solids. *Europhysics Letters*, 19:201–6, 1992.

[124] D. Natelson. *collective behavior of tunneling systems in amorphous solids*. PhD thesis, Stanford University, 1998.

[125] R.P. Welty and J.M. Martinis. Two-stage integrated squid amplifier with series array output. *IEEE Trans. Appl. Supercond. (USA), IEEE Transactions on Applied*, 3:2605–8, 1993.